Development of theranostics nanomaterials

By

Qiuhong Yang

Submitted to the graduate degree program in Pharmaceutical Chemistry and the Graduate Faculty of the University of Kansas in partial fulfillment of the requirements for the degree of Doctor of Philosophy.

_____

Chairperson Dr. Laird Forrest

_____

Dr. Jeff Krise

_____

Dr. Teruna J. Siahaan

_____

Dr. Thomas Tolbert

_____

Dr. Shenqiang Ren

Date Defended: October 6th, 2014

The Dissertation Committee for Qiuhong Yang

certifies that this is the approved version of the following dissertation:

Development of theranostics nanometerials

_____

Chairperson Dr. Laird Forrest

Date approved: October 6th, 2014

Abstract

Clinical outcomes of conventional anticancer therapies are often compromised due to off-target toxicity and adaptive drug resistance. Moreover, currently there are no imaging modalities that can be utilized for real-time monitoring of therapeutic responses in the human body. Therefore, there is a critical need to develop a novel generation of personalized medicine that combines functionalities of diagnosis and therapy, with an ultimate goal of early detection, accurate treatment and timely assessment of therapeutic efficacy. Over the last few decades, a variety of nano-medical materials or devices such as liposomes, micelles, quantum dots, magnetic nanoparticles and plasmonic nanobubbles have been developed to deliver therapeutic products or diagnostic agents to the sites of disease in a controlled manner with reduced or eliminated side effects to normal tissues. This dissertation focuses on the development of functional molecular imaging probe and nanoparticles-based therapeutic agent delivery systems for effective theranostics of lymphatically metastatic cancer, thus opening new avenues to combat cancer.

In chapter 2, a near-infrared (NIR) absorbing dye -based caspase-9 image probe was synthesized in 11 steps to directly detect apoptotic cells with high specificity. This cell-permeable molecular contrast agent has demonstrated the feasibility of monitoring cancer cell apoptosis induced by chemotherapeutics in mice bearing head and neck squamous cell carcinoma (HNSCC), via non-invasive

photoacoustic imaging (PAI) within 24 h after treatment, thus to predict treatment efficacy.

In chapter 3, a biocompatible core/shell FePt@Fe3O4 magnetic nanoparticles (MNPs) was developed as a robust probe for magnetic resonance imaging (MRI) and to mediate hyperthermia treatment against breast tumor. Enhanced anti-tumor effectiveness was demonstrated in a mouse model of 4T1.2 Neu breast tumor as a consequence of the high magnetic-thermal energy transfer capability of MNPs. In addition, increased MRI contrast in the tumor region potentiated the clinical application of MNPs for cancer diagnosis.

In chapter 4, Cabozantinib (XL-184), a poorly water-soluble pan-kinase inhibitor, was encapsulated into a DSPE-PEG2000 micellar formulation with excellent colloidal stability. Compared with the free XL-184 solution, drug-loaded micelles exhibited increased intracellular drug uptake and higher cytotoxicity in one human lung adenocarcinoma epithelial cell line and two human malignant glioblastoma cell lines.

In chapter 5, a high molecular-weight hyaluronic acid-deferoxamine (DFO) conjugated was synthesized for sustained release delivery of DFO, whose potent iron-chelating capability can be utilized to reverse the radiotherapy-induced pathologic effects. The HA-DFO conjugate exhibited significantly decreased cytotoxicity to normal cells and excellent biodegradability. In addition, localized HA-DFO injection stimulated vascularity and improved bony regeneration and union after radiotherapy.

In chapter 6, a nano-hyaluronic acid (HA)-based anticancer drug, HA-Cisplatin, was subcutaneously injected in an in-vivo murine model for locally advanced melanoma. Compared with the untreated control group and cisplatin-treated group (intravenous or subcutaneous injection), significant tumor shrinkage was observed in the subcutaneous peri-tumoral HA-cisplatin group, offering great potential as a therapeutic option in the treatment of certain types of human melanoma.

Dedicated to:

My parents, Zhilin Liu and Shaolin Yang, and my husband, Biao Li,

for

their love, support and encouragement.

Acknowledgements

I would like to express my gratitude to my advisor, Dr. Laird Forrest, for his continuous guidance, encouragement and support throughout my graduate studies. Dr. Forrest introduced me to the targeted nanopharmceutics and controlled drug delivery technology, and I was immediately attracted to these beautiful disciplines. I appreciate the freedom that he provided me to pursue various projects and the insightful discussions and constructive criticisms at different stages of my research.

I am truly thankful to my oral prelim and dissertation committee members, Dr. Jeff Krise, Dr. Sue M. Lunte, Dr. Teruna Siahaan, Dr. Thomas Tolbert, Dr. Shenqiang Ren and Dr. Xinmai Yang for reading this dissertation and providing their valuable suggestions that improved the presentation and contents.

I am also grateful to the following former or current Forrest lab members with whom I had the fortunate to work with: Adel Alhowyan, Dr. Taryn Bagby, Dr. Shuang Cai, Dr. Shaofeng Duan, Jay Jha, Peter Kleindl, Dr. Yepeng Luan, Abby Perulis, Ryan Moulder, Dr. Yumei Xie, Ti Zhang, Dr. Yunqi Zhao. To my dear staff members of Pharm Chem, I thank you for the kindness and assistance over the past five years.

Last, but not the least, I would like to express my eternal gratitude to my parents and my husband. None of this would have been made possible without your everlasting love and support.

Table of Contents

Chapter 1

Introduction

1. Cancer theranostics:

Cancer is the second leading caused of death in the USA. The number of death in 2013 alone has reached over half a million, and American Cancer Society has estimated that there will be 585,720 cancer deaths and over 1.6 million newly diagnosed patients in the USA this year [1]. For this reason, the successful development of cancer therapeutic strategies requires effective anticancer agents with minimal related side effects and informative diagnostic imaging methods with improved specificity and sensitivity [2]. Cancer theranostics, as the name indicates, is an evolving multidisciplinary field that combines diagnostics and therapeutic approaches to the treatment of cancer [3]. The aim of cancer theranostics is to guide pharmacological treatment of cancer based on molecular diagnostic tests. This collaborative platform offers numerous advantages such as single-step procedures, targeted drug delivery and real-time monitoring of early treatment responses. It can be a therapeutic product administered following diagnosis to distinguish the disease subtype and select treatment regimens accordingly. It can also be a diagnosis following therapy to assess how the patients respond to the treatment and thus its ongoing efficacy. It is also possible that therapeutic and diagnostic products are used concurrently. For example, the combination of Genentech's Herceptin®, with DakoCytomation's HercepTest® is the best-known example of a commercialized theranostic. Herceptin® is an anti-HER-2/neu humanized monoclonal antibody, which effectively reduces growth of breast tumors with HER-2/neu overexpression. HercepTest ® is a semi-quantitative immunohistochemical test that employs the A0485 polyclonal antibody against HER-2/neu. Breast cancer patients with high

tumor scores in the HercepTest ® tend to respond well to Herceptin®, thus achieving increased efficacy of anticancer treatment and reducing adverse events associated with the therapy.

With recent advances in materials science and biomedical nanotechnology, a variety of models of duo-purpose nanomedicines have been reported as theranostic agents [4, 5] that implement therapeutics and diagnostic modalities into the same nanoparticle. A schematic illustration of a typical theranostic agent is shown in Figure 1. On one hand, the diagnostic functionality of theranostic nanoparticles includes locating the present disease, phenotyping the disease status and reporting the disease's response to the current treatment. The ways that theranostic nanoparticles achieve their therapeutic role, on the other hand, may entail several methods. First, anticancer agents (e.g. doxorubicin, docetaxel, paclitaxel, therapeutic siRNA) that are encapsulated into the nanoparticles are released from their carriers into the targeted disease sites. Second, therapeutic antibodies (e.g. Herceptin) attached to the surface of the nanoparticles can specifically bind with high affinity to the corresponding surface receptors of cancer cells, thereby disrupting cell regulation [6]. In another route, nanoparticles with intrinsic magnetic or thermoablative capabilities can respond to external stimuli and convert magnetic or light energy into heat energy to induce cancer cell death [7-11].

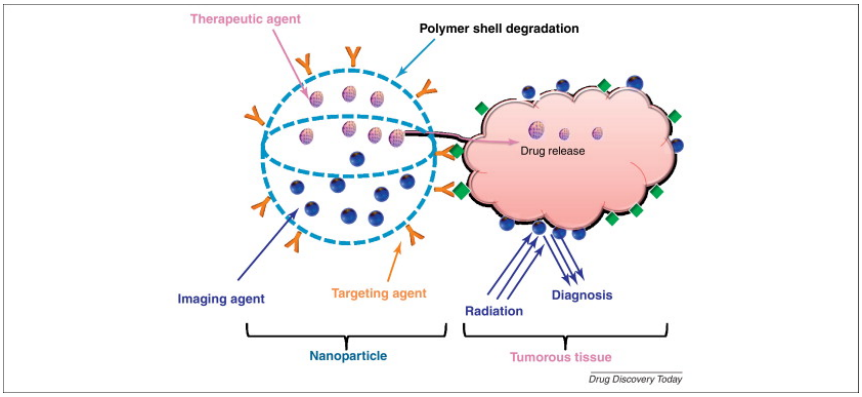

Figure 1. Schematic illustration of typical theranostic agents for cancer diagnosis and therapy. Figure originally published in reference [5]

The key advantages of cancer theranostic nanoparticles are excellent stability, large payloads, high surface area to volume ratio, and most importantly, their nanoscale size, which facilitates the nanoparticles to extravasate through the leaky vasculature and preferentially accumulate in the solid tumors (often termed the enhanced permeability and retention effect) to achieve tumor-selective imaging/therapy [12-14]. Cancer theranostic nanoparticles reported to date mainly include magnetic nanoparticles (MNPs), quantum dots (QDs), carbon nanotubes (CNTs), gold nanoparticles, silica etc, and they have opened new avenues for the development of effective cancer treatment. Listed in Table 1 [5, 15] are a variety of trials involving biomedical applications of theranostic agents.

Table 1. Examples of theranostic agents used for biomedical applications.

Contrast agent	Drug used	Applications
Manganese oxide	siRNA	MRI and RNA delivery [16]
Gold Nanoparticles	Doxorubicin	Diagnosis tumor targeting and photo thermal therapy [17-20]
Magnetic Nanoparticles	siRNA, doxorubicin and docetaxel	Targeting, MRI and therapy [21-25]
Silica	Pyropheophorbide and doxorubicin	Drug carrier, X-ray/CT imaging and Photodynamic therapy [19, 26, 27]
Carbon nanotubes	DNA plasmid, doxorubicin, paclitaxel	Diagnosis, DNA and drug delivery [28-31]
Quantum dots	Doxorubicin and methotrexate	Imaging, therapy and sensing [32-34]
Gadolinium-diethylenetriaminepentaacetic acid	Doxorubicin	MRI and therapy [35, 36]
Isotopes of rhenium -^{186}Re	Doxorubicin	Radionuclide imaging and chemoradionuclide therapy [37]

2. Molecular imaging in cancer theranostics

Within the field of diagnostic imaging, molecular imaging technology is rapidly emerging as a potent tool to actively target biomolecules and molecularly based events critical to a tumor biology. Molecular imaging possesses the potential for *in vivo* cancer detection, staging, treatment selection and real-time assessment of treatment response. Conventional anatomic imaging techniques such as mammography, computed tomography (CT) and magnetic resonance imaging (MRI) have been widely used in clinical medicine and radiology as standards of care. Anatomic imaging modalities rely on tumor size, shape or density for diagnosis and to evaluate therapeutic response by measuring changes in these parameters over time, which often occur with a delay due to molecular changes and lack of specificity. In comparison, functional molecular imaging technologies measure tumor-related abnormalities and anatomic locations of specific molecules of interest, such as cellular proliferation, growth factor expression, hypoxia-induced gene expression, occurrence of cell apoptosis or autophagy in vivo and monitor their changes over the course of treatments [38, 39]. Modalities that have been used for molecular imaging include MRI, magnetic resonance spectroscopy (MRS), positron emission tomography (PET), single photon emission CT (SPECT), ultrasound and photoacoustic imaging. These modalities offer a versatile platform to generate images with details of physiology, biological processes and molecular characteristics of tumors [40-43].

Molecular imaging can be performed using both endogenous and exogenous probes. Proton (^{1}H) MRS imaging, for example, utilizes endogenous protons to distinguish malignant tissues from benign tissues. *In vivo* levels of taurine, choline, creatine and lactate can be acquired on ^{1}H MRS spectra, where tumor tissues often show higher counts of choline and lactate [44, 45]. To enhance the signal and contrast of the imaging, however, most clinical molecular imaging applications employ exogenous imaging agents that comprise two components: one targeting moiety (e.g. small molecules, peptide or antibody) for localization and an imaging modality (e.g. fluorochrome, radionuclide or paramagnetic chelate) to enable visualization. Broadly, molecular imaging contrast agents can be categorized into four groups: (1) phenotypic probes to monitor characteristic changes of tumor physiology, exemplified by a radiotracer, ^{18}F-fluoro-2-deoxy-D-glucose [FDG], for PET/CT cross-sectional imaging [46-49]; (2) targeted probes to detect specific biomolecules of tumors, such as a receptor-targeting fluorescent peptide for optical tumor imaging [50], or ^{99}mTc-RP-527, a bombesin-based tripeptide to target bombesin/gastrin-releasing peptide receptor overexpressing breast carcinomas [51]; (3) cell-tracking probes to track cell motions critical to tumor survival, such as fluorophore labeled peptides [52] and MNPs-based CD 8+ T lymphocytes [53]; and (4) reporter gene to show whether a therapeutic gene remains intact after reaching its target [54].

3. Therapeutics delivery to lymphatically metastatic cancers

The lymphatic system is a sub-system of the circulatory system central to maintaining tissue homeostasis and immunofunction [55], including removing excess extravascular fluid; presenting to the immune system foreign bodies and pathogens; maturation of lymphocytes, and absorption of lipid-soluble nutrients from the digestive tract. The lymphatic system consists of an extensive network (Figure 2) of lymphatic vessels, lymph nodes, lymph, lymphatic organs (e.g. spleen and thymus), and lymphoid tissues (e.g. tonsils and Peyer's patches).

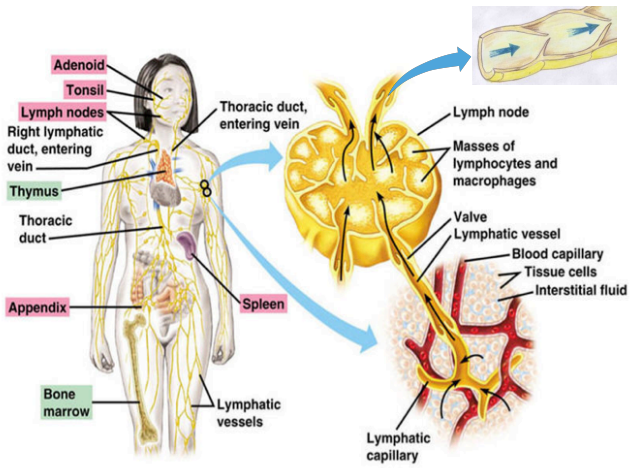

Figure 2. The human lymphatic system. Reproduced from [56].

The lymphatic system has distinctive physiological functions in lipid absorption and micro-particulate uptake, which could be harnessed as an alternative route for the delivery of pharmaceuticals to enhance their bioavailability and efficacy. Drug agents that would benefit from lymphatic concentration, such as vaccines and anti-cancer chemotherapeutics, could be engineered for preferential uptake into the lymphatic system to improve efficacy with reduced systemic distribution. In addition, with the increase in resolution and specificity of imaging technologies, there is the potential to monitor tumor cells that migrate through the lymphatic system and accumulate in the lymph nodes, which could detect very early micrometastatic disease. Two approaches are generally proposed to modify drug molecules for targeted accumulation in the lymphatic system. One approach is to chemically tailor the structures of the drug molecules and synthesize an inactive precursor of the drug, "prodrug", with enhanced lipophilicity, primarily used to improve gastric lymphatic absorption [57, 58]. Another approach is to develop particulate drug carriers to encapsulate drug molecules. With recent advances in materials science and technology, a variety of models of drug delivery to the lymphatic system have been reported in the literature including drug-polymer conjugates [59-65], drug-loaded emulsions [66-74], liposomes [75-99], solid lipid nanoparticles [100-106], nanostructured lipid carriers [107-113], polymeric micelles [114-117], polymeric nanoparticles [118-124] and microparticles [125-130], carbon nanotubes [131, 132], and nanocapsules.

Multiple factors including the physiological state of the interstitial space, immunological state, the lymph flow rate, the administration routes, the distance

between the injection site and the lymph nodes and the physicochemical parameters of the drug carrier/particles may alter the effectiveness of lymphatic drainage and transport of a drug carrier/particle. However, numerous studies have established that the physicochemical characteristics of a drug carrier play a predominant role in determining its efficiency. These predominant characteristics lie in three key aspects: particle size, surface charge and hydrophobicity [69, 82, 120, 133-135].

To achieve targeted drug lymphatic delivery, a desired carrier should possess the following features:

- Low- or non-toxicity to healthy tissues and organs;
- High colloidal, chemical and biological stability;
- Rapid drainage into the lymphatic capillaries from the injection site;
- High lymph nodal retention;
- Efficient delivery and release of therapeutic agents to the tissues or organs of interest.

In the process of creating an optimal drug carriers, nano-sized particles, especially being lipid and polymer-based, have distinct advantages over alternative models. These advantages, such as tunable size control and facile surface modifications with targeting molecules, have attracted intense interest. Summarized

in Table 2 is the development of nanocarriers for lymphatic system delivery with a special focus on liposomes and polymer-based nanoparticles.

Table 2. Examples of anticancer drug-loaded nanoparticles that have have demonstrated enhanced chemotherapeutic efficacies in tumor models.

Formulations	Encapsulated Drugs	Tumor Models	References
Liposomes	Paclitaxel	Ovarian, melanoma	[75, 136]
	Doxorubicin	Breast, lung, melanoma, gastric, ovarian, KB oral carcinoma, and Kaposi's sarcoma	[76-78, 81, 84, 137-141]
	Muramyl-tripeptide phosphoethanolamine	Ovarian	[85]
	DNA	Ovarian	[86]
	Melphalan	Mammary adenocarcinoma	[142]
	Cisplatin	Colon, lung	[87, 143]
	Combination of Vitamin E analogue and 9-nitro camptothecin	Lung metastasis	[144]
	Combination of Vitamin E analogue and paclitaxel	Lung metastasis	[145]
Polymeric Micelles	Cisplatin	Tongue	[114]
	Vinorelbine	Breast	[115]
	(1,2 diaminocyclohexane) platinum (II)	Gastrics	[116]
Poly (lactic-co-glycolic) Nanoparticles	Paclitaxel	Ovarian	[122]
	Cisplatin, doxorubicin	Head and neck, breast, melanoma	[60, 64, 65]
Chitosan Nanoparticles	Camptothecin	Liver, soft tissues	[119]

3.1 Liposomes

A liposome is a spherical self-enclosed vesicle with a lipid bilayer composed of amphiphilic monomers (e.g. phospholipids). The average diameter of small unilamellar liposomes ranges from 25 to 100 nm [146]. As shown in Figure 3, liposomes possess a structure with the long hydrocarbon chains of phospholipids lining up against one another to form a membrane and the charged hydrophilic groups on both sides orienting towards aqueous medium. Such a unique structure makes the liposomes especially suitable to encapsulate water-soluble molecules in the hydrophilic core and to trap lipophilic molecules within the bilayer. The structures of liposomes impart high colloidal stability, rendering the nanoparticles less sensitive to exterior environment change than micellular structures or emulsions. Additionally, polymer coatings on the surface can further sterically stabilize liposomes for prolonged blood retention.

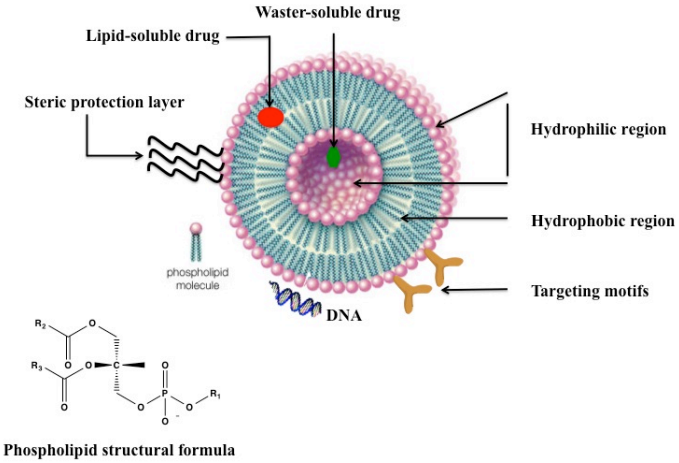

Figure 3. Typical structure of liposomes. Adapted from Encyclopedia Britannica [147].

Drug-encapsulated liposomes are typically prepared by a four-step film-rehydration method, which consists of (1) dissolving the drug and phospholipids (e.g. phosphatidylcholine or phosphatidylethanolamine) or cholesterol in a organic solvent such as chloroform or methanol, (2) removal of the solvent by rotary evaporation under reduced pressure to form a uniform and thin film, (3) hydration of the film in an aqueous medium, and (4) size-reduction via sonication or extrusion.

Liposomes are generally considered as a promising drug carrier for lymphatic delivery, due to their biocompatibility, tunable size, and dual loading capacity for both hydrophilic and hydrophobic drugs. A variety of liposomal formulations of anticancer drugs have been approved by drug administration agencies or are currently in the advanced stages of clinical trials. For example, Doxil®, the first FDA-approved nano-drug, is a doxorubicin-encapsulated liposomal formulation coated with PEG. Doxil® has been used as a first-line anticancer drug administered via IV infusion to treat a series of cancers including Kaposi's sarcoma, breast cancer, gastric cancer, ovarian cancer, and head and neck squamous cell carcinoma [37, 81, 137-140].

Unmodified and polymer-coated liposomes drain into the lymphatic capillaries and then are internalized by macrophages in the regional lymph nodes and tumor cells. Most tumor cells, tumor lymphatic and tumor-associated macrophages express specific membrane associated proteins such as receptors, membrane transporters, and adhesion molecules. Therefore, conjugation of targeting motifs to the surface of liposomes could specifically target the

encapsulated drugs to the tumor lymphatics via receptor-mediated interactions and consequently enhance the therapeutics efficacy.

LyP-1, for example, is a cyclic nanopeptide (CGNKRTRGC) that possesses specific binding ability with the p32/gC1q receptor overexpressed in tumor cells, lymphatics vessels and tumor-associated macrophages [148-150]. Yan et al [76, 77] synthesized LyP-1-conjugated PEG-DSPE and prepared a lymphatic-targeting liposomal formulation of doxorubicin, which has demonstrated superior chemotherapeutic efficacy in animal models implanted with lymphatic metastatic breast and lung tumors, in part by suppressing lymph node metastases and disrupting tumor lymphatics. Surface modification with antigen presenting cell-specific antibodies is another approach to enhancing the lymphatic delivery of liposomes. Coupling a non-specific IgG to PEG-bearing liposomes has been found to increase its retention in both the primary and secondary lymph nodes [79]. A closer examination of the immuno-PEG-liposomes structure revealed that IgG chains orient randomly on the liposomes surface and expose its Fc region to facilitate the recognition by Fc receptors on the surface of macrophages. Immunoliposome-mediated lymphatic targeting to specific tumor cells, on the other hand, could be enhanced by attaching Fab' fragments of monoclonal antibodies that are directed against specific a antigen present on the cancer cells [83, 84]. Bestman-Smith et. al [83] reported an elevated accumulation of the anti-HLA-DR-coupled PEG-liposomes in lymph nodes over plain liposomes or PEG-liposomes.

In addition to ligand-attached liposomes, cationic liposomes prepared from DOTAP and DOPC have been shown to preferentially target tumor endothelial cells and vessels [82, 86, 136, 151]. However, the mechanism underlying their selective targeting has not yet been fully elucidated.

3.2 Polymer-based carriers

Numerous therapeutic agents have been conjugated or encapsulated into polymer-based nanoparticles for targeted and sustained lymphatic delivery to inhibit tumor growth and metastases. The widely utilized polymers are categorized into natural polymers such as dextran [61, 62], hyaluronic acid (HA) [60, 63, 152], and synthetic polymers including poly (ethylene glycol)-block-poly (3-caprolactone) (PEG-PCL) [117], poly (L-lactic acid) [125], poly (lactide-co-glycolide) (PLGA) [120, 121, 153], poly (hexylcyanoacrylate) nanoparticles (PHCA) and poly (methylmethacrylate) (PMMA) [154].

3.2.1 Natural polymers

Polysaccharide-based nanoparticles, such as dextran and HA (Figure 4), have gained popularity in developing controlled-release drug delivery systems, attributed to their biocompatibility, biodegradability, broad range of physicochemical properties and their versatile modification by simple chemical conjugations with drug molecules.

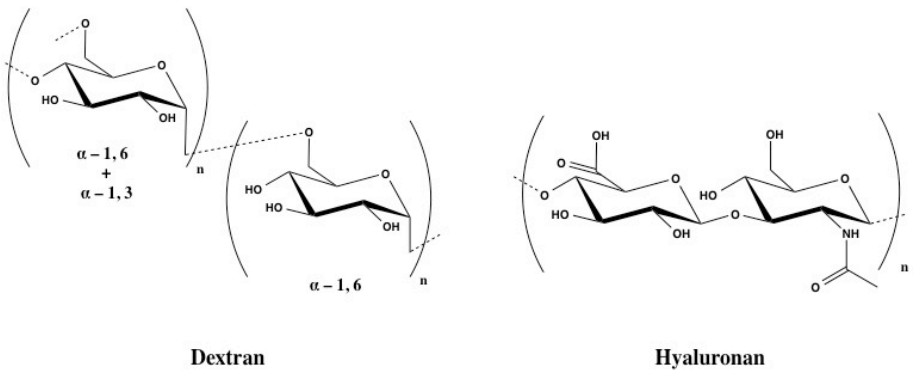

Figure 4. Structures of Dextran and Hyaluronan

The feasibility of mitomycin C-dextran conjugate (MMC-D) as a lymphatic drug delivery system has been earlier demonstrated by Takakura et al [61]. Anticancer antibiotic, mitomycin C, was first conjugated to dextran with molecular weights of 10 to 500 kDa via ε-aminocaproic acid as a spacer, and then administered by IM injection to rats inoculated with leukemia cells. In contrast to the free drug and MMC-D prepared with the lowest molecular weight (10 kDa), larger MMC-Ds afforded significantly higher drug concentrations in the thoracic lymph as well as substantially enhanced accumulation in the regional lymph nodes, resulting in a more efficient suppression of tumor growth and metastasis.

Hyaluronic acid (HA) is another type of natural polysaccharide that consists of alternating D-glucuronic acid and N-acetyl D-glucosamine. HA is present throughout the body with particularly high concentrations in the connective tissues. In the process of clearance by the lymphatic system, HA is catabolized in the lymph nodes by receptor-mediated endocytosis and lysosomal degradation. Some invasive tumors such as breast and head and neck tumors, preferentially uptake HA over normal tissues due to their surface overexpression of the HA receptor CD44. Therefore, conjugation of chemotherapeutic agents to HA could provide an efficacious approach to treating lymphatic metastases. Cai et al synthesized two HA-cytotoxic drug nanoconjugates, HA-cisplatin [65, 152, 155, 156] and HA-doxorubicin [60], which have both exhibited *in vivo* sustained-release profiles and enhanced drug retention by lymph nodes in locally aggressive metastatic tumor models of head and neck squamous cell cariconma and breast cancer. Consequently, intralymphatic delivery of HA-cisplatin and HA-doxorubicin significantly inhibited

tumor progression and led to the increased survival rates when compared with the conventional chemotherapy.

3.2.2 Synthetic polymeric nanoparticles

In aqueous solution, biodegradable amphiphilic block copolymers such as PEG-PCL or PEG-poly (aminio acid) self-assemble into a core-shell structured polymeric micelle with a size of 20 to 100 nm, as shown in Figure 5. The description and characterization of polymeric micelles and the recent developments in functional biodegradable micelles for safe and efficient cancer chemotherapy have been extensively reviewed by Croy et at [157] and Deng et al [158]. In the past decade, polymeric micelles have generated great interest for sustained delivery of poorly water-soluble anticancer drugs attributed to their inherent physiochemical features. For example, a core formed from poly (3-caprolactone) or poly (amino acid) provides a hydrophobic environment for accommodating lipophilic drug molecules, while the presence of PEG in the hydrophilic shell spares micelles from aggregation and also reduces the fast clearance of the micelles by RES.

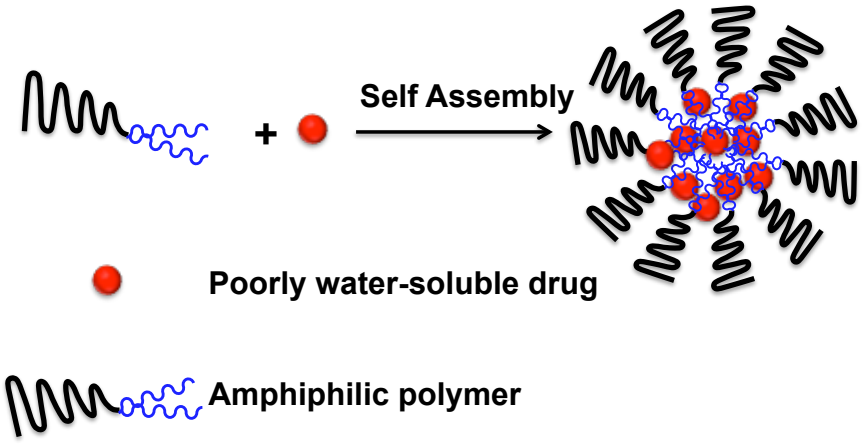

Figure 5. Self-assembly of polymeric micelles encapsulated with poorly water-soluble anticancer drugs.

Drug-loaded polymeric micelles generally enter the primary tumor via passive diffusion through blood capillaries after IV administration. Surface-modification of the polymeric micelles with targeting ligands can enhance their binding with tumor lymphatic vessels through a receptor-mediated interaction to achieve active lymphatic targeting. LyP-1 peptide, as mentioned in section 1.3.1, has been identified as a ligand for p32/gC1qR, which is overexpressed in highly metastatic tumor cells and tumor lymphatics [148]. Wang et al [117] developed a LyP-1 peptide-conjugated PEG-PCL micelles (LyP-1-PM) with a size of around 30 nm. The specific binding of the LyP-1-PM with highly metastatic tumor cells (MDA-MB-435S) and lymphatic endothelial cells was first observed by flow cytometry and laser confocal microscopy, leading to an *in vivo* investigation of its lymphatic targeting in a breast tumor model. After IV injection of the fluorescein-loaded LyP-1-PM into the breast tumor-bearing mice, *in vivo* fluorescent imaging only showed good co-localization of the LyP-1-1PM with the lymph vessel marker (LYVE-1) but not with the blood vessel marker (CD31). In addition, targeted delivery of artemisinin-encapsulated LyP-1-PM remarkably enhanced the antitumor efficacy and reduced the systemic toxicity, indicating the potential of LyP-1-targeting polymeric micelles as specific drug carriers for lymphatic delivery.

Poly (lactide-co-glycolide) (PLGA) -based drug carriers have also been used for lymphatic targeting. This biocompatible and biodegradable polymer has been approved by the FDA for use in humans as a therapeutic device and it has been extensively studied as a sustained release system to deliver chemotherapeutic agents [120, 121, 126, 153]. Drug-incorporated PLGA microspheres or sub-100 nm

nanoparticles can be readily prepared by emulsification-solvent evaporation methods [159-163], and it has been reported that surface-coating with poloxamer or poloxamine block co-polymers can remarkably enhance the maximal lymphatic uptake from 6% to 17% after SC injection [124]. Paclitaxel-loaded PLGA (PTX-PLGA) microspheres have been demonstrated to effectively inhibit tumor growth in animal models bearing intraperitoneal carcinomatosis [125] and subcutaneous carcinoma [127]. Liu et al [128] further incorporated PTX-PLGA into a biodegradable gelatin sponge that enabled a continuous release of PTX into the lymphatics with subsequent accumulation in the regional lymph nodes. The PTX-PLGA sponge was implanted into the pleural space of rats, and its retention in mediastinal lymph nodes was compared with that of the IV PTX solution. During the given 28-d experimental time, an over 400-fold increase in PTX exposure at the ipsilateral mediastinal lymph nodes and approximately a 100-fold increase at the contralateral side were observed in the group treated with IP PTX-PLGA sponge. Attributed to the improved drug distribution into the lymphatic system, the PTX-PLGA sponge also exhibited the enhanced antitumor efficacy in an orthotopic lung tumor-bearing rat model, which resulted in an 80% inhibition of lymphatic metastasis.

4 Conclusions

The theranostic agent integrates the advantages of non-invasive in *vivo* diagnosis, evaluation of therapeutic response and administration of chemotherapeutic agents within a single nanoparticles for biomedical applications.

The unique physiochemical properties possessed by magnetic nanoparticles, quantum dots, carbon nanotubes and gold nanoparticles enable them to serve as efficient contrast agents for a variety of imaging modalities for cancer diagnosis, including MRI, CT and photoacoustics imaging. In addition, magnetic nanoparticles can also mediate local hyperthermia in response to an external alternating magnetic field to disrupt tumor tissues, while quantum dots photosensitize upon activation by light and then transfer energy to surrounding oxygen molecules to damage cancer cells. As sufficient accumulation of the theranostic agents in diseased regions is required, formulations such as liposomes or polymer-based nanocarriers have been under extensive investigation as platforms to selectively deliver cargos to tumors with reduced systemic toxicity. In summary, nanoparticle-based cancer theranostic agents are expected to play a significant role in the development of personalized medicine.

5. References

1. Siegel, R., et al., *Cancer statistics, 2014.* CA-Cancer J Clin, 2014. **64**(1): p. 9-29.
2. Solanki, A., J.D. Kim, and K.B. Lee, *Nanotechnology for regenerative medicine: nanomaterials for stem cell imaging.* Nanomedicine (Lond), 2008. **3**(4): p. 567-78.
3. Warner, S., *Diagnostics + therapy = theranostics.* Scientist, 2004. **18**(16): p. 38-39.

4. Xie, J., S. Lee, and X. Chen, *Nanoparticle-based theranostic agents.* Adv Drug Deliv Rev, 2010. **62**(11): p. 1064-1079.

5. Ahmed, N., H. Fessi, and A. Elaissari, *Theranostic applications of nanoparticles in cancer.* Drug Discov Today, 2012. **17**(17–18): p. 928-934.

6. Lee, J.H., et al., *Artificially engineered magnetic nanoparticles for ultra-sensitive molecular imaging.* Nat Med, 2007. **13**(1): p. 95-9.

7. Tsiapa, I., et al., *Tc-labeled aminosilane-coated iron oxide nanoparticles for molecular imaging of alphabeta-mediated tumor expression and feasibility for hyperthermia treatment.* J Colloid Interface Sci, 2014. **433C**: p. 163-175.

8. Yuan, C., et al., *Magnetic nanoparticles for targeted therapeutic gene delivery and magnetic-inducing heating on hepatoma.* Nanotechnology, 2014. **25**(34): p. 345101.

9. Majeed, J., et al., *Enhanced specific absorption rate in silanol functionalized FeO core-shell nanoparticles: Study of Fe leaching in FeO and hyperthermia in L929 and HeLa cells.* Colloids Surf B Biointerfaces, 2014. **122C**: p. 396-403.

10. Baldi, G., et al., *In vivo anticancer evaluation of the hyperthermic efficacy of anti-human epidermal growth factor receptor-targeted PEG-based nanocarrier containing magnetic nanoparticles.* Int J Nanomedicine, 2014. **9**: p. 3037-56.

11. Burford, C.D., et al., *Nanoparticle Mediated Thermal Ablation of Breast Cancer Cells Using a Nanosecond Pulsed Electric Field.* IEEE Trans Nanobioscience, 2013. **12**(2): p. 112-118.

12. Maeda, H., H. Nakamura, and J. Fang, *The EPR effect for macromolecular drug delivery to solid tumors: Improvement of tumor uptake, lowering of systemic*

toxicity, and distinct tumor imaging in vivo. Adv Drug Deliv Rev, 2013. **65**(1): p. 71-9.

13. Jain, P.K., et al., *Noble metals on the nanoscale: optical and photothermal properties and some applications in imaging, sensing, biology, and medicine.* Acc Chem Res, 2008. **41**(12): p. 1578-86.
14. Wagner, V., et al., *The emerging nanomedicine landscape.* Nat Biotechnol, 2006. **24**(10): p. 1211-7.
15. Luk, B.T., R.H. Fang, and L. Zhang, *Lipid- and polymer-based nanostructures for cancer theranostics.* Theranostics, 2012. **2**(12): p. 1117-26.
16. Bae, K.H., et al., *Surface functionalized hollow manganese oxide nanoparticles for cancer targeted siRNA delivery and magnetic resonance imaging.* Biomaterials, 2011. **32**(1): p. 176-84.
17. Huang, P., et al., *Folic acid-conjugated silica-modified gold nanorods for X-ray/CT imaging-guided dual-mode radiation and photo-thermal therapy.* Biomaterials, 2011. **32**(36): p. 9796-809.
18. Chen, W., et al., *A molecularly targeted theranostic probe for ovarian cancer.* Mol Cancer Ther, 2010. **9**(4): p. 1028-38.
19. Prabaharan, M., et al., *Gold nanoparticles with a monolayer of doxorubicin-conjugated amphiphilic block copolymer for tumor-targeted drug delivery.* Biomaterials, 2009. **30**(30): p. 6065-75.
20. Lu, W., et al., *Targeted photothermal ablation of murine melanomas with melanocyte-stimulating hormone analog-conjugated hollow gold nanospheres.* Clin Cancer Res, 2009. **15**(3): p. 876-86.

21. Yang, X., et al., *Multifunctional SPIO/DOX-loaded wormlike polymer vesicles for cancer therapy and MR imaging.* Biomaterials, 2010. **31**(34): p. 9065-73.

22. Ling, Y., et al., *Dual docetaxel/superparamagnetic iron oxide loaded nanoparticles for both targeting magnetic resonance imaging and cancer therapy.* Biomaterials, 2011. **32**(29): p. 7139-50.

23. Liu, Y., et al., *PEGylated FePt@Fe2O3 core-shell magnetic nanoparticles: potential theranostic applications and in vivo toxicity studies.* Nanomedicine, 2013. **9**(7): p. 1077-88.

24. Erten, A., et al., *Magnetic resonance and fluorescence imaging of doxorubicin-loaded nanoparticles using a novel in vivo model.* Nanomedicine, 2010. **6**(6): p. 797-807.

25. Lai, J.-R., et al., *Multifunctional doxorubicin/superparamagnetic iron oxide-encapsulated Pluronic F127 micelles used for chemotherapy/magnetic resonance imaging.* J Appl Phys, 2010. **107**(9): p. -.

26. Roy, I., et al., *Ceramic-based nanoparticles entrapping water-insoluble photosensitizing anticancer drugs: a novel drug-carrier system for photodynamic therapy.* J Am Chem Soc, 2003. **125**(26): p. 7860-5.

27. Park, J.H., et al., *Biodegradable luminescent porous silicon nanoparticles for in vivo applications.* Nat Mater, 2009. **8**(4): p. 331-6.

28. Pantarotto, D., et al., *Functionalized carbon nanotubes for plasmid DNA gene delivery.* Angew Chem Int Ed Engl, 2004. **43**(39): p. 5242-6.

29. Liu, Z., et al., *Drug delivery with carbon nanotubes for in vivo cancer treatment.* Cancer Res, 2008. **68**(16): p. 6652-60.

30. Liu, Z., et al., *Carbon Nanotubes in Biology and Medicine: In vitro and in vivo Detection, Imaging and Drug Delivery.* Nano Res, 2009. **2**(2): p. 85-120.

31. Liu, Z., et al., *Supramolecular stacking of doxorubicin on carbon nanotubes for in vivo cancer therapy.* Angew Chem Int Ed Engl, 2009. **48**(41): p. 7668-72.

32. Kumar, R., et al., *In vitro evaluation of theranostic polymeric micelles for imaging and drug delivery in cancer.* Theranostics, 2012. **2**(7): p. 714-22.

33. Savla, R., et al., *Tumor targeted quantum dot-mucin 1 aptamer-doxorubicin conjugate for imaging and treatment of cancer.* J Control Release, 2011. **153**(1): p. 16-22.

34. Yuan, J., et al., *Anticancer drug-DNA interactions measured using a photoinduced electron-transfer mechanism based on luminescent quantum dots.* Anal Chem, 2009. **81**(1): p. 362-8.

35. Liu, T., et al., *Multifunctional pH-disintegrable micellar nanoparticles of asymmetrically functionalized beta-cyclodextrin-based star copolymer covalently conjugated with doxorubicin and DOTA-Gd moieties.* Biomaterials, 2012. **33**(8): p. 2521-31.

36. Tagami, T., et al., *MRI monitoring of intratumoral drug delivery and prediction of the therapeutic effect with a multifunctional thermosensitive liposome.* Biomaterials, 2011. **32**(27): p. 6570-8.

37. Soundararajan, A., et al., *[(186)Re]Liposomal doxorubicin (Doxil): in vitro stability, pharmacokinetics, imaging and biodistribution in a head and neck squamous cell carcinoma xenograft model.* Nucl Med Biol, 2009. **36**(5): p. 515-24.

38. Miller, J.C. and J.H. Thrall, *Clinical molecular imaging.* J Am Coll Radiol, 2004. **1**(1, Supplement): p. 4-23.

39. Massoud, T.F. and S.S. Gambhir, *Molecular imaging in living subjects: seeing fundamental biological processes in a new light.* Genes Dev, 2003. **17**(5): p. 545-80.

40. Bradbury, M. and H. Hricak, *Molecular MR imaging in oncology.* Magn Reson Imaging Clin N Am, 2005. **13**(2): p. 225-40.

41. Grassi, R., R. Lagalla, and A. Rotondo, *Genomics, proteomics, MEMS and SAIF: which role for diagnostic imaging?* Radiol Med, 2008. **113**(6): p. 775-8.

42. Kircher, M.F., L. Josephson, and R. Weissleder, *Ratio imaging of enzyme activity using dual wavelength optical reporters.* Mol Imaging, 2002. **1**(2): p. 89-95.

43. Weissleder, R. and M.J. Pittet, *Imaging in the era of molecular oncology.* Nature, 2008. **452**(7187): p. 580-9.

44. Howe, F.A., et al., *Proton spectroscopy in vivo.* Magn Reson Q, 1993. **9**(1): p. 31-59.

45. Negendank, W., *Studies of human tumors by MRS: a review.* NMR Biomed, 1992. **5**(5): p. 303-24.

46. Buck, A.K., et al., *Economic evaluation of PET and PET/CT in oncology: evidence and methodologic approaches.* J Nucl Med Technol, 2010. **38**(1): p. 6-17.

47. Gupta, N., et al., *Dynamic positron emission tomography with F-18 fluorodeoxyglucose imaging in differentiation of benign from malignant lung/mediastinal lesions.* Chest, 1998. **114**(4): p. 1105-11.

48. Czernin, J., M.R. Benz, and M.S. Allen-Auerbach, *PET/CT imaging: The incremental value of assessing the glucose metabolic phenotype and the structure of cancers in a single examination.* Eur J Radiol, 2010. **73**(3): p. 470-80.

49. Kelloff, G.J., et al., *Progress and promise of FDG-PET imaging for cancer patient management and oncologic drug development.* Clin Cancer Res, 2005. **11**(8): p. 2785-808.

50. Becker, A., et al., *Receptor-targeted optical imaging of tumors with near-infrared fluorescent ligands.* Nat Biotechnol, 2001. **19**(4): p. 327-31.

51. Van de Wiele, C., et al., *Gastrin-releasing peptide receptor imaging in human breast carcinoma versus immunohistochemistry.* J Nucl Med, 2008. **49**(2): p. 260-4.

52. Koch, A.M., et al., *Uptake and Metabolism of a Dual Fluorochrome Tat-nanoparticle in HeLa Cells.* Bioconjugate Chem, 2003. **14**(6): p. 1115-1121.

53. Schottelius, M. and H.J. Wester, *Molecular imaging targeting peptide receptors.* Methods, 2009. **48**(2): p. 161-77.

54. Allport, J.R. and R. Weissleder, *In vivo imaging of gene and cell therapies.* Exp Hematol, 2001. **29**(11): p. 1237-46.

55. Maby-El Hajjami, H. and T.V. Petrova, *Developmental and pathological lymphangiogenesis: from models to human disease.* Histochem Cell Biol, 2008. **130**(6): p. 1063-78.

56. *Lymphatic System: Anatomy and Histology*. [cited 2014 Feburary 6]; Available from: http://legacy.owensboro.kctcs.edu/gcaplan/anat2/notes/APIINotes7 Lymphatic Anatomy.htm.

57. Yanez, J.A., et al., *Intestinal lymphatic transport for drug delivery.* Adv Drug Deliv Rev, 2011. **63**(10-11): p. 923-42.

58. White, K.L., et al., *Lymphatic transport of Methylnortestosterone undecanoate (MU) and the bioavailability of methylnortestosterone are highly sensitive to the mass of coadministered lipid after oral administration of MU.* J Pharmacol Exp Ther, 2009. **331**(2): p. 700-9.

59. Kaminskas, L.M., et al., *PEGylation of interferon α2 improves lymphatic exposure after subcutaneous and intravenous administration and improves antitumour efficacy against lymphatic breast cancer metastases.* J Control Release, 2013. **168**(2): p. 200-8.

60. Cai, S., et al., *Localized doxorubicin chemotherapy with a biopolymeric nanocarrier improves survival and reduces toxicity in xenografts of human breast cancer.* J Control Release, 2010. **146**(2): p. 212-8.

61. Takakura, Y., et al., *Enhanced lymphatic delivery of mitomycin C conjugated with dextran.* Cancer Res, 1984. **44**(6): p. 2505-10.

62. Kim, J., et al., *Lymphatic Delivery of 99mTc-labeled Dextran Acetate Particles Including Cyclosporine A.* J Microbiol Biotechnol, 2008. **18**(9): p. 1599-605.

63. Jeong, Y.I., et al., *Cisplatin-incorporated hyaluronic acid nanoparticles based on ion-complex formation.* J Pharm Sci, 2008. **97**(3): p. 1268-76.

64. Yang, Q., et al., *In vivo efficacy of nano hyaluronan-conjugated cisplatin for treatment of murine melanoma.* J Drugs Dermatol, 2014. **13**(3): p. 283-7.

65. Cai, S., et al., *Carrier-based intralymphatic cisplatin chemotherapy for the treatment of metastatic squamous cell carcinoma of the head & neck.* Ther Deliv, 2010. **1**(2): p. 237-45.

66. Wu, H., et al., *Examination of lymphatic transport of puerarin in unconscious lymph duct-cannulated rats after administration in microemulsion drug delivery systems.* Eur J Pharm Sci, 2011. **42**(4): p. 348-53.

67. Singh, B., et al., *Optimized nanoemulsifying systems with enhanced bioavailability of carvedilol.* Colloids Surf B Biointerfaces, 2013. **101**(0): p. 465-74.

68. Sha, X., et al., *Self-microemulsifying drug-delivery system for improved oral bioavailability of probucol: preparation and evaluation.* Int J Nanomedicine, 2012. **7**: p. 705-12.

69. Khullar, O.V., et al., *Nanoparticle migration and delivery of Paclitaxel to regional lymph nodes in a large animal model.* J Am Coll Surg, 2012. **214**(3): p. 328-37.

70. Sun, M., et al., *Intestinal absorption and intestinal lymphatic transport of sirolimus from self-microemulsifying drug delivery systems assessed using the*

single-pass intestinal perfusion (SPIP) technique and a chylomicron flow blocking approach: linear correlation with oral bioavailabilities in rats. Eur J Pharm Sci, 2011. **43**(3): p. 132-40.

71. Thakkar, H., et al., *Formulation and characterization of lipid-based drug delivery system of raloxifene-microemulsion and self-microemulsifying drug delivery system.* J Pharm Bioallied Sci, 2011. **3**(3): p. 442-8.

72. Liu, R., et al., *Prevention of nodal metastases in breast cancer following the lymphatic migration of paclitaxel-loaded expansile nanoparticles.* Biomaterials, 2013. **34**(7): p. 1810-9.

73. Yoshimura, K., et al., *Evaluation of endoscopic pirarubicin-Lipiodol emulsion injection therapy for gastric cancer.* Gan To Kagaku Ryoho, 1996. **23**(11): p. 1519-22.

74. Atef, E. and A.A. Belmonte, *Formulation and in vitro and in vivo characterization of a phenytoin self-emulsifying drug delivery system (SEDDS).* Eur J Pharm Sci, 2008. **35**(4): p. 257-63.

75. Ye, L., et al., *Antitumor effect and toxicity of Lipusu in rat ovarian cancer xenografts.* Food Chem Toxicol, 2013. **52**: p. 200-6.

76. Yan, Z., et al., *LyP-1-conjugated PEGylated liposomes: a carrier system for targeted therapy of lymphatic metastatic tumor.* J Control Release, 2012. **157**(1): p. 118-25.

77. Yan, Z., et al., *LyP-1-conjugated doxorubicin-loaded liposomes suppress lymphatic metastasis by inhibiting lymph node metastases and destroying tumor lymphatics.* Nanotechnology, 2011. **22**(41): p. 415103.

78. Herringson, T.P. and J.G. Altin, *Effective tumor targeting and enhanced anti-tumor effect of liposomes engrafted with peptides specific for tumor lymphatics and vasculature.* Int J Pharm, 2011. **411**(1-2): p. 206-14.

79. Moghimi, M. and S.M. Moghimi, *Lymphatic targeting of immuno-PEG-liposomes: evaluation of antibody-coupling procedures on lymph node macrophage uptake.* J Drug Target, 2008. **16**(7): p. 586-90.

80. Jain, S., A.K. Tiwary, and N.K. Jain, *PEGylated elastic liposomal formulation for lymphatic targeting of zidovudine.* Curr Drug Deliv, 2008. **5**(4): p. 275-81.

81. Akamo, Y., et al., *Chemotherapy targeting regional lymph nodes by gastric submucosal injection of liposomal adriamycin in patients with gastric carcinoma.* Jpn J Cancer Res, 1994. **85**(6): p. 652-8.

82. Zhuang, Y., et al., *PEGylated cationic liposomes robustly augment vaccine-induced immune responses: Role of lymphatic trafficking and biodistribution.* J Control Release, 2012. **159**(1): p. 135-42.

83. Bestman-Smith, J., et al., *Sterically stabilized liposomes bearing anti-HLA-DR antibodies for targeting the primary cellular reservoirs of HIV-1.* Biochim Biophys Acta, 2000. **1468**(1-2): p. 161-74.

84. Vingerhoeds, M.H., et al., *Immunoliposome-mediated targeting of doxorubicin to human ovarian carcinoma in vitro and in vivo.* Br J Cancer, 1996. **74**(7): p. 1023-9.

85. Malik, S.T., et al., *Therapy of human ovarian cancer xenografts with intraperitoneal liposome encapsulated muramyl-tripeptide*

phosphoethanolamine (MTP-PE) and recombinant GM-CSF. Br J Cancer, 1991. **63**(3): p. 399-403.

86. Lee, M.J., et al., *Intraperitoneal gene delivery mediated by a novel cationic liposome in a peritoneal disseminated ovarian cancer model.* Gene Ther, 2002. **9**(13): p. 859-66.

87. Hirai, M., et al., *Novel and simple loading procedure of cisplatin into liposomes and targeting tumor endothelial cells.* Int J Pharm, 2010. **391**(1-2): p. 274-83.

88. Hirano, K. and C.A. Hunt, *Lymphatic transport of liposome-encapsulated agents: effects of liposome size following intraperitoneal administration.* J Pharm Sci, 1985. **74**(9): p. 915-21.

89. Oussoren, C. and G. Storm, *Lymphatic uptake and biodistribution of liposomes after subcutaneous injection: III. Influence of surface modification with poly(ethyleneglycol).* Pharm Res, 1997. **14**(10): p. 1479-84.

90. Kaur, C.D., M. Nahar, and N.K. Jain, *Lymphatic targeting of zidovudine using surface-engineered liposomes.* J Drug Target, 2008. **16**(10): p. 798-805.

91. Trubetskoy, V.S., et al., *Controlled delivery of Gd-containing liposomes to lymph nodes: surface modification may enhance MRI contrast properties.* Magn Reson Imaging, 1995. **13**(1): p. 31-7.

92. Torchilin, V.P., et al., *Targeted delivery of diagnostic agents by surface-modified liposomes.* J Control Release, 1994. **28**(1-3): p. 45-58.

93. Perrie, Y., et al., *Liposome (Lipodine)-mediated DNA vaccination by the oral route.* J Liposome Res, 2002. **12**(1-2): p. 185-97.

94. Ling, S.S., et al., *Enhanced oral bioavailability and intestinal lymphatic transport of a hydrophilic drug using liposomes.* Drug Dev Ind Pharm, 2006. **32**(3): p. 335-45.

95. Koshkina, N.V., et al., *Distribution of camptothecin after delivery as a liposome aerosol or following intramuscular injection in mice.* Cancer Chemother Pharmacol, 1999. **44**(3): p. 187-92.

96. Parker, R.J., K.D. Hartman, and S.M. Sieber, *Lymphatic absorption and tissue disposition of liposome-entrapped [14C]Adriamycin following intraperitoneal administration to rats.* Cancer Res, 1981. **41**(4): p. 1311-7.

97. Kim, C.K. and J.H. Han, *Lymphatic delivery and pharmacokinetics of methotrexate after intramuscular injection of differently charged liposome-entrapped methotrexate to rats.* J Microencapsul, 1995. **12**(4): p. 437-46.

98. Rutenfranz, I., A. Bauer, and H. Kirchner, *Pharmacokinetic study of liposome-encapsulated human interferon-gamma after intravenous and intramuscular injection in mice.* J Interferon Res, 1990. **10**(3): p. 337-41.

99. Zavaleta, C.L., et al., *Use of avidin/biotin-liposome system for enhanced peritoneal drug delivery in an ovarian cancer model.* Int J Pharm, 2007. **337**(1-2): p. 316-28.

100. Kuo, Y.C. and H.F. Ko, *Targeting delivery of saquinavir to the brain using 83-14 monoclonal antibody-grafted solid lipid nanoparticles.* Biomaterials, 2013. **34**(20): p. 4818-30.

101. Chalikwar, S.S., et al., *Formulation and evaluation of Nimodipine-loaded solid lipid nanoparticles delivered via lymphatic transport system.* Colloids Surf B Biointerfaces, 2012. **97**: p. 109-16.

102. Alex, A., et al., *Enhanced delivery of lopinavir to the CNS using Compritol-based solid lipid nanoparticles.* Ther Deliv, 2011. **2**(1): p. 25-35.

103. Aji Alex, M.R., et al., *Lopinavir loaded solid lipid nanoparticles (SLN) for intestinal lymphatic targeting.* Eur J Pharm Sci, 2011. **42**(1-2): p. 11-8.

104. Baek, J.S., et al., *Solid lipid nanoparticles of paclitaxel strengthened by hydroxypropyl-beta-cyclodextrin as an oral delivery system.* Int J Mol Med, 2012. **30**(4): p. 953-9.

105. Paliwal, R., et al., *Effect of lipid core material on characteristics of solid lipid nanoparticles designed for oral lymphatic delivery.* Nanomedicine, 2009. **5**(2): p. 184-91.

106. Videira, M., A.J. Almeida, and A. Fabra, *Preclinical evaluation of a pulmonary delivered paclitaxel-loaded lipid nanocarrier antitumor effect.* Nanomedicine, 2012. **8**(7): p. 1208-15.

107. Sun, M., et al., *Quercetin-nanostructured lipid carriers: Characteristics and anti-breast cancer activities in vitro.* Colloids Surf B Biointerfaces, 2014. **113**: p. 15-24.

108. Luan, J., et al., *Design and characterization of Amoitone B-loaded nanostructured lipid carriers for controlled drug release.* Drug Deliv, 2013. **20**(8): p. 324-30.

109. Zhang, X.Y., et al., *Preparation of isoliquiritigenin-loaded nanostructured lipid carrier and the in vivo evaluation in tumor-bearing mice.* Eur J Pharm Sci, 2013. **49**(3): p. 411-22.

110. Shete, H., et al., *Long chain lipid based tamoxifen NLC. Part II: pharmacokinetic, biodistribution and in vitro anticancer efficacy studies.* Int J Pharm, 2013. **454**(1): p. 584-92.

111. Hsu, S.H., et al., *Formulation design and evaluation of quantum dot-loaded nanostructured lipid carriers for integrating bioimaging and anticancer therapy.* Nanomedicine (Lond), 2013. **8**(8): p. 1253-69.

112. Bondi, M.L., et al., *Nanostructured lipid carriers-containing anticancer compounds: preparation, characterization, and cytotoxicity studies.* Drug Deliv, 2007. **14**(2): p. 61-7.

113. Patel, A.R., et al., *Efficacy of aerosolized celecoxib encapsulated nanostructured lipid carrier in non-small cell lung cancer in combination with docetaxel.* Pharm Res, 2013. **30**(5): p. 1435-46.

114. Endo, K., et al., *Tumor-targeted chemotherapy with the nanopolymer-based drug NC-6004 for oral squamous cell carcinoma.* Cancer Sci, 2013. **104**(3): p. 369-74.

115. Qin, L., et al., *Polymeric micelles for enhanced lymphatic drug delivery to treat metastatic tumors.* J Control Release, 2013. **171**(2): p. 133-42.

116. Rafi, M., et al., *Polymeric micelles incorporating (1,2-diaminocyclohexane)platinum (II) suppress the growth of orthotopic scirrhous*

gastric tumors and their lymph node metastasis. J Control Release, 2012. **159**(2): p. 189-96.

117. Wang, Z., et al., *LyP-1 modification to enhance delivery of artemisinin or fluorescent probe loaded polymeric micelles to highly metastatic tumor and its lymphatics.* Mol Pharm, 2012. **9**(9): p. 2646-57.

118. Luo, G., et al., *LyP-1-conjugated nanoparticles for targeting drug delivery to lymphatic metastatic tumors.* Int J Pharm, 2010. **385**(1-2): p. 150-6.

119. Zhou, L., et al., *In vivo antitumor and antimetastatic activities of camptothecin encapsulated with N-trimethyl chitosan in a preclinical mouse model of liver cancer.* Cancer Lett, 2010. **297**(1): p. 56-64.

120. Rao, D.A., et al., *Biodegradable PLGA based nanoparticles for sustained regional lymphatic drug delivery.* J Pharm Sci, 2010. **99**(4): p. 2018-31.

121. Hawley, A.E., L. Illum, and S.S. Davis, *Preparation of biodegradable, surface engineered PLGA nanospheres with enhanced lymphatic drainage and lymph node uptake.* Pharm Res, 1997. **14**(5): p. 657-61.

122. Lu, H., et al., *Paclitaxel nanoparticle inhibits growth of ovarian cancer xenografts and enhances lymphatic targeting.* Cancer Chemother Pharmacol, 2007. **59**(2): p. 175-81.

123. Manolova, V., et al., *Nanoparticles target distinct dendritic cell populations according to their size.* Eur J Immunol, 2008. **38**(5): p. 1404-13.

124. Hawley, A.E., L. Illum, and S.S. Davis, *Lymph node localisation of biodegradable nanospheres surface modified with poloxamer and poloxamine block co-polymers.* FEBS Lett, 1997. **400**(3): p. 319-23.

125. Liggins, R.T., et al., *Paclitaxel loaded poly(L-lactic acid) microspheres for the prevention of intraperitoneal carcinomatosis after a surgical repair and tumor cell spill.* Biomaterials, 2000. **21**(19): p. 1959-69.

126. Choi, H.S., et al., *Preparation and characterization of fentanyl-loaded PLGA microspheres: in vitro release profiles.* Int J Pharm, 2002. **234**(1-2): p. 195-203.

127. Azouz, S.M., et al., *Prevention of local tumor growth with paclitaxel-loaded microspheres.* J Thorac Cardiovasc Surg, 2008. **135**(5): p. 1014-21.

128. Liu, J., et al., *Translymphatic chemotherapy by intrapleural placement of gelatin sponge containing biodegradable Paclitaxel colloids controls lymphatic metastasis in lung cancer.* Cancer Res, 2009. **69**(3): p. 1174-81.

129. Tawde, S.A., et al., *Formulation and evaluation of oral microparticulate ovarian cancer vaccines.* Vaccine, 2012. **30**(38): p. 5675-81.

130. Coppi, G. and V. Iannuccelli, *Alginate/chitosan microparticles for tamoxifen delivery to the lymphatic system.* Int J Pharm, 2009. **367**(1-2): p. 127-32.

131. Yang, F., et al., *Magnetic functionalised carbon nanotubes as drug vehicles for cancer lymph node metastasis treatment.* Eur J Cancer, 2011. **47**(12): p. 1873-82.

132. Yang, D., et al., *Hydrophilic multi-walled carbon nanotubes decorated with magnetite nanoparticles as lymphatic targeted drug delivery vehicles.* Chem Commun (Camb), 2009(29): p. 4447-9.

133. Oussoren, C. and G. Storm, *Liposomes to target the lymphatics by subcutaneous administration.* Adv Drug Deliv Rev, 2001. **50**(1-2): p. 143-56.

134. Nishioka, Y. and H. Yoshino, *Lymphatic targeting with nanoparticulate system.* Adv Drug Deliv Rev, 2001. **47**(1): p. 55-64.

135. Hawley, A.E., S.S. Davis, and L. Illum, *Targeting of colloids to lymph nodes: influence of lymphatic physiology and colloidal characteristics.* Adv Drug Deliv Rev, 1995. **17**(1): p. 129-48.

136. Strieth, S., et al., *Paclitaxel encapsulated in cationic liposomes increases tumor microvessel leakiness and improves therapeutic efficacy in combination with Cisplatin.* Clin Cancer Res, 2008. **14**(14): p. 4603-11.

137. Tejada-Berges, T., et al., *Caelyx/Doxil for the treatment of metastatic ovarian and breast cancer.* Expert Rev Anticancer Ther, 2002. **2**(2): p. 143-50.

138. Frenkel, V., et al., *Delivery of liposomal doxorubicin (Doxil) in a breast cancer tumor model: investigation of potential enhancement by pulsed-high intensity focused ultrasound exposure.* Acad Radiol, 2006. **13**(4): p. 469-79.

139. Prescott, L.M., *Doxil offers hope to KS sufferers.* J Int Assoc Physicians AIDS Care, 1995. **1**(11): p. 43-4.

140. O'Brien, M.E., et al., *Reduced cardiotoxicity and comparable efficacy in a phase III trial of pegylated liposomal doxorubicin HCl (CAELYX/Doxil) versus conventional doxorubicin for first-line treatment of metastatic breast cancer.* Ann Oncol, 2004. **15**(3): p. 440-9.

141. Pan, X.Q., H. Wang, and R.J. Lee, *Antitumor activity of folate receptor-targeted liposomal doxorubicin in a KB oral carcinoma murine xenograft model.* Pharm Res, 2003. **20**(3): p. 417-22.

142. Khato, J., E.R. Priester, and S.M. Sieber, *Enhanced lymph node uptake of melphalan following liposomal entrapment and effects on lymph node metastasis in rats.* Cancer Treat Rep, 1982. **66**(3): p. 517-27.

143. Vaage, J., et al., *Therapy of a xenografted human colonic carcinoma using cisplatin or doxorubicin encapsulated in long-circulating pegylated stealth liposomes.* Int J Cancer, 1999. **80**(1): p. 134-7.

144. Lawson, K.A., et al., *Novel vitamin E analogue and 9-nitro-camptothecin administered as liposome aerosols decrease syngeneic mouse mammary tumor burden and inhibit metastasis.* Cancer Chemother Pharmacol, 2004. **54**(5): p. 421-31.

145. Latimer, P., et al., *Aerosol delivery of liposomal formulated paclitaxel and vitamin E analog reduces murine mammary tumor burden and metastases.* Exp Biol Med (Maywood), 2009. **234**(10): p. 1244-52.

146. Lopes, S.C.d.A., et al., *Liposomes as Carriers of Anticancer Drugs*. Cancer Treatment - Conventional and Innovative Approaches, ed. L. Rangel. 2013.

147. *Liposome*. [cited 2014 Feburaray 6]; Available from: http://www.britannica.com/EBchecked/media/92244/Phospholipids-can-be-used-to-form-artificial-structures-called-liposomes.

148. Laakkonen, P., et al., *A tumor-homing peptide with a targeting specificity related to lymphatic vessels.* Nat Med, 2002. **8**(7): p. 751-5.

149. Laakkonen, P., et al., *Antitumor activity of a homing peptide that targets tumor lymphatics and tumor cells.* Proc Natl Acad Sci U S A, 2004. **101**(25): p. 9381-6.

150. Fogal, V., et al., *Mitochondrial/cell-surface protein p32/gC1qR as a molecular target in tumor cells and tumor stroma.* Cancer Res, 2008. **68**(17): p. 7210-8.

151. Thurston, G., et al., *Cationic liposomes target angiogenic endothelial cells in tumors and chronic inflammation in mice.* J Clin Invest, 1998. **101**(7): p. 1401-13.

152. Cai, S., et al., *Intralymphatic chemotherapy using a hyaluronan-cisplatin conjugate.* J Surg Res, 2008. **147**(2): p. 247-252.

153. Niu, C., et al., *Doxorubicin loaded superparamagnetic PLGA-iron oxide multifunctional microbubbles for dual-mode US/MR imaging and therapy of metastasis in lymph nodes.* Biomaterials, 2013. **34**(9): p. 2307-17.

154. Maincent, P., et al., *Lymphatic targeting of polymeric nanoparticles after intraperitoneal administration in rats.* Pharm Res, 1992. **9**(12): p. 1534-9.

155. Cohen, M.S., et al., *A Novel Intralymphatic Nanocarrier-Delivery System for Cisplatin Therapy in Breast Cancer with Improved Tumor Efficacy and Lower Systemic Toxicity In Vivo.* Am J Surg, 2009. **198**(6): p. 781-6.

156. Cai, S., et al., *Pharmacokinetics and disposition of a localized lymphatic polymeric hyaluronan conjugate of cisplatin in rodents.* J Pharm Sci, 2010. **99**(6): p. 2664-71.

157. Croy, S.R. and G.S. Kwon, *Polymeric micelles for drug delivery.* Curr Pharm Des, 2006. **12**(36): p. 4669-84.

158. Deng, C., et al., *Biodegradable polymeric micelles for targeted and controlled anticancer drug delivery: Promises, progress and prospects.* Nano Today, 2012. **7**(5): p. 467-80.

159. Murakami, H., et al., *Preparation of poly(DL-lactide-co-glycolide) nanoparticles by modified spontaneous emulsification solvent diffusion method.* Int J Pharm, 1999. **187**(2): p. 143-52.

160. Govender, T., et al., *PLGA nanoparticles prepared by nanoprecipitation: drug loading and release studies of a water soluble drug.* J Control Release, 1999. **57**(2): p. 171-85.

161. Mainardes, R.M. and R.C. Evangelista, *PLGA nanoparticles containing praziquantel: effect of formulation variables on size distribution.* Int J Pharm, 2005. **290**(1-2): p. 137-44.

162. Wang, Y.M., et al., *Preparation and characterization of poly(lactic-co-glycolic acid) microspheres for targeted delivery of a novel anticancer agent, taxol.* Chem Pharm Bull (Tokyo), 1996. **44**(10): p. 1935-40.

163. Jalil, R. and J.R. Nixon, *Microencapsulation using poly(L-lactic acid). I: Microcapsule properties affected by the preparative technique.* J Microencapsul, 1989. **6**(4): p. 473-84.

Chapter 2

Functional *In Vivo* Imaging Apoptotic Cancer Cell using Molecular Probes

1. Introduction

Noninvasive imaging techniques are necessary for early cancer detection and evaluation of the chemotherapeutic effect on tumors. Current diagnostic imaging techniques generally include γ -scintigraphy, magnetic resonance imaging, computed tomography, and ultrasonography; however, these techniques only give morphological information on the tumor. These techniques do not report the biochemical response of the tumor to treatment and physical changes in the tumor in response to treatment may take days to weeks to fully manifest. Positron emission topography and SPECT can indirectly detect tumor response to treatment due to changes in metabolic activity and blood perfusion, respectively. However, no clinical imaging technique can directly detect the biochemical response, e.g., apoptosis, of tumors to treatment. Typically anti-cancer agents act on cancer cells to induce apoptosis, so apoptosis is a rapid and definite indicator of tumor response. Since apoptosis often occurs within in the first 18 to 36 h after treatment, direct imaging of apoptosis would rapidly indicate if there is a response in the tumor to chemotherapy.

Apoptosis is the process of programmed cell death by which multicellular organisms regulate cell number and maintain homeostasis. Within the series of biochemical events

involved in apoptosis, the activation of caspase family of cysteine proteases has been recognized as a critical marker. Apoptosis can be triggered by extrinsic or intrinsic signals such as physiological activators (TNF family, neurotransmitters, calcium, glucocorticoids), damage-related inducers (heat shock, viral infection, tumor suppressors p53, oxidants, free radicals), therapy-associated agents (chemotherapeutic agents, gamma radiation and UV radiation) and toxins (ethanol, β - amyloid peptide) [1-5]. Defective apoptosis processes can lead to severe pathological disorders, for example, down-regulated apoptosis is involved in autoimmune diseases, cancer and viral infections [6, 7]; abnormal upregulation of apoptosis is associated with AIDS, neurodegenerative disorders and ischemic injury [7, 8]. Therefore, the development of caspase inhibitors could be novel treatments for a variety apoptosis associated diseases.

A number of peptidyl caspase inhibitors have been developed including peptidyl chloromethyl ketones, peptidyl fluoromethyl ketones and peptidyl aldehydes. The chloromethyl ketones have strong electrophilicity and are not stable to high concentrations of thiol, which limits their use in vivo [9]. The aldehyde based inhibitors are poorly cell permeable and are not effective caspase inhibitors under concentrations of 1 μ M [10]. The fluoromethyl ketone (FMK) inhibitors, which are more stable in vivo and cell permeable [10, 11], act as broad-spectrum, irreversible caspase inhibitors [12] with no added

cytotoxic effects. Inhibitors synthesized with a benzyloxycarbonyl group (such as Boc- or Z-) at the N-terminus and O-methyl side chains such as Z-Val-Ala-Asp (OMe)-FMK display improved cellular permeability facilitating their use in both in vitro cell culture and in vivo animal studies [13, 14].

Photoacoustic imaging (PAI) overcomes the spatial and resolution limitations of conventional imaging techniques at a relatively low cost [15, 16], and it has shown its potential to monitor the growth of melanoma brain tumors [17] and melanoma metastasis in sentinel lymph nodes [18]. However, ascribed to the fact that PAI utilizes the optical absorption of tissues for contrast, it cannot differentiate normal from cancerous cells unless the cells are overexpressing chromomeric marker (e.g., melanomas) or labeled by reporter moieties as contrast agent to enhance the contrast between normal and pathological tissues. In this case, contrast agents such as fluorochromes with absorption and emission maxima wavelengths between 650 and 900 nm (within the near-infrared range) are ideally suited for imaging in tissue due to the minimal optical absorption from hemoglobin, water, and lipids over this range [19-21]. These fluorochromes are expected to facilitate both the visualization of head and neck squamous cell carcinoma (HNSCC) cancer cells and their response to treatment in vivo by PAI with a significant benefit over current commercial cell caspase imaging agents, such as FLIVO™, which use fluorophores

wavelengths less than 600 nm, e.g. fluorescein and rhodamine, where there is significantly more tissue autofluorescence and optical attenuation.

We reported herein an imaging agent containing a near-infrared (NIR) fluorochrome IR780 with high quantum yield and a cell permeable fluoromethyl ketone of the tripeptides valine, alanine, and O-methyleglutamic acid [Val-Ala-Glu (OMe)-FMK], which specifically and irreversibly binds to the cysteine residue at the active site of caspase-9 [12]. In this study, we first demonstrated the sensitivity of IR780-linker-Val-Ala-Glu (OMe)-FMK imaging probe for cell apoptosis via in vitro cell-imaging with prostate cancer DU 145 cells, followed by evaluating the application of the imaging probe for PAI to detect procaspase-9 activation caused by anticancer drug treatment in living nude mice bearing HNSCC tumors.

2 Materials and Methods

2.1 Materials

All chemicals were obtained from Sigma-Aldrich (St. Louis, MO, USA) and used as received unless stated otherwise. Solvents were distilled under argon immediately before

use. Dichloromethane (DCM), N,Ndimethylformamide (DMF) and triethylamine (TEA) were freshly distilled from CaH_2, and tetrahydrafuran (THF) was freshly distilled from sodium benzophenone. Camptothecin was purchased from Natland International Corporation (Morrisville, NC, USA). Human prostate cancer cell line DU145 was kindly provided by Dr. Benyi Li, The University of Kansas Medical Center (Kansas City, Kansas, USA). The human oral squamous carcinoma cell line, MDA-1986, was a gift from Dr. Jeffrey Myers (University of Texas, M.D. Anderson Cancer Center; Houston, TX). Dulbecco's Modified Eagle's Medium and trypsin-EDTA were purchased from Life Technologies (Grand Island, NY, USA). Fetal bovine serum (U.S.D.A Origin) was purchased from Biowest LLC (Kansas City, MO, USA). Double distilled water was used in syntheses, characterization and cell-culture (sterilized by autoclaving).

2.2 Methods

2.2.1 Synthesis of IR780-linker-Val-Ala-Glu (OMe)-FMK

The NIR fluorescent imaging agent 4′ C-[4-[2-(fluoromethylketone-Ala-Val-NH)carbonyl]ethyl]carbonyl]amino]butyl]amino-IR780 [IR780-linker-Val-Ala-Glu(OMe)-

FMK] (compound 10) was synthesized in 11 steps shown in Scheme 1. Reactions were carried out under dry argon with flame-dried glassware.

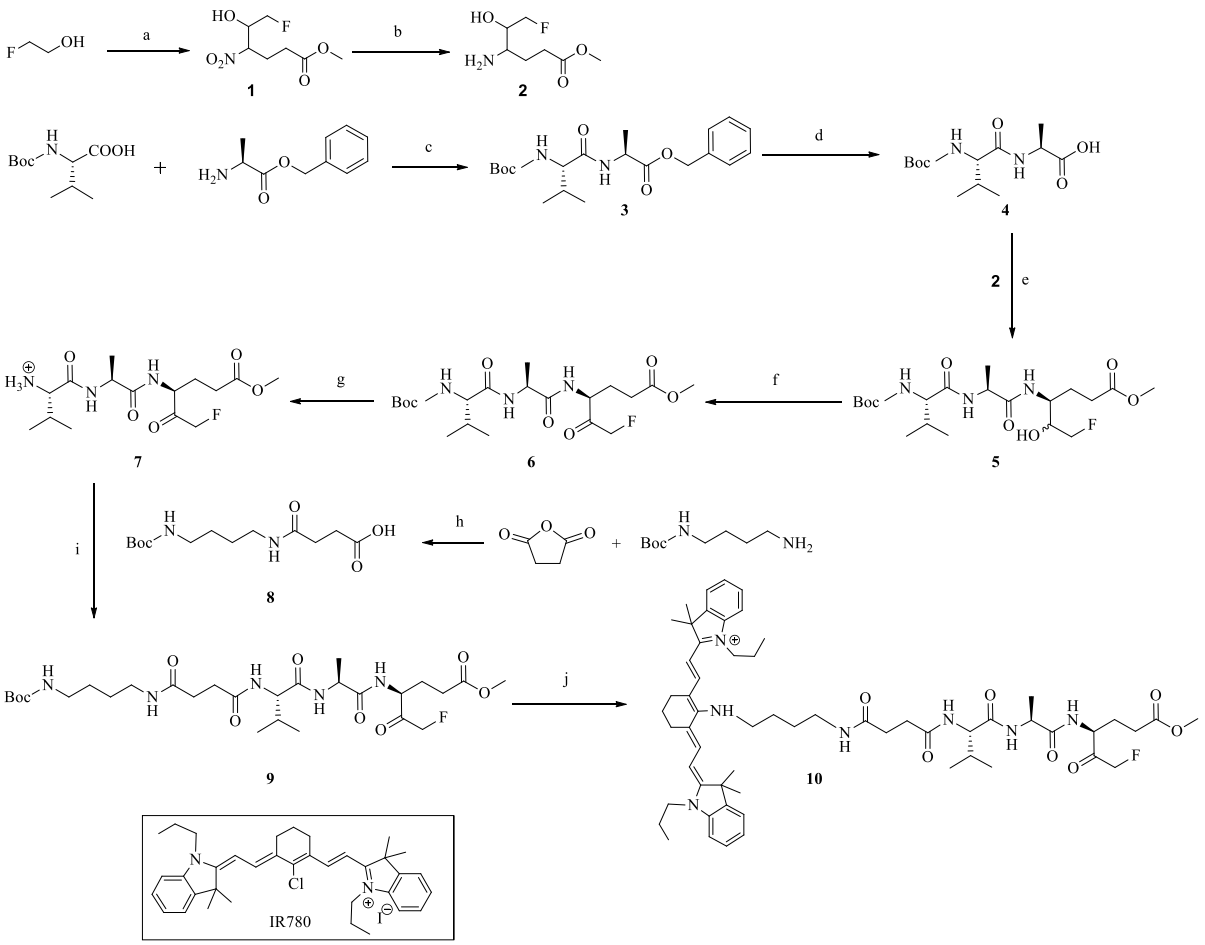

Scheme 1. Synthetic scheme of IR780-linker-Val-Ala-Glu (OMe)-FMK imaging agent

Reagents: a) i, Swern oxidation; ii, methyl 4-nitrobutyrate, TEA; b) 10% Pd/C, H2, in MeOH; c) TEA, HBTU, DMF; d) 10% Pd/C, H2, in THF; e) EDCI, DMAP, THF; f) Dess-Martin periodinane, in DCM; g) 4M HCl/EtOAc; h) 1,4-dioxan, DMAP, reflux; i) EDCI, HOBt, DMAP, THF; j) i, 4M HCl/EtOAc; ii, IR 780, TEA, DMF.

6-Fluoro-5-hydroxy-4-nitrohexanoic acid methyl ester (compound 1)

Anhydrous DMSO (1.4 mL, 19 mmol) was added dropwise to the solution of oxalyl chloride (0.9 mL, 9.6 mmol) in DCM (5 mL) at −78°C. To this solution was added 2-fluoroethanol (0.44 mL, 7.5 mmol) in DCM (2 mL). Fifteen minutes later, the reaction mixture was diluted with DCM (60 mL), followed by addition of TEA (4.4 mL, 31 mmol). The mixture was allowed to warm up to 0°C and stirred for 2 h followed by the addition of methyl 4-nitrobutyrate (0.93 g, 6.3 mmol) in DCM (5 mL). The mixture was stirred at 0°C for 3 h and then ambient temperature (ca. 20°C) overnight (23). The solution was concentrated and washed with ethyl acetate (EtOAc). Removal of the solvent followed by purification by silica gel column (hexanes: EtOAc = 5:1) gave the desired compound (1.0 g, 76%) as yellow viscous oil.

4-Amino-6-fluoro-5-hydroxyhexanoic acid methyl ester (compound 2) A solution of 6-fluoro-5-hydroxy-4-nitrohexanoic acid methyl ester (compound 1, 1.15 g, 5.5 mmol) in methanol (20 mL) and acetic acid (0.5 mL) was hydrogenated with H2 (40-45 psi) at ambient temperature for 5 h using 10% Pd/C (0.5 g) catalyst. The Pd/C was filtered off and the solvent was evaporated under reduced pressure. The desired compound was obtained as colorless viscous oil (0.92 g, yield 87%), which was used for the next step without further purification.

Boc-Val-Ala-OBn (compound 3) Boc-Val (3.0 g, 13.8 mmol), alanine benzyl ester hydrochloride salt (3.3 g, 15.3 mmol) and O-benzotriazole-N, N, N', N'-tetramethyl-uronium-hexafluoro-phosphate (HBTU, 5.76 g, 15.3 mmol) were dissolved in DMF (100 mL) followed by addition of TEA (4.3 mL). The reaction was stirred at ambient temperature for 24 h and then diluted with saturated citric acid (100 mL). Then the mixture was washed with EtOAc (100 mL × 2), and the combined organic layers were washed with brine, saturated NaHCO3 and brine, respectively, and then dried over Na2SO4. Removal of the solvent under reduced pressure followed by purification on silica gel (EtOAc: hexanes = 1:3) gave the desired compound (4.48 g, 86%) as a white solid.

Boc-Val-Ala-COOH (compound 4) Boc-Val-Ala-OBn (Compound 3, 5.0 g, 12.7 mmol) was dissolved in THF (100 mL), and the solution was hydrogenated with H2 (1 atm) using 10% Pd/C catalyst (0.50 g) for 24 h. The solid Pd/C was removed by filtration, and the solvent was evaporated under reduced pressure. The desired compound was obtained as a white solid (3.4 g, 82%).

4-(Boc-Val-Ala-amido)-6-fluoro-5-hydroxylhexa-noic acid methyl ester (compound 5) Boc-Val-Ala-COOH (compound 4, 1.0 g, 3.5 mmol), 4-dimethyla-minopyridine (DMAP, 0.25 g, 1.9 mmol), and N -(3-dimethylaminopropyl)-N -

ethylcarbodiimide hydrochloride (EDAC, 0.74 g, 3.9 mmol) were dissolved in anhydrous THF (10 mL) at ambient temperature. After 10 min a solution of 4-amino-6-fluoro-5-hydroxyhexanoic acid methyl ester (compound 2, 0.69 g, 3.9 mmol) in anhydrous THF (10 mL) was added directly to the above solution, and the reaction was stirred at ambient temperature overnight. The solvent was removed under reduced pressure, and the residue was dissolved in EtOAc, washed with saturated NaHCO3, brine, and citric acid, respectively. The organic layer was dried with Na2SO4, and the product was purified over silica gel (EtOAc: hexanes = 3:1) to give the desired compound as a white solid (0.5 g, 32%).

4-(Boc-Val-Ala-amido)-6-fluoro-5-oxohexanoic acid methyl ester (compound 6) A solution of compound 5 (0.898 g, 2.0 mmol) in DCM (20 mL) was treated with Dess - Martin periodinane solution (20 mL, 0.3 M in DCM). The reaction mixture was stirred at ambient temperature for 12 h. The solvent was removed under reduced pressure, and the crude product was purified by silica gel chromatography (EtOAc: hexanes = 1:1) to give the desired compound as a white solid (0.749 g, 81%).

4-(Val-Ala-amido)-6-fluoro-5-oxohexanoic acid methyl ester [Val-Ala-Glu(OMe)] (compound 7) A solution of 4-M HCl in anhydrous EtOAc (20 mL) was cooled to 0°C, 4-(Boc-Val-Alaamido)-6-fluoro-5-oxohexanoic acid methyl ester (compound 6,

0.749 g, 1.62 mmol) was added, and the mixture was stirred at ambient temperature overnight. Collection of the precipitated solid followed by washing with EtOAc (50 mL) gave a pale yellow solid (0.564 g, quantitative yield), which was directly used for the next step without further purification.

4-(4-(Tert-butoxycarbonyl)ethylamino)-4-oxobutanoic acid (Boc-linker, compound 8) Mono-Boc-protected butane-1, 4-diamine (2.82 g, 15 mmol; prepared according to previous reports [22, 23]) in 10 mL of dioxane was added slowly to a solution of succinic anhydride (1.5 g, 15 mmol) in 10 mL of dioxane and then stirred at 80°C for 3 h. Removal of the solvent followed by purification of the residue through silica gel chromatography (EtOAc: hexanes:acetic acid = 50:5:1) gave the desired compound as a white solid (2.64 g, 63%).

Boc-linker-Val-Ala-Glu(OMe)-FMK (compound 9) To a solution of compound 8 (1.44 g, 5.0 mmol) in THF (30 mL) was added N - (3-dimethylaminopropyl)-N-ethylcarbodiimide hydrochloride (EDCI, 0.96 g, 5.0 mmol), 1-hydroxybenzotriazole (HOBt; 0.68 g, 5.0 mmol), and 4-dimethylaminopyridine (DMAP) (0.31 g, 2.5 mmol). The mixture was stirred for 10 min at ambient temperature followed by the addition of compound 7 (2.24 g, 5.0 mmol) in THF (15 mL). The mixture was stirred at ambient temperature

overnight. After removing the solvent under reduced pressure, the residue was diluted with EtOAc (100 mL) and washed with brine (50 mL). The organic layer was dried over sodium sulfate the solvent was removed under reduced pressure. Purification of the residue by silica gel chromatography (EtOAc: MeOH = 20:1) gave the desired compound as a yellow solid (1.17 g, 38%).

IR780-linker-Val-Ala-Glu (OMe)-FMK (compound 10) To a solution of Boc-linker-Val-Ala-Glu (OMe)-FMK (compound 9, 0.46 g, 0.75 mmol) in dry DMF (5 mL) was added a solution of 4-M HCl/EtOAc (10 mL) at 0°C. The mixture was stirred for 12 h at ambient temperature, followed by the addition of TEA (55 µL, 0.75 mmol) and IR780 iodide (0.1 g, 0.15 mmol) in dry DMF (5 mL) [24, 25]. The mixture was then heated to 85°C and stirred continuously for 24 h in the dark. Removal of the solvent followed by purification of the obtained residue through silica gel chromatography (CHCl3: MeOH = 50:1) gave the desired compound as a blue solid (0.038 g, 25%).

2.2.2 Spectral properties of IR780-linker-Val-Ala-Glu (OMe)-FMK

The fluorescent spectrum of a 1-µM solution of IR780-linker-Val-Ala-Glu(OMe)-FMK in DMSO was recorded using a Shimadzu RF-5301 PC spectrofluorophotometer. The Stokes

shift was determined by the difference in wavelength between excitation and emission maxima. The quantum yield was measured according to a reported protocol [26, 27] using cresyl violet as a reference.

2.2.3 TUNEL assay

DU145 cells were treated with 1 μ M of camptothecin as described for 24 h and then were fixed in freshly prepared 4% paraformaldehyde in PBS, pH 7.4, for 1 h at ambient temperature. After washing with PBS, cells were permeabilized with 0.1% Triton X-100 in 0.1% sodium citrate for 2 min on ice. Cells were incubated with TUNEL reaction mixture (Roche Diagnostics, Indianapolis, IN, USA) at 37°C in a humidified atmosphere for 1 h. Samples were directly imaged under a Nikon Eclipse 80i microscope coupled with a Hamamatsu ORCA-ER digital camera at 465-495 nm excitation and 515 - 555 nm emission.

2.2.4 Western blotting

DU145 cells were treated with 1 μ M of camptothecin as described in the previous section, and cell lysates were prepared with a solution of 1% Nonidet P-40, 50-mM Tris,

150-mM NaCl, APL protease inhibitors, and PMSF adjusted to pH 7.4. After treatment, floating cells were collected by aspiration, and attached cells were collected by trypsinization followed by centrifugation at 350 × g for 5 min. Cell pellets were incubated with lysis buffer on ice for 20 min and then centrifuged at 3,000 × g for 20 min at 4°C. The protein concentration was determined by BCA assay. Samples (40 μ g of protein/sample) were separated by 10% polyacrylaminde gel and then transferred onto 0.45-μ m nitrocellulose membrane, which was then blocked with 5% (w/v) non-fat milk in TBS and 0.1% Tween 20 (TBS/T). After washing with TBS/T, the nitrocellulose membrane was incubated with the anti-caspase-9 polyclonal antibody (diluted 1:1,000, Cell Signaling Technology #9502, Danvers, MA, USA) overnight at 4°C, followed by horseradish peroxidase-conjugated secondary antibody (diluted 1:2,000, Santa Cruz Biotechnology #sc-2004, Santa Cruz, CA, USA) for 1 h at ambient temperature. Proteins were visualized with the Western Lightening® ECL detection system from Perkin Elmer.

2.2.5 Cell imaging for apoptosis

The DU145 cell line was cultured in Dulbecco's Modified Eagle's Medium supplemented with 10% fetal bovine serum and 1% L-glutamine. Cells were seeded into an

8-chamber culture slide at a density of 40,000 per well, and after overnight incubation, they were treated with or without 1 μM of camptothecin. After 24 h, IR780-linker-Val-Ala-Glu (OMe)-FMK (compound 10) or IR780 iodide at different concentrations (0.1, 0.2, 0.5 and 1.0 μM) was applied, and the cells were incubated at 37°C for 30 min. Fresh MEM medium was exchanged once every hour for 3 h. The cells were washed once with sterile phosphate buffered saline (PBS) for fluorescent imaging using a Nikon Eclipse 80i microscope coupled with a Hamamatsu ORCA-ER digital camera. The fluorescent images were analyzed using the MetaMorph software.

For the nuclear counterstain, DU145 cells were seeded onto a 12-mm coverslip in 6-well plate at a density of 1.5×10^5 cells per well for overnight. After cells were treated with or without 1 μ M of camptothecin for 24 h, IR780-linker-Val-Ala-Glu (OMe)-FMK at concentrations of 0.1 or 0.5 μ M was incubated with cells for 30 min at 37°C. Then the cells were washed twice with sterile PBS and subsequently incubated with 5-μ g/mL DAPI in MEM for at 37°C for 5 min. Finally, the cells were washed with sterile PBS twice and imaged using the system described above.

The acute toxicity of the IR780-linker-Val-Ala-Glu (OMe)-FMK in cell culture was determined by incubating the cells with the imaging agent for 30 min and then measuring

the ratio of dead to live (attached cells). DU145 cells had been seeded at 1.5×10^5 cells/well in a 6-well plate and allowed to attach overnight before addition of the imaging agent.

2.2.6 Tumor model

Female Nu/Nu mice used in the experiments were maintained under the supervision and guidelines of the University of Kansas Institutional Animal Care and Use Committee. Animals were fed on a diet of low chlorophyll feed for at least two weeks before imaging. Human HNSCC cells, MDA1986, were prepared in 1 × PBS solution at a cell concentration of 2×10^7 cells/mL. Nude mice were anesthetized with 1.5% isoflurane in oxygen-air mixture (50:50). Fifty microliters of cell suspension was injected into the sub-mucosa of a mouse using a 30-ga needle. Primary HNSCC tumors were observed on the cheek of the animals two weeks after implantation with a size range of 5 to 150 mm3 [tumor volume = 0.52 × (width) 2 × (length)]. Animals were euthanized at the completion of the study.

2.2.7 Treatments and fluorescent imaging

Female nude mice bearing head and neck tumors were randomly divided into two groups, including cisplatin treatment and control groups. One dose of 10.0-mg/kg cisplatin (LC Laboratories) was intravenously administered via the tail vein to the animals in the treatment group once the tumor size was between 40 to 50mm^3. The control group received no treatment. NIR-FMK (25 nmol in 100-μL of saline) was intravenously injected via the tail vein into a tumor-negative mouse, and systemic clearance of the dye was evaluated by fluorescent imaging (CRI Maestro Flex, CRI Inc., Woburn, Massachusetts) throughout 5 min to 24 h. A 575 to 605-nm filtered halogen excitation light and a 645-nm long pass emission filter were applied. Fluorescence intensity in the abdominal area was measured using a cooled chargecoupled- device (CCD) camera with auto exposure. The unscaled images were normalized to the same exposure and the brightness and constrast were adjusted for print.

2.2.8 *In vivo* photoacoustic imaging

Figure 1 illustrates the schematic of the PAI system. The mechanism of the PAI system was previously described[16, 17] and is identical to the system presented by Song et al [15]. A tunable OPO laser (Surelite OPO PLUS; Continuum, Santa Clara, California)

pumped by a Q-switchedNd:YAGlaser (Surelite; Continuum, Santa Clara, California) is used to generate the laser pulse with a repetition rate of 10 Hz and a laser wavelength of 680 nm. The laser light, directed by a prism group, forms a ring-shaped illumination on an optical condenser and is then refocused by a conical lens on the targeted area. The produced photoacoustic signals are collected by a 5-MHz single-element focused ultrasonic transducer (SU-108-013, Sonic Concepts, Bothell, Washington), amplified by a pre-amplifier (5072PR, Olympus-NDT, Waltham, Massachusetts), and finally collected by a personal computer through an A/D Scope Card (CS21G8 - 256MS, Gage, Lockport, Illinois) with a 125-MHz sampling rate to reconstruct 2-D images. The 5-MHz ultrasonic transducer (fractional bandwidth of 60%, 35-mm focal length, and 33-mm aperture size) is mounted in the center of the condenser and driven by a step motor to scan over the targeted region. It takes ca. 20 min to scan a 20 mm × 20 mm area. Previous work [16, 17] on this system has shown that it has a lateral resolution of 270 μm and an axial resolution of 220 μm.

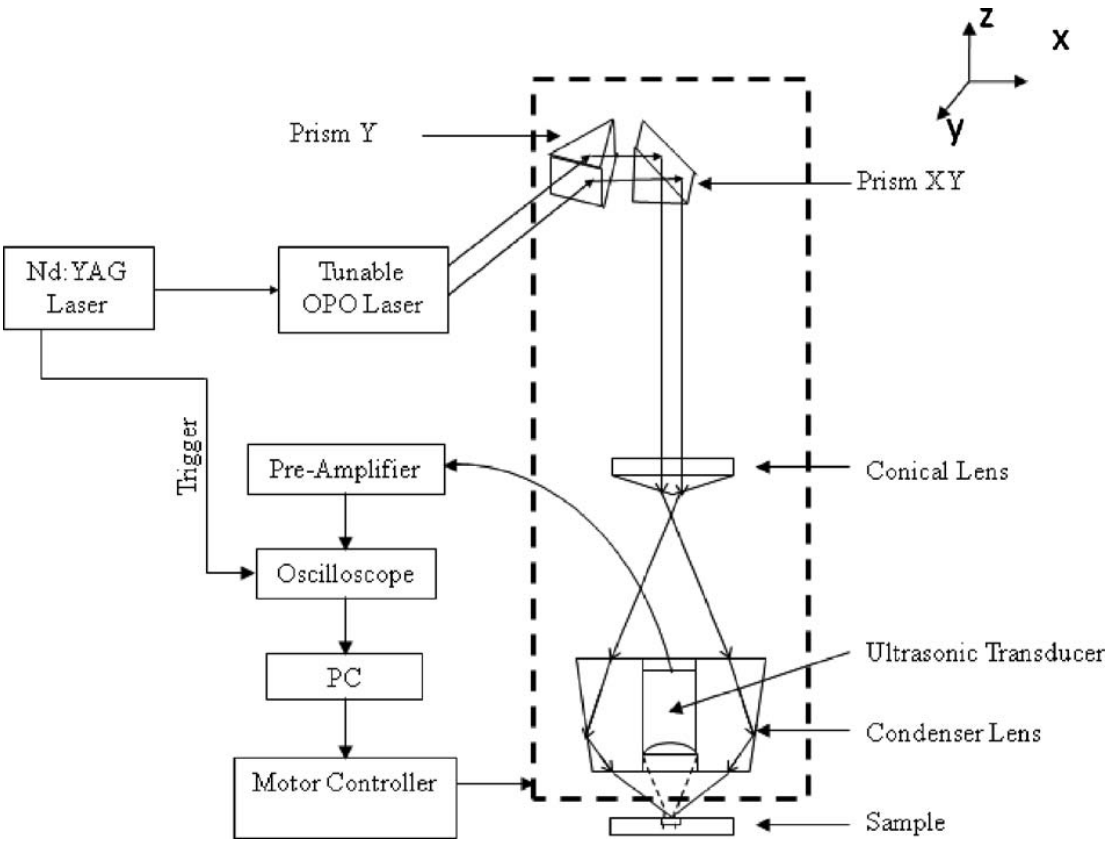

Figure 1. Schematic of Photoacoustic Imaging system

Twenty-four hours post-treatment with cisplatin, mice were positioned as shown in Figure 2 and anesthetized by inhalation of a mixture of 1% isoflurane and pure oxygen at 1-L/min flow rate. The initial background photoacoustic (PA) images were obtained around the tumor region on the cheek of the mouse and then NIR-FMK (25 nmol in 100 μL of saline) was intravenously injected via the tail vein. PA images were acquired at 2, 4, 6, and 8 h. A laser wavelength of 680 nm was used during the imaging, and the imaging depth was 2 to 3 mm. Signal intensity was analyzed using Fiji/ImageJA software (ver. 20110307, http://pacific.mpicbg.de/wiki/index.php/Fiji).

2.2.9 Immunostaining for apoptosis

The HNSCC tumor was excised within several hours after PAI. Subsequently, it was embedded into tissue freezing medium (Triangle Biomedical Sciences, Durham, North Carolina) and sectioned using a cryostat (Thermo Shandon Limited, Kalamazoo, Michigan). Fourteen-micron (thickness) sections of the tumor tissue were stained with a goat primary polyclonal antibody for cleaved caspase-3 p11 subunit (Asp-175-Ser-176) and a donkey anti-goat secondary antibody with a fluorescein isothiocyanate (FITC) fluorophore (Santa

Cruz Biotechnology Inc., Santa Cruz, California). Cell nuclei were stained with 4,6-diamidino-2-phenylindole (DAPI).

3. Results and Discussion

3.1 Synthesis of IR780-linker-Val-Ala-Glu (OMe)-FMK

We successfully synthesized the NIR fluorescent imaging agent [IR780-linker-Val-Ala-Glu (OMe)-FMK] in 11 steps with an overall yield 0.75%. The structure of each compound was determined by 1 H-NMR or together with APCI-MS (ESI-MS). NMR spectra were taken on a 400-MHz Bruker with the TMS peak as internal reference. Mass spectra were run in the electrospray ionization mass spectrometry (ESI-MS) mode or atmospheric pressure chemical ionization (APCI-MS) mode. Optically pure starting materials were used in the synthesis; however, isomers may have been introduced during the synthesis at the three chiral centers. During the purification of compound 5, only the major compound was collected, a pair of enantiomers, which resulted in the low yield of 32%. The enantiomers were not separated further before proceeding.

Compound 1: ^{1}H-NMR (400 MHz, CDCl3): 2.40 - 2.45 (m, 4H), 3.69 (s, 3H), 4.20 (brs) and 4.25 (brs, 1H), 4.40 - 4.80 (m, 3H), 5.02 (brs) and 5.19 (brs, 1H).

Compound 2: ^{1}H-NMR (400 MHz, MeOD): 1.65-2.00 (m, 2H), 2.90-3.42 (m, 2H), 3.65 (s, 3H), 3.66-3.3.95 (m, 2H), 4.41 - 4.55 (m, 2H).

Compound 3: ^{1}H-NMR (400 MHz, CDCl3): 0.93 (d, J = 7.0 Hz, 3H), 0.97 (d, J = 6.8 Hz, 3H), 1.44 (d, J = 7.2 Hz, 3H), 1.46 (s, 9H), 2.08-2.20 (m, 1H), 3.94 (t, J = 7.6 Hz, 1H), 4.62-4.69 (m, 1H), 5.08 (d, J = 8.8, 1H), 5.19 (dd, J = 12.3, 8.2 Hz, 2H), 6.44 (d, J = 5.8 Hz, 1H), 7.32-7.44 (m, 5H).

Compound 4: ^{1}H-NMR (400 MHz, CDCl3): 0.92 (d, J = 6.7 Hz, 3H), 0.96 (d, J = 6.7 Hz, 3H), 1.42-1.47 (m, 12H, overlap), 2.00-2.11 (m, 1H), 4.01 (t, J = 8.0 Hz, 1H), 4.57 (t, J = 7.0 Hz, 1H), 5.51 (brs, 1H), 7.04 (brs, 1H), 9.66 (brs, 1H).

Compound 5: APCI -MS: [M + 1] = 450.3, [M + 1-C4H8] = 394.2, [M-Boc] = 350.2. 1H-NMR (400 MHz, CDCl3): 0.95 (d, J = 7.0 Hz, 3H), 0.98 (d, J = 6.6 Hz, 3H), 1.40 (d, J = 7.6 Hz, 3H), 1.45 (s, 9H), 1.85-1.97 (m, 2H), 2.08-2.18 (m, 1H), 2.41 (t, J = 7.2 Hz, 2H), 3.69 (s, 3H), 3.83-3.95 (m, 1H), 3.96-4.10 (m, 1H), 4.29-4.55 (m, 3H), 6.54 (brs, 1H), 6.58 (brs, 1H).

Compound 6: APCI-MS: [M + 1] = 448.3, [M + 1-C4H8] = 392.2, [M-Boc] = 348.2. 1H-NMR (400 MHz, CDCl3): 0.95 (d, J = 7.0 Hz, 3H), 0.99 (d, J = 6.6 Hz, 3H), 1.40 (d, J = 7.6 Hz, 3H), 1.45 (s, 9H), 1.88-1.96 (m, 2H), 2.12-2.22 (m, 1H), 2.43 (t, J = 7.2 Hz, 2H), 3.68 (s, 3H), 3.87-3.99 (m, 1H), 4.46-4.59 (m, 1H), 5.09-5.21 (m, 2H), 6.76 (brs, 1H), 7.37 (brs, 1H).

Compound 8: ^{1}H-NMR (400 MHz, MeOD): 1.46 (s, 9H), 1.46-1.57 (m, 4H), 2.39-2.50 (m, 2H), 2.55-2.67 (m, 2H), 3.06 (t, J = 4.6 Hz, 2H), 3.19 (t, J = 6.5 Hz, 2H), 6.53 (brs, 1H), 7.90 (brs, 1H), 12.10 (brs, 1H).

Compound 9: APCI-MS: [M + 1] = 618.7, [M-Boc] = 518.5. 1H-NMR (400 MHz, CDCl3): 0.95 (d, J = 7.0 Hz, 3H), 0.99 (d, J = 6.6 Hz, 3H), 1.40 (d, J = 7.6 Hz, 3H), 1.46 (s, 9H), 1.47-1.55 (m, 4H), 1.67-1.78 (m, 2H), 2.14-2.26 (m, 1H), 2.39-2.50 (m, 4H), 2.55-2.68 (m, 2H), 3.07 (t, J = 4.7 Hz, 2H), 3.20 (t, J = 6.4, 2H), 3.68 (s, 3H), 4.08-4.20 (m, 1H), 4.45-4.58 (m, 1H), 4.48-4.59 (m, 1H), 4.99-5.30 (m, 2H), 6.19 (brs, 1H), 6.50 (brs, 1H), 7.45 (brs, 1H), 7.53 (brs, 1H), 7.56 (brs, 1H).

Compound 10: ESI-MS: [M+ 1] = 1022.3. 1H-NMR (400 MHz, DMSO-d6): 0.95 (d, J = 7.0 Hz, 3H), 0.98 (d, J = 6.6 Hz, 3H), 1.03-1.07 (m, 6H), 1.32-1.41 (m, 2H), 1.42-1.51 (m, 5H), 1.52-1.57 (m, 4H), 1.59-1.70 (m, 15H), 1.71-1.76 (m, 4H), 2.07-2.15 (m, 2H), 2.18-2.27 (m, 1H), 2.34 (t, J = 7.2 Hz, 2H), 2.49 (t, J = 6.8 Hz, 2H), 2.57 (t, J = 6.8 Hz, 2H), 2.83 (t, J = 7.5 Hz,

4H), 2.89 (t, J = 6.8 Hz, 2H), 3.05 (t, J = 6.8 Hz, 2H), 3.64 (s, 3H), 3.79 (t, J = 6.8, 2H), 3.94 (t, J = 7.2 Hz, 2H), 4.10-4.20 (m, 1H), 4.26-4.37(m, 1H), 4.48-4.56 (m, 1H), 5.13-5.25 (m, 2H), 5.86 (d, J = 13.0 Hz, 2H), 7.06-7.15 (m, 4H), 7.29-7.36 (m, 1H), 7.62-7.71 (m, 1H), 7.77 (d, J = 13.0 Hz, 2H), 8.13-8.25 (m, 2H).

3.2 Absorption and emission spectrum of IR780-linker-Val-Ala-Glu (OMe)-FMK

The structure of IR780-linker-Val-Ala-Glu (OMe)-FMK consists of three parts: the IR780 fluorophore, the linker, and the fluoromethyl ketone of the tripeptides valine, alanine, and Omethyle-glutamic acid [Val-Ala-Glu (OMe)-FMK] as the reactive part to the caspase-9. IR780-linker-Val-Ala-Glu (OMe)-FMK had a maximum excitation at 650 nm (Figure 2) and emission at 729 nm respectively. By contrast, the λmax of unconjugated IR780 dye was at 685 and 760 nm for excitation and emission, respectively. The fluorescence quantum yield (Φ) was calculated as 0.75, which was determined in methanol with reference compound cresyl violet (Φ = 0.54 in methanol [28]). The quantum yield is high enough to be employed as a fluorescent label in cell imaging studies.

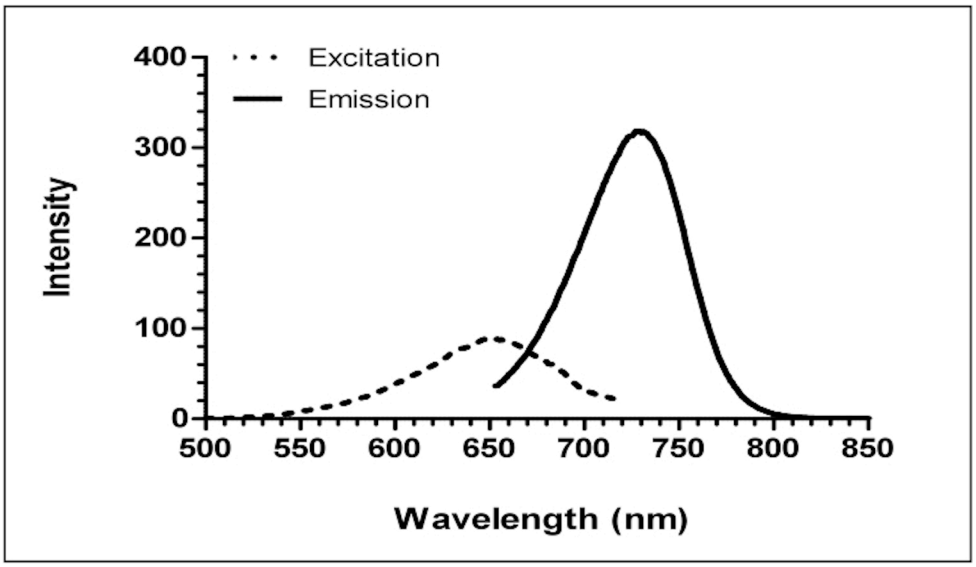

Figure 2. Excitation (dashed) and emission (solid) spectrum of IR780-linker-Val-Ala-Glu (OMe)-FMK.

3.3 Camptothecin induces apoptosis via activation of caspases-9

The caspase proteases can be activate either though the death signal-induced or stress-induced pathways. Caspase-9 is an activator of apoptosis in the mitochondrion-mediated or stress-induced pathway, wherein it subsequently activates caspases-3/6/7. Caspase-9 can be bypassed in the death signal-induced pathway when death receptors (e.g. TNF receptor) activate caspases-3/6/7 directly via caspase-10 [29]. Camptothecin inhibits DNA synthesis and was expected to induce apoptosis via the caspase-9 pathway. After treatment with camptothecin, TUNEL assay indicated DNA fragmentation characteristic of apoptosis (Figure 3) and immunoblotting found cleaved caspase-9 fragments (Figure 4), which are the target of the IR780-linker-Val-Ala-Glu (OMe)-FMK imaging agent.

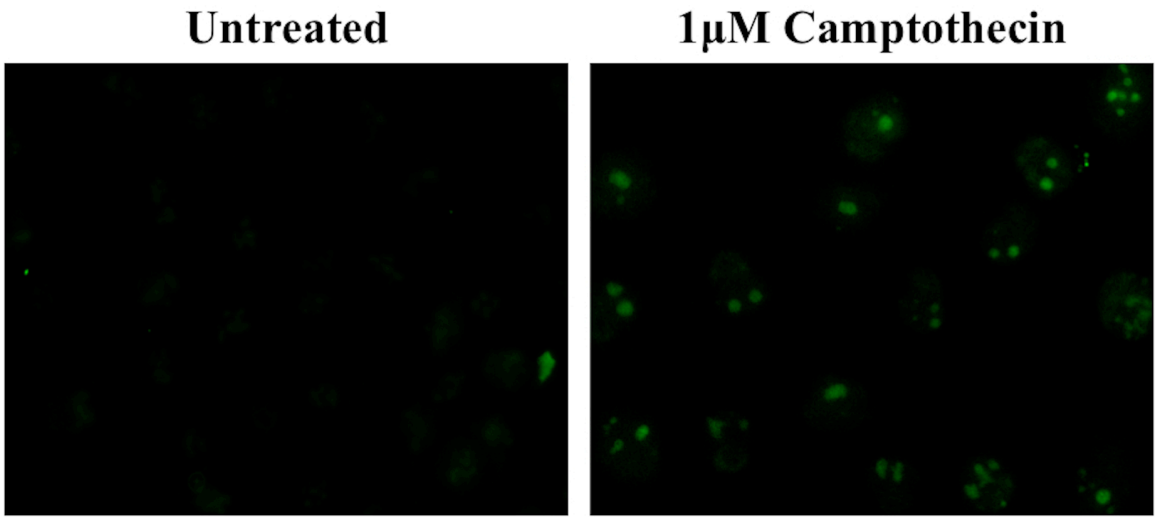

Figure 3. TUNEL assay. Apoptotic DU145 cells that have been treated with 1 μM camptothecin for 24 h were labeled by TUNEL staining of the DNA fragments. In comparison, untreated cells did not undergo apoptosis.

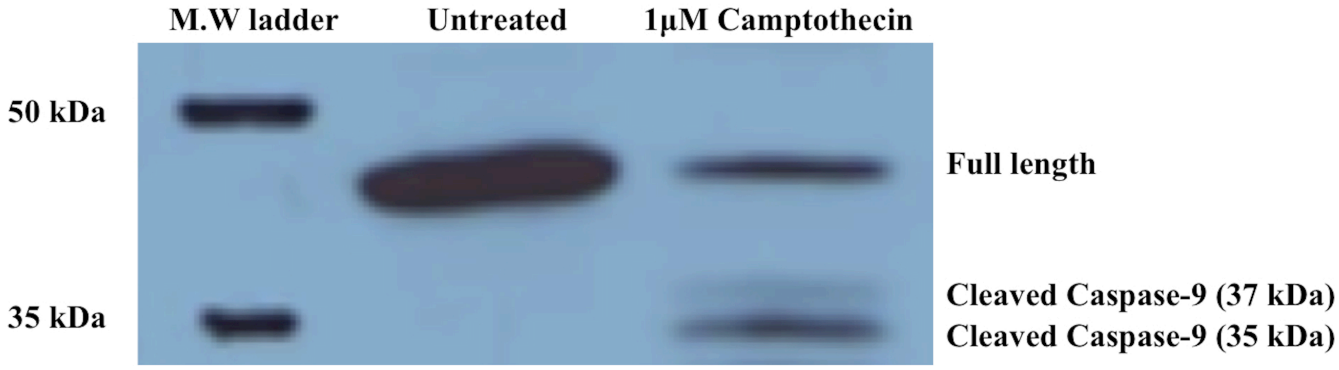

Figure 4. Western blot analysis of caspase-9 cleavage in untreated DU145 cells, or cells treated with 1-μM camptothecin for 24 h. (a) full length; (b) cleaved caspase-9 (37 kDa); (c) cleaved caspase-9 (35 kDa

The normal DU145 cells had no uptake of IR780 dye in the tested concentration range (0.1-1 μM). The unconjugated IR780 dye is highly polar and impregnable to cell membrane, and we did not observe nonspecific uptake of the unconjugated IR780 dye in normal or apoptotic DU145 cells (images not shown). DU145 cells undergoing apoptosis showed fluorescent signals, because IR780-linker-Val-Ala-Glu (OMe)-FMK bound to the cleaved caspase-9 induced by camptothecin, which caused it to be retained within the cells (Figures 5D, E, and F). Furthermore, counter-staining of the cells with DAPI confirmed that the IR780-linker-Val-Ala-Glu (OMe)-FMK was confined to the cytoplasm (Figure 6). The inhibition and binding of IR780-linker-Val-Ala-Glu (OMe)-FMK to cleaved caspase-9 is a result of the peptide sequence recognition and the nucleophilic substitution of the fluoro-group by a sulfhydryl group of the cysteine protease [30]. By contrast, after untreated DU145 cells (~ 90% cell confluence) were incubated with IR780-linker-Val-Ala-Glu (OMe)-FMK, there was no accumulation of fluorescence either on the cell membrane or inside the cells at 0.1- or 0.2-μM IR780-Val-Ala-Glu (OMe)-FMK concentrations (Figures 5A and 5B). However, there was a small amount of fluorescence detected when the cells were incubated with 0.5-μM IR780-linker-Val-Ala-Glu (OMe)-FMK (Figure 5C). This was probably due to the high cell confluence (~ 90%) used for the imaging, as this non-specific binding was not observed in the cells at 60% confluency used for the DAPI counterstaining (Figure 6), and

the imaging agent alone was not toxic. When the cells were incubated with the imaging agent for 30 min, there were no statistically significant differences in cell death between 0, 0.1 and 0.5 μM of agent, which resulted in 3.17 ± 0.85, 3.01 ± 1.17, and 3.34 ± 1.01% dead cells, respectively.

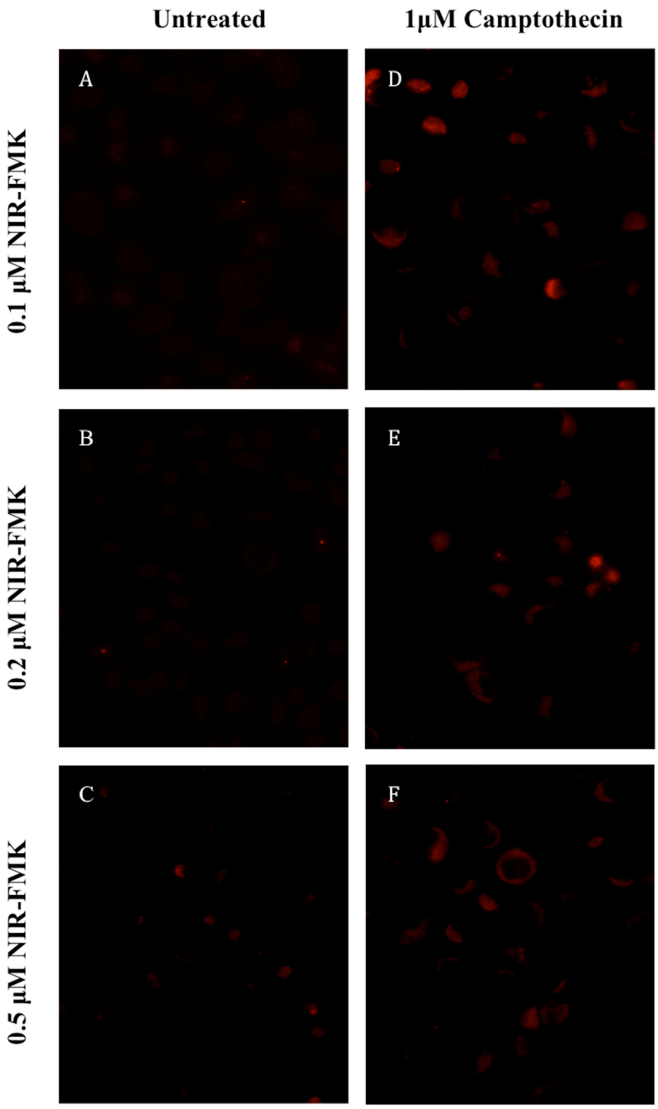

Figure 5. DU145 cell imaging after treatment with IR780-linker-Val-Ala-Glu(OMe)-FMK at concentrations of: A) 0.1 μM; B) 0.2 μM; C) 0.5 μM; IR780-linker-Val-Ala-Glu(OMe)-FMK with 1 μM of camptothecin at concentrations of: D) 0.1 μM; E) 0.2 μM; F) 0.5 μM.

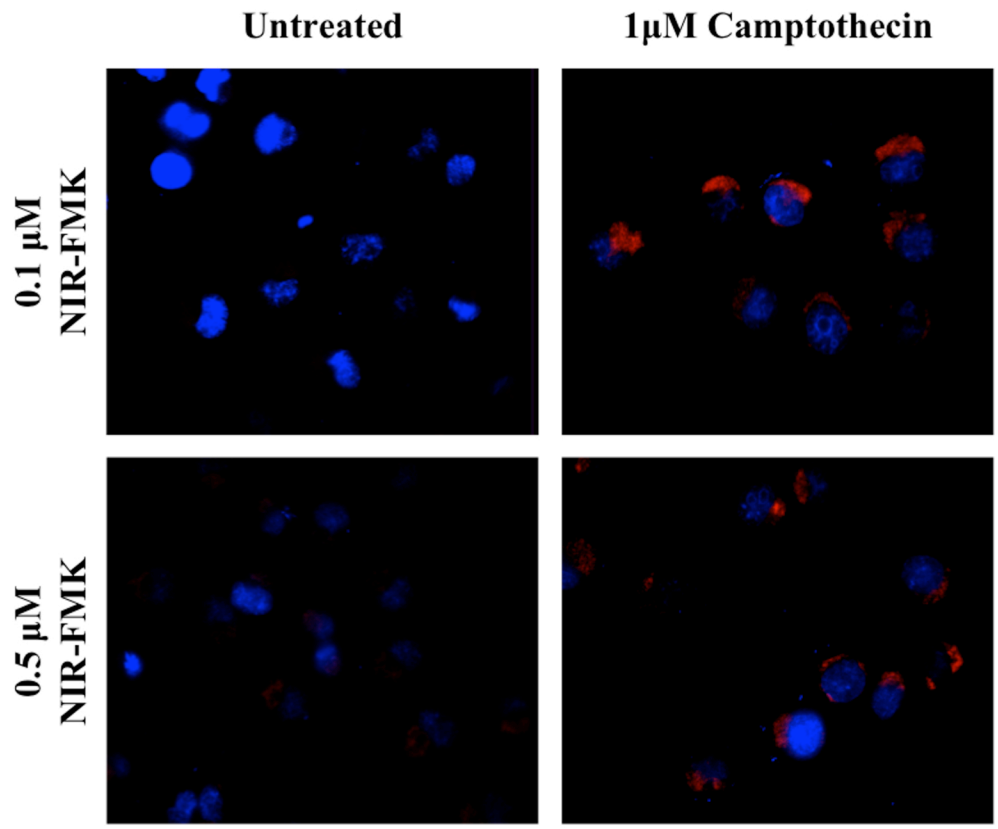

Figure 6. Fluorescent microscopic images of IR780-linker-Val-Ala-Glu(OMe)-FMK-stained DU145 cells; DAPI counter stain. The IR780-linker-Val-Ala-Glu(OMe)-FMK fluorescent label (red) is distributed within the cytoplasm of the cells.

3.4 *In vivo* fluorescent imaging of tumor-free mice treated with IR780-linker-Val-Ala-Glu (OMe)-FMK

Systemic clearance of the imaging agent from a tumor-free mouse was evaluated by injecting animals with 25 nmol of NIR-FMK via their tail vein and fluorescently imaging animals from 5 min to 24 h. Fluorescence signals in the abdominal area shown in Figure 7 indicated that NIR-FMK was retained by the liver within the first 5 min after injection, with later distribution to the small intestines and spleen. Organ fluorescence decreased to background or auto-fluorescence levels after eight hours, indicating that the agent had been completely cleared from the body. The kinetics of clearance of NIR-FMK served to assist with determining the time course of PA imaging on tumor-positive mice. Within the first hour, the liver had cleared the imaging agent from the systemic circulation, offering a favorable time frame for PA imaging to differentiate the imaging agents bound to the tumor tissue from the free agent distributed in the tissue space. In addition, considering the imaging resolution and patients' comfort in future clinical applications, we performed the PA imaging at 2, 4, 6, and 8 h after intravenous injection.

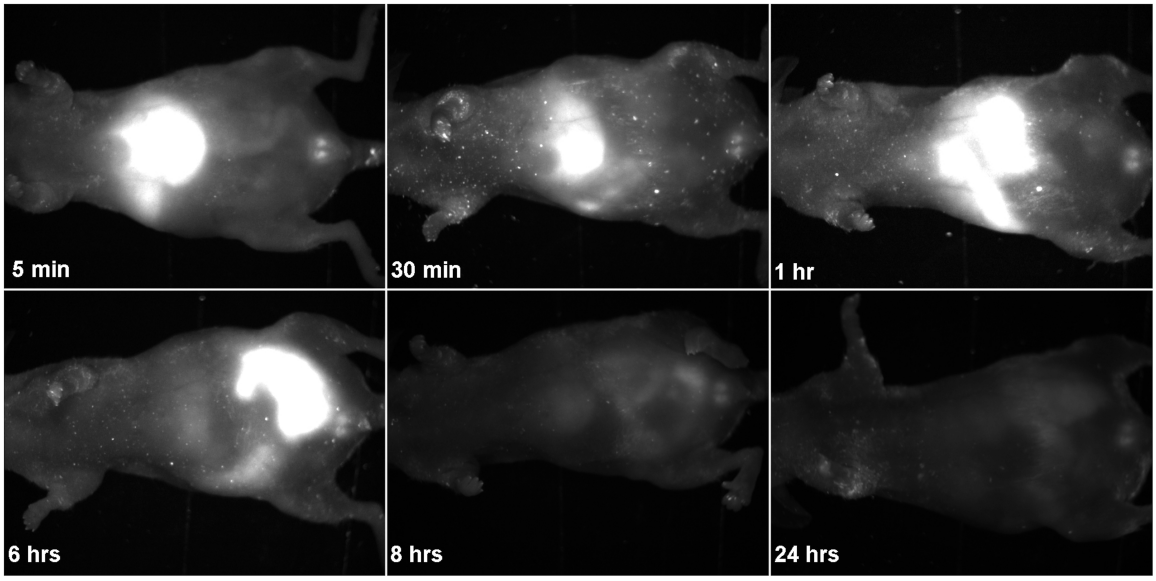

Figure 7. Fluorescent images of the systemic clearance of NIR-FMK constrast agent. Animal was fluorescently imaged after tail vein injection of 25 nmol of NIR-FMK. Agent was rapidly cleared from the systemic circulation and was concentrated in the liver from 5 to 30 min and in the intestines from 1 to 6 h.

3.5 *In vivo* photoacoustic imaging of chemotherapy-induced apoptosis in squamous cell carcinoma

Maximum amplitude projection images obtained from the PAI of the HNSCC tumor region shown in Figure 8 were converted to grayscale images. The grayscale images at various time points were linearly aligned using the scale-invariant feature transform function of Fiji/ImageJA software (ver. 20110307, http://pacific.mpi-cbg.de/wiki/index.php/Fiji) (Figure 9). Quantification of PA signal intensity within the tumor region was performed in triplet for each image by measuring the mean gray value (units: gray/pixel) of the circled tumor region. The extent of signal enhancement was calculated by normalizing the tumor signal against a background reading taken immediately before injection of the imaging agent (Figure 8), and the process can be indicated with the following equation:

Increase in PA signal = [(intensity of each time point−intensity of background image)/intensity of background imaging] × 100%.

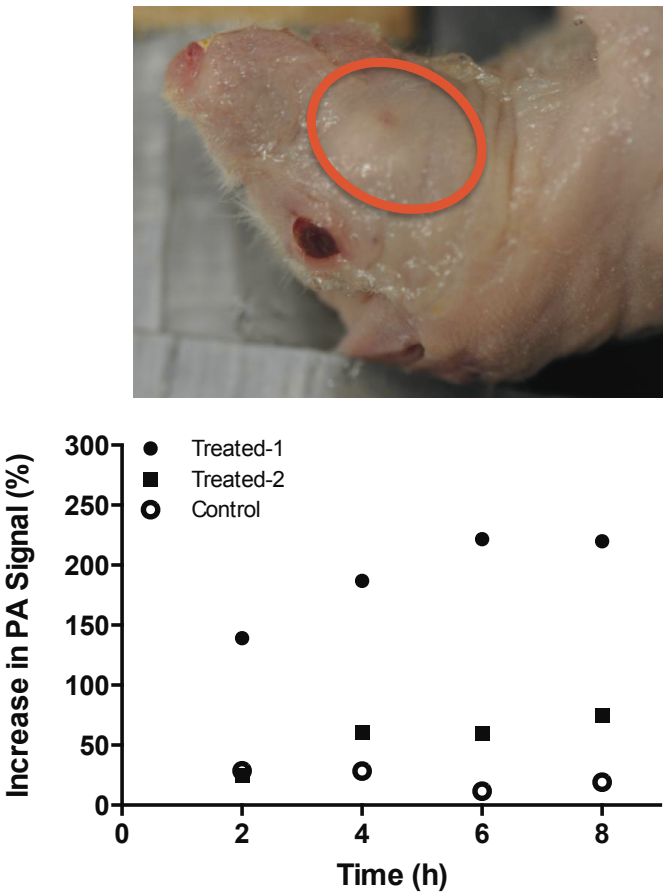

Figure 8. Increase in PA amplitude within the HNSCC tumor after intravenous injection of imaging agent via the tail vein. The treated animals (n = 2) were intravenously given 10 mg/kg of cisplatin 24 h prior to administration of the imaging agent. PAI images were centered on the tumor (circle, bottom). Images of the control animal (n = 1) at the optimal imaging depth were chosen for data analysis.

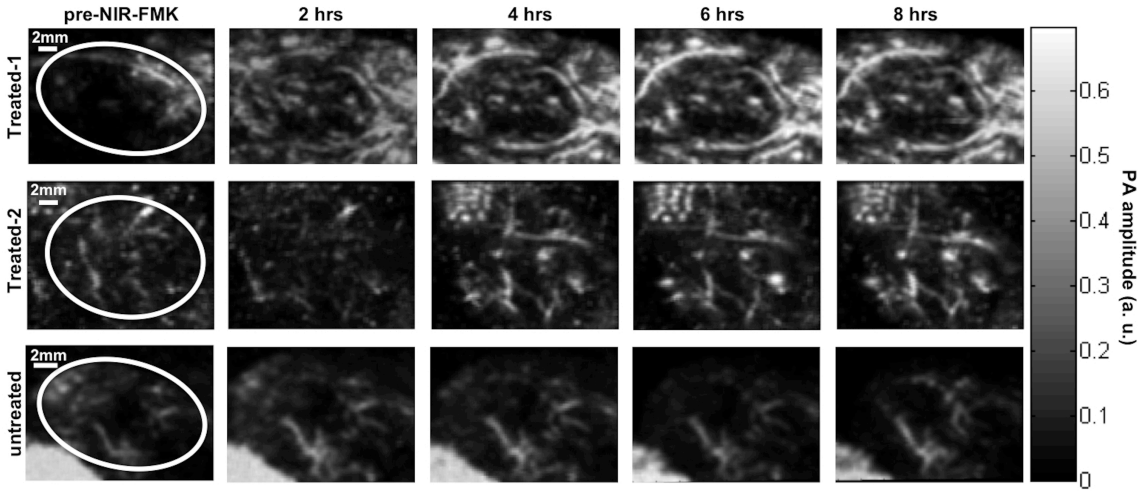

Figure 9. PA images of HNSCC tumor apoptosis after contrast treatment. Animals were administered 25 nmol of NIR-FMK via the tail vein. Intravenous cisplatin (10 mg/kg) was administered 24 h prior to imaging in the treatment group.

The signal intensity within the tumor region of each frame (denoted by a white circle in Figure 9) was compared with other frames in the same time series between the treated and control groups. The same scaling was used for all images within the series. The triangle-shaped white region in the lower left corner of the control group images in Figure 10 is noise from a piece of paper used to cover the right eye, which is outside of the HNSCC tumor region. The signal of the mouse in the control group reached the maximum intensity at 2 h and after that it began to drop. This indicated that the imaging probe was nonspecifically distributed to the tumor tissues after injection, and the agent then cleared with the systemic circulation as observed in the fluorescence studies (Figure 7). By comparison, PA images of the treatment group demonstrated enhanced signal intensity during the same time course. The significant difference between control and cisplatin treatment groups could be explained by the specific and irreversible binding between NIR-FMK and caspase 9 in the tumor tissue. In cisplatin treated mice, apoptosis of HNSCC cancer cells resulted in the activation of caspase 9 around the tumor, serving as binding sites for the imaging probe and allowing the probe to accumulate.7 Since the control group did not receive the chemotherapy treatment, caspase 9 was not activated due to the lack of the cell apoptosis process and the imaging probe was rapidly cleared from the tumor.

Diffuse contrast on the peripheral of the tumor region in the treated group is likely due to apoptosis of metastatic cells on the margins of the solid primary tumor mass.

3.6 Immunostaining of sliced tumor for apoptosis

Apoptosis in the tumor tissues was independently verified by immunohistochemical staining for caspase 3, a downstream indicator of apoptosome-activated caspase-mediated apoptosis that would not cross-react with the caspase-9 PA probe. Figure 10(a) represents a control section stained with the secondary antibody alone (autofluorescence of the tissue without apparent staining); while, Figure 10 (b) shows the immunostaining of the caspase-3 p11 subunit (green) and the DAPI staining of cell nuclei. The intense green fluorescence in these sections suggests the wide spread apoptosis of cells in the tumor tissues after intravenous administration of high-dose cisplatin. In addition, cells on the peripheral of the tumor stained more strongly for caspase 3 (green fluorescence) compared to cells at the tumor interior. This was consistent with the PA imaging of apoptosis that showed strong apoptosis at the tumor peripheral, suggesting chemotherapeutics had penetrated the outer layers of the tumor and induced apoptosis.

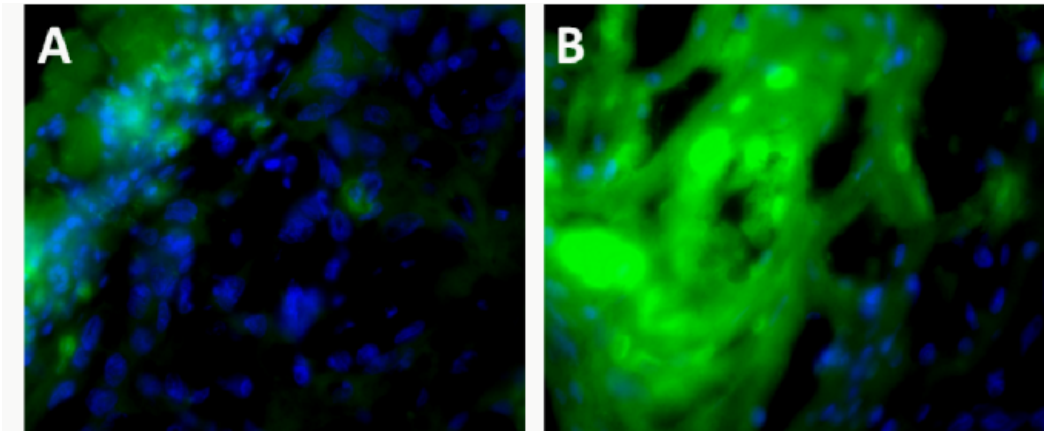

Figure 10. Immunostaining for apoptosis in tumor. (A) representative control section stained with secondary antibody alone, and (B) tissue section of the HNSCC tumor stained for caspase-3 p11 subunit after cisplatin treatment. Green FITC fluorescence indicates the presence of apoptotic cells, and blue DAPI indicates the cell nuclei.

4. Conclusions

In conclusion, the synthesis of a new NIR fluorescent imaging agent [IR780-Val-Ala-Glu (OMe)-FMK] for caspase-9 was successfully accomplished in 11 steps (0.75% overall yield), which has a maxima excitation at 650 nm and emission at 729 nm. The in vitro cell imaging has demonstrated the sensitivity of this imaging agent for caspase-9-mediated cell apoptosis. At high confluences and dye concentrations, the dye uptake lost specificity. In addition, the cell-permeable imaging probe can be utilized to monitor cancer cell apoptosis in living mice by photoacoustic imaging with improved contrast.

5. References

1. Bosman, F.T., B.C. Visser, and J. van Oeveren, *Apoptosis: pathophysiology of programmed cell death.* Pathol Res Pract, 1996. **192**(7): p. 676-83.
2. Buttke, T.M. and P.A. Sandstrom, *Oxidative stress as a mediator of apoptosis.* Immunol Today, 1994. **15**(1): p. 7-10.
3. Reed, J.C., *Bcl-2 and the regulation of programmed cell death.* J Cell Biol, 1994. **124**(1-2): p. 1-6.

4. Sachs, L. and J. Lotem, *Control of programmed cell death in normal and leukemic cells: new implications for therapy.* Blood, 1993. **82**(1): p. 15-21.

5. Vaux, D.L., I.L. Weissman, and S.K. Kim, *Prevention of programmed cell death in Caenorhabditis elegans by human bcl-2.* Science, 1992. **258**(5090): p. 1955-7.

6. Hanahan, D. and R.A. Weinberg, *The hallmarks of cancer.* Cell, 2000. **100**(1): p. 57-70.

7. Thompson, C.B., *Apoptosis in the pathogenesis and treatment of disease.* Science, 1995. **267**(5203): p. 1456-62.

8. Yuan, J. and B.A. Yankner, *Apoptosis in the nervous system.* Nature, 2000. **407**(6805): p. 802-9.

9. Smith, R.E., et al., *Visualization of time-dependent inactivation of human tumor cathepsin B isozymes by a peptidyl fluoromethyl ketone using a fluorescent print technique.* Anticancer Res, 1988. **8**(4): p. 525-9.

10. Ekert, P.G., J. Silke, and D.L. Vaux, *Caspase inhibitors.* Cell Death Differ, 1999. **6**(11): p. 1081-6.

11. Yang, W., et al., *MX1013, a dipeptide caspase inhibitor with potent in vivo antiapoptotic activity.* Br J Pharmacol, 2003. **140**(2): p. 402-12.

12. Sadhukhan, R., et al., *An efficient method to express and refold a truncated human procaspase-9: a caspase with activity toward Glu-X bonds.* Protein Expr Purif, 2006. **46**(2): p. 299-308.

13. Guo, Y. and N. Kyprianou, *Restoration of transforming growth factor beta signaling pathway in human prostate cancer cells suppresses tumorigenicity via induction of caspase-1-mediated apoptosis.* Cancer Res, 1999. **59**(6): p. 1366-71.

14. Schlegel, J., et al., *CPP32/apopain is a key interleukin 1 beta converting enzyme-like protease involved in Fas-mediated apoptosis.* J Biol Chem, 1996. **271**(4): p. 1841-4.

15. Song, K.H. and L.V. Wang, *Deep reflection-mode photoacoustic imaging of biological tissue.* J Biomed Opt, 2007. **12**(6): p. 060503.

16. Cui, H., J. Staley, and X. Yang, *Integration of photoacoustic imaging and high-intensity focused ultrasound.* J Biomed Opt, 2010. **15**(2): p. 021312.

17. Staley, J., et al., *Growth of melanoma brain tumors monitored by photoacoustic microscopy.* J Biomed Opt, 2010. **15**(4): p. 040510.

18. McCormack, D., et al., *Photoacoustic detection of melanoma micrometastasis in sentinel lymph nodes.* J Biomech Eng, 2009. **131**(7): p. 074519.

19. Wang, W., et al., *A new optical and nuclear dual-labeled imaging agent targeting interleukin 11 receptor alpha-chain.* Bioconjug Chem, 2007. **18**(2): p. 397-402.

20. Hilderbrand, S.A., et al., *Monofunctional near-infrared fluorochromes for imaging applications.* Bioconjug Chem, 2005. **16**(5): p. 1275-81.

21. Bouteiller, C., et al., *Novel water-soluble near-infrared cyanine dyes: synthesis, spectral properties, and use in the preparation of internally quenched fluorescent probes.* Bioconjug Chem, 2007. **18**(4): p. 1303-17.

22. Montero, A., et al., *Guanidinium and aminoimidazolinium derivatives of N-(4-piperidyl)propanamides as potential ligands for mu opioid and I2-imidazoline receptors: synthesis and pharmacological screening.* Bioorg Med Chem, 2002. **10**(4): p. 1009-18.

23. Unciti-Broceta, A., et al., *Synthesis, penetrability and intracellular targeting of fluorescein-tagged peptoids and peptide-peptoid hybrids.* Bioorg Med Chem, 2009. **17**(3): p. 959-66.

24. Strekowski, L., M. Lipowska, and G. Patonay, *Substitution reactions of a nucleofugal group in heptamethine cyanine dyes. Synthesis of an isothiocyanato derivative for labeling of proteins with a near-infrared chromophore.* J Org Chem, 1992. **57**(17): p. 4578-4580.

25. Masotti, A., et al., *A novel near-infrared indocyanine dye-polyethylenimine conjugate allows DNA delivery imaging in vivo.* Bioconjug Chem, 2008. **19**(5): p. 983-7.

26. Williams, A.T.R., S.A. Winfield, and J.N. Miller, *Relative fluorescence quantum yields using a computer-controlled luminescence spectrometer.* Analyst, 1983. **108**(1290): p. 1067-1071.

27. Dhami, S., et al., *PHTHALOCYANINE FLUORESCENCE AT HIGH CONCENTRATION: DIMERS OR REABSORPTION EFFECT?* Photochem Photobiol, 1995. **61**(4): p. 341-346.

28. Magde, D., et al., *Absolute luminescence yield of cresyl violet. A standard for the red.* J Phys Chem, 1979. **83**(6): p. 696-699.

29. Fan, T.J., et al., *Caspase family proteases and apoptosis.* Acta Biochim Biophys Sin, 2005. **37**(11): p. 719-27.

30. Haberkorn, U., et al., *Investigation of a potential scintigraphic marker of apoptosis: radioiodinated Z-Val-Ala-DL-Asp(O-methyl)-fluoromethyl ketone.* Nucl Med Biol, 2001. **28**(7): p. 793-8.

Chapter 3

Combining Hard and Soft Magnetism into A Single Core-Shell Nanoparticle to Achieve Both Hyperthermia and Image Contrast

1. Introduction

Engineered superparamagnetic iron oxide nanoparticles (SPINOs), including magnetite Fe_3O_4 and γ- Fe_2O_3, with elaborately tailored particle sizes and surface chemistry have been extensively studied as probes for magnetic resonance imaging (MRI) and magnetic hyperthermia treatment (MFH) due to their biocompatibility, ease in synthesis, and their FDA-approval for clinical usage. With recent advances in materials science and nanotechnology, the composition, crystallinity and magnetism of SPIONs can be modified to markedly enhance magnetic saturation [1, 2]. Therefore, SPIONs represents a powerful tool in the field of cancer theranostics that combines magnetic resonance imaging (MRI) and magnetic hyperthermia treatment (MHT) under extra alternating current magnetic fields[3-9]. However, a major challenge in the biomedical application of SPIONs for MHT is its moderate heating efficiency and lack of precise control of *in vivo* temperature evolution during the treatment [10].

In order to achieve strong MRI contrast sensitivity and sufficient heating efficacy for MHT, high magnetization is a prerequisite, which has led to the exploration of magnetic alloy nanoparticles including FePt [11, 12], FeCo[13, 14] and FePd [15]as new theranostics probes. The magnetic alloy nanoparticles have demonstrated enhanced magnetic properties, and compared to FeCo MNPs, FePt MNPs are more chemically stable against rapid oxidation in biological solutions[16]. Novel bi-magnetic core/shell nanostructures that incorporate magnetically soft materials (e.g. iron oxide, FeCo) and magnetically hard magnetic alloy nanoparticles

(MNPs) (e.g. FePt, FePd) take advantage of the intrinsic magnetic properties at both ends of the spectrum. These core/shell MNPs combine high magnetocrystalline anisotropy and saturated magnetization via the effective interfacial exchange coupling interaction between the two phases, affording cooperative magnetic switching and tunable magnetic properties [17, 18]. The enhanced magnetism can be further translated into a high thermal energy transfer capability, which is crucial for generating the high local temperatures needed for thermal abduction of tumor tissues [19] during the magnetically mediated hyperthermia. Compared with a clinically approved Fe_3O_4 MNPs formulation, Feridex®, a significant enhancement of magnetic heat induction has been reported in exchange-coupled $CoFe_2O_4$ @$MnFe_2O_4$, which were intradumorally injected and led to the complete tumor eradication after local hyperthermia [20]. Although high concentration of MNPs within the tumor region can be achieved by local administration, direct injection is invasive and not amenable to suppress small metastatic tumor growth, presenting a severe practical challenge. For example, tumor overheating has been found to cause plaque formation over a period of 7 days following the hyperthermia after the local injection of MNPs [20]. In contrast, intravenous (i.v.) administration is far less invasive and could offer better coverage for the metastatic tumor regions.

The aim of this study was to develop novel MNPs of core/shell structures with mutual coupling of magnetically hard and soft components to simultaneously achieve high saturated magnetization and coercivity, which could be used as an anticancer theranostic agent for imaging and treatment. In addition, an efficient surface coating strategy was applied to the as-synthesized core/shell MNPs to

increase their biocompatibility, aqueous-dispersity and colloidal stability. Surface-coating materials typically include inorganic materials such as gold [21, 22] and silica [23, 24], and biodegradable polymers such as dextran [25, 26], chitosan [27-29], poly (lactide acid) [30, 31] and polyethylene glycol (PEG) [32, 33]. Amongst these surface modification methods, PEG coating is one of the most efficient approaches for preventing aggregation of MNPs in physiological conditions due to the steric expulsion between the hydrophilic chains, which extends the *in vivo* circulation and subsequently enhances the accumulation of MNPs in tumors due to its capability to resist reticuloendothelial system clearance [34-38].

The potential of our PEGylated core/shell FePt@Fe_3O_4 MNPs (PEG-MNPs) as a robust probe for cancer theranostics was investigated in a mouse model of 4T1.2 Neu breast tumor. The i.v. injected PEG- MNPs were activated by an alternating magnetic field to generate high magnetic heating. Combined with the deep-tissue penetration capacity of the magnetic field, the PEG-MNPs-mediated hyperthermia exhibited significant antitumor efficacy. In addition, the enhanced *in vivo* T_2-weighted spin-echo MRI sensitivity within the tumor region demonstrated the potential of using the PEG-MNPs for integrated diagnostics.

2. Materials and Methods

2.1 Materials

All chemicals were used as received without further purification unless otherwise noted. Platinum acetylacetonate ($Pt(acac)_2$) (97%), iron pentacarbonyl ($Fe(CO)_5$) (>99.99% trace metal basis), iron (III) acetylacetonate ($Fe(acac)_3$), 1,2-hexadecanediol (Technical grade 90%), dioctylether (99%), oleylamine (technical grade 70%), oleic acid (technical grade 90%), anhydrous hexane (95%), acetone (≥99.5%) and triethylamine (≥99.5%) were purchased from Sigma-Aldrich Co (St. Louis, MO, USA). Methanol (≥99.9%) and phenyl ether (99%) were obtained from Fisher Scientific (Pittsburgh, PA, USA). Ethanol (200 proof) was purchased from Decon Labs, Inc (King of Prussia, PA, USA). Double distilled water was used in syntheses, characterization, cell culture, and animal experiments (sterilized by autoclaving). Metastatic murine breast cancer cell line 4T1.2-Neu was a kind gift from Dr. Zhaoyang You, University of Pittsburgh (Pittsburgh, PA, USA). Cell culture medium, Dulbecco's Modified Eagle Medium (DMEM), and Fetal Bovine Serum (FBS) were purchased from Life Technologies (Grand Island, NY, USA).

2.2 Methods

2.2.1 FePt@Fe_3O_4 MNPs synthesis

The core/shell FePt@Fe_3O_4 MNPs synthetic procedure consists of two steps, including FePt core synthesis and Fe_3O_4 coating. Under an argon atmosphere, platinum acetylacetonate ($Pt(acac)_2$, 0.5 mmol) and 1,2-hexadecanediol (2 mmol) were dissolved in 20 mL of dioctylether, degased/refilled three cycles, and heated to 100°C. Iron pentacarbonyl ($Fe(CO)_5$, 1 mmol), oleylamine (0.17 mL) and oleic acid

(0.16 mL) were injected, degased/refilled one cycle under argon, and then the solution was heated to 295 ^{o}C for 30 min. After cooling to room temperature, the FePt MNPs were precipitated using methanol/hexane (5:1 v/v) and washed three times. The black FePt MNPs were collected and annealed at 450 ^{o}C for 2 h in a N_2/H_2 annealing atmosphere. The FePt MNPs were dispersed in hexane and stored under N_2. FePt MNPs (25mg) in hexane, iron (III) acetylacetonate ($Fe(acac)_3$, 1 mmol), oleylamine (1 mmol), oleic acid (1 mmol), and 1,2-hexadecanediol (5 mmol) were mixed in phenyl ether (20 mL) in a flask equipped with a condenser and degased/refilled with N_2 for three cycles. The mixture was heated to 100 ^{o}C and purged under N_2 for 10 min to remove the hexane. The remaining solution was heated to 265 ^{o}C for 30 min. After cooling to room temperature, the MNP were precipitated using methanol/hexane (5:1 v/v) and washed three times. The final black FePt@Fe_3O_4 MNPs were dispersed in hexane and stored in the N_2 glovebox.

2.2.2 Specific absorption rate (SAR) measurements of the FePt@Fe_3O_4 MNPs

A series of MNPs sample solutions with different MNP sizes were prepared, and their heating properties were measured using an inductive magnetic filed generator. Briefly, a 2 mL MNPs sample solution was placed in a glass vial and held within the induction heater coil using a Teflon holder. The Teflon holder acted as an insulator and prevented residual heating of the sample from the coil. The temperature change of the colloidal solution was measured using a fiber optic probe

(Neoptix Inc, Québec, QC, Canada) and the temperature rise of the sample solutions as a function of time was recoded with a computer. In order to reduce errors due to heat loss to the environment, the initial slope of the time dependent temperature curve ($\Delta T/\Delta t$) was taken for the calculation of SAR. The SAR value was calculated with the following equation, $SAR=(C/m_{NP})(\Delta T/\Delta t)$, where C is the heat capacity of the solution and m_{NP} is the mass of the nanoparticles.

2.2.3 Nuclear Magnetic Resonance (NMR) relaxivity measurement of MNPs solution

Longitudinal (T_1) and/or Transverse (T_2) relaxation rate constants were measured as a function of MNPs concentration using the inversion recovery and spin echo pulse sequences on a 400 MHz Bruker AV spectrometer [39].

2.2.4 Surface PEGylation of FePt@Fe_3O_4 MNPs

Core/shell FePt@Fe_3O_4 MNPs were modified with 2-methoxy polyethyleneoxy propyltrimethoxysilane (silane-PEG) through a ligand exchange reaction according to the method of Larsen *et. al.* [35, 40]. Briefly, 300 µL of as-synthesized nanoparticles in hexane (30 mg/mL) were washed with 10 mL of methanol/acetone (1:1) and centrifuged at 2,000×g for 30 min. After the supernatant was discarded, precipitated nanoparticles were re-suspended in 300 µL of hexane. The washing step was repeated three times and the precipitated nanoparticles were then dried under an argon flow to remove residual solvents.

The dried nanoparticles were dispersed in 6 mL of toluene, followed by addition of 600 μL of silane-PEG (1 mg/mL), 3 mL of triethylamine, and 60 μL of double distilled water. The mixture was stirred at 60° C overnight, after which the nanoparticles were precipitated with 25 mL of hexane/ethanol (3:1). The particle suspension was precipitated by centrifugation (2,000×g for 10 min) and re-suspended in 2 mL of toluene. The washing cycle was repeated three times. The washed PEGylated FePt@Fe_3O_4 MNPs (PEG-MNPs) were dried at 35 °C overnight with a centrifugal evaporator.

2.2.5 Fourier Transform Infrared Spectroscopy (FTIR)

FTIR spectra of approximately 2 mg of dried MNPs were recorded using an IRAffinity-1 FTIR (Shimadzu Scientific Instruments, KS, USA). For each spectrum, 45 scans were collected between 4000 and 400 cm^{-1} at a resolution of 1 cm^{-1}.

2.2.6 Hydrodynamic Diameters Measurements

PEG-MNPs were dispersed at 1 mg/mL in PBS, and Dynamic light scattering (DLS) measurements of the hydrodynamic diameters of PEG-MNP dispersions were performed at 25 °C using a ZetaPlus Particle Size Analyzer (Brookshaven Instrument, NY, USA), and all measurements were repeated five times.

2.2.7 Thermal Gravimetric Analysis (TGA)

TGA was performed on a Q50 TGA thermal analyzer (TA instruments, PA, USA). Approximately 8 mg of dried PEG-MNPs were heated from room temperature to 900 °C at 10 °/min.

2.2.8 Stability of the PEG-MNPs in physiological media

PEG-MNPs dispersed at 1 mg/mL in PBS, DMEM, and 10% FBS were stored at room temperature (r.t.) or 2-5 °C for up to one week. Stability of PEG-MNPs in the physiological media was assessed by observing aggregates and measuring hydrodynamic diameters by DLS. All measurements were repeated five times.

2.2.9 *In vitro* cytotoxicity

Metastatic murine breast cancer cell line 4T1.2-Neu was cultured in DMEM supplemented with 10% (v/v) FBS and 1% L-glutamine. Cells were trypsinized and seeded into 96-well plates at 3,000 cells/well (n=3 plates, 12 wells/concentration) and incubated overnight. PEG-MNPs dispersed in PBS were added to each well with final concentrations of 4 μg/mL to 4 mg/mL. PBS and 10% trichloroacetic acid (TCA) were used as negative and positive controls, respectively. A resazurin-based colorimetric assay was used to measure viability of cell cultures [41], and the IC_{50} was determined as the midpoint between control groups of positive and negative using GraphPad Prism 6 software (GraphPad Software Inc., La Jolla, CA).

2.2.10 Cellular uptake

To investigate the intracellular uptake of PEG-MNPs, 4T1.2-Neu cells were seeded in 12-well plates at 3×10^5 cells/well and then incubated with PEG-MNP suspensions in PBS at 0.3 mg/mL for 24 h. The same volume of the PBS without PEG-MNPs was added to cell cultures at the same cell density as a negative control. After three washes with PBS, the cells were detached with trypsin and then re-suspended in DMEM for cell counting using a hemocytometer. To measure the intracellular uptake of PEG-MNPs, the cell suspensions were centrifuged at 8,000×g for 10 min, and cell pellets were digested in 30% HCl at 70 °C for 1h [42]. PEG-MNPs in cells were quantified on an inductively coupled plasma mass spectrometer (ICP-MS) (7500a, Agilent Technologies, CA, USA) for iron content, and samples collected from untreated cells were used as a negative control. All measurements were repeated four times.

2.2.11 Tumoral uptake of PEG-MNPs

The animal study was approved by the Institutional Animal Care and Use Committee of the University of Kansas. To determine the dosage of PEG-MNPs used for the tumoral uptake, antitumor efficacy and MRI experiments, PEG-MNPs suspended in sterile saline were injected into tumor-free female Balb/c mice via the tail vein at three different dosages, 100, 50 and 20 mg/kg. Body weights of the mice were recorded every other day, and the animals were monitored for toxic reactions for ten days after the injection.

Female Balb/c mice were anesthetized with 2% isoflurane in O_2, and 3×10^6 4T1.2-Neu breast cancer cells in PBS were injected into the right mammary fat pad under the second nipple along the lateral line. Tumor sizes were measured three to four times weekly with a digital caliper in two perpendicular dimensions, and the tumor volume was calculated as: tumor volume = 0.52 × (width) ^{2} × (length). Once tumor volumes reached 150 mm^3, 100 mg/kg of PEG-MNPs suspended in sterile saline was injected intravenously via the tail vein. Animals were euthanized at 0.5, 4, 24, 48, 72 and 96 h post injection (n=3 per time point), and tumors were excised and blood samples were drawn into EDTA-treated vials through cardiac puncture followed by centrifugation for 5 minutes at 2,000×g to collect plasma. Biological samples were digested using aqua regia at 130 °C for 1 h and diluted with 1% HNO_3 prior to platinum analysis by ICP-MS.

2.2.12 Therapeutic efficacy

Female Balb/c mice bearing 4T1.2-Neu breast tumors were randomly divided into four groups (n=3 to 5 per group), including PEG-MNPs plus inductive field, inductive magnetic field only, PEG-MNPs only and untreated controls. When tumors reached 150 mm^3 in size, 100 mg/kg of PEG-MNPs dispersed in sterile saline was injected via the tail vein. After 24 h, the mice were placed under anesthesia in a water-cooled magnetic induction coil with the tumor region positioned in the central part of the coil. An inductive magnetic field of 400 kHz at 25.6 kAm^{-1} was applied for 5 min for two consecutive days using a SI-7KWHF induction heater

(Superior Induction Company, CA, USA) and a 2.5-cm copper coil. Following the inductive heating treatment, tumor growth was monitored until it reached an endpoint of 1,500 mm^3.

2.2.13 Magnetic Resonance Imaging (MRI)

In vivo MRI was performed using a 9.4-Tesla horizontal MR system (Agilent Technologies, Santa Clara, CA), in the Hoglund Brain Imaging Center at the University of Kansas Medical Center. Tumor bearing mice were injected intravenously with PEG-MNPs as stated in section 6. T_2-weighted MR images (echo times: 9.3, 14, 20, 30 and 40 ms) of mouse whole bodies were obtained at predetermined time points after injection. MR images acquired from animals without any injections were used as controls. MR images were processed using the Stimulate software [43]. A mono-exponential model of signal decay was applied to calculate T_2 values within the tumor region on a pixel-by-pixel basis.

2.3 Statistical analyses

Tumor size ratio for the four experimental groups were analyzed and expressed at mean ± standard deviation. Statistical significance was determined by the unpaired t-test with $P< 0.05$ using the GraphPad Prism 6 software.

3. Results and Discussion

3.1 Synthesis and characterization of core/shell FePt@Fe_3O_4 MNPs

Co-reduction of $Pt(acac)_2$ and $Fe(CO)_5$, followed by annealing at 450 °C for 2 hr formed the hard FePt core. Then the soft Fe_3O_4 shell was controllably hybridized via thermal decomposition from $Fe(acac)_3$ in the presence of oleylamine, oleic acid and 1,2-hexadecanediol in phenyl ether. Transmission electron microscopy (TEM) images of the core/shell FePt@Fe_3O_4 MNPs (Figure 1A) clearly revealed the spherical shape of the core/shell MNPs, and the detailed structure of the core/shell structure was characterized by the high-resolution TEM (HRTEM) in the inset that shows the coating of 5-nm Fe_3O_4 (lighter ring) on the initial 12-nm FePt core (darker region) to render a homogenous 22-nm core/shell structure. The highly uniform size distribution of the core/shell MNPs in Figure 1A confirmed that the MNPs formed is solely the core/shell FePt@Fe_3O_4 and not a mixture of FePt and Fe_3O_4 MNPs with much smaller sizes.

The exchange-coupled behavior of the FePt@Fe_3O_4 MNPs was compared with two different MNPs coupling schemes, including randomly mixed hard and soft MNPs and aggregated hard and soft MNPs. In comparison, the aggregated FePt and Fe_3O_4 MNPs were prepared by removing the oleic acid used to isolate and stabilize the MNPs during the synthesis. The M-H hysteresis measurement of the MNPs conducted with a superconducting quantum interference device (Figure 1B) shows that the coercivity values (Hc) for Fe_3O_4 and FePt MNPs are 50 Oe and 800 Oe at ambient temperature, respectively. Several research groups have investigated the

influence of annealing temperature on the microstructures and magnetic properties of the FePt MNPs [44-47]. It has been shown that higher annealing temperature could provide increased magnetic coercivities. For example, conversion of the soft face center cubic (fcc) phase FePt with a single SiO_2 [44] or a TaO_x [45] capping layer to the hard face center tetragonal (fct) phase have been found after annealing at 400 °C, and a highest coercivity (4.2 kOe)of FePt/TaO_x was reached as the annealing temperature increased to 550 °C [45]. However, further increases in annealing temperature above 580 - 600 °C could cause severe MNPs aggregation, increasing the particles size and size distribution [45, 47]. In this study, annealing was performed at 450 ° and a partial conversion from chemically disordered face-centered cubic (fcc) into the ordered face-centered tetragonal (fct) structure was achieved. The coercivity of our FePt MNPs is 800 Oe, which is consistent with the data reported by Kang et al [48]. Comparatively, the core/shell FePt@Fe_3O_4 MNPs have an Hc of 600 Oe with a single-phase-like loop due to the smooth magnetization transition, indicating the adjacent moments effectively aligning with each other due to the magnetic exchange coupling at the interface. In addition, a uniform size dispersion of the core/shell MNPs without any particle aggregation was illustrated in Figure 1A.

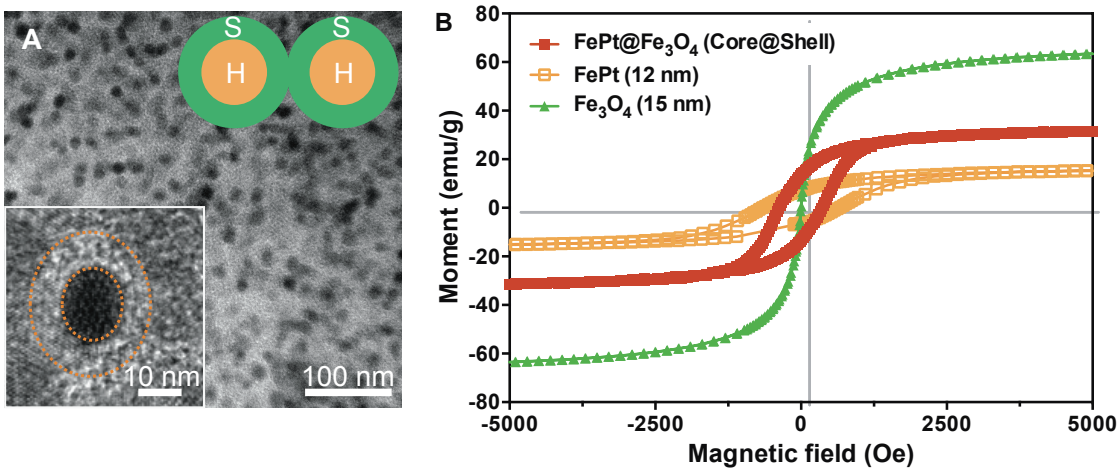

Figure 1. Nanostructures and magnetic characteristics of exchange coupled MNPs. (A) FePt@Fe_3O_4 (core/shell) MNPs; (B) The magnetic hysteresis loop of hard, soft and core/shell magnetic MNPs.

The effectiveness of hybrid FePt@Fe_3O_4 magnetically coupled nanoparticles as an MRI contrast agent was examined by measuring the dependence of the longitudinal ($1/T_1 = R_1$) and transverse ($1/T_2 = R_2$) relaxation rate constant of FePt@Fe_3O_4 MNPs solution. First, we measured R_1 and R_2 of the soft Fe_3O_4 MNPs, hard FePt MNPs, 1:1 mixture and core/shell FePt@Fe_3O_4 MNPs as a function of MNP concentration using the inversion recovery and spin echo pulse sequences, respectively, on a 9.4 T nuclear magnetic resonance (NMR) spectrometer [39] (Figure 2A and B). The relaxivities ($r_{1\ (or\ 2)}$) were determined from the slope of the plot of R_1 and R_2 versus MNP concentration. The values for r_1 equals 2.0, 0.2 and 1.2 Hz ml mg^{-1} for Fe_3O_4 MNPs, FePt MNPs and a 1:1 mixture MNPs, respectively, and the values for r_2 equals 20.1, 3.6 and 17.4 Hz ml mg^{-1} for Fe_3O_4 MNPs, FePt MNPs and the 1:1 mixture MNPs, respectively. For FePt@Fe_3O_4, r_1 equals 4.4 Hz ml mg^{-1} and r_2 equals 99.2 Hz ml mg^{-1}. The larger relaxivity of the FePt@Fe_3O_4 MNPs relative to Fe_3O_4 and FePt MNPs is hypothesized to stem from the favorable combination of coercively and saturation magnetization of the Fe_3O_4 shell and the FePt core structure. Comparing R_1 and R_2 of Fe_3O_4 MNPs, FePt MNPs, the 1:1 mixture of Fe_3O_4: FePt MNPs, a 1: 1 mixture prepared by ligand exchange and core/shell FePt@Fe_3O_4 MNPs at 1 mg/ml, the FePt@Fe_3O_4 MNPs have the largest effect upon the relaxation rate constant (Figure 2C and D), indicating their enhanced efficiency as contrast agents for either T_1-weighted or T_2-weighted MRI to promote spin-lattice relaxation. Therefore, the core/shell FePt@Fe_3O_4 MNPs were beneficial in both high oxidation resistance and maximum magnetic coupling to surrounding spins.

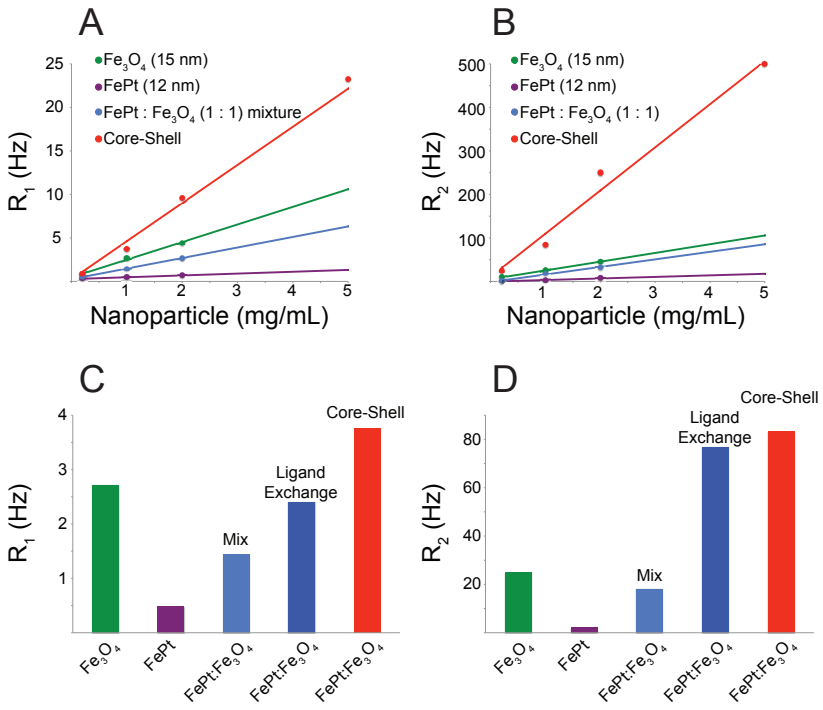

Figure 2. MNP relaxivity in hexane. (A) R_1 versus MNPs concentration. (B) R_2 versus MNPs concentration. Filled circles are data points for Fe_3O_4 (green), FePt (purple), 1:1 mixture of Fe_3O_4 and FePt (blue) and Core/shell (red). Lines are linear fits of data to determine relaxivity. (C) R_1 and (D) R_2 at 1 mg/ml for Fe_3O_4 (green), FePt (purple), 1:1 mixture of Fe_3O_4:FePt (blue), 1:1 mixture of Fe_3O_4:FePt with ligands exchanged by the addition of hexanoic acid (dark blue) and Core/shell (red).

During a local hyperthermia treatment, the MNPs dispersed in the biological fluids or tumor tissues are subjected to a magnetic alternating current field and then induce a gradual alignment of the magnetic moments towards the external field. When the magnetic moments of MNPs relax to their equilibrium orientation states, the magnetic energy is dissipated and converted into heating effects that are related to the maximum power loss during the magnetization reversal process. Specific absorption rate (SAR) is a key parameter to describe the energy amount converted into thermal energy material per gram [49]. In order to achieve efficient magnetic hyperthermia, the MNPs should heat rapidly within a short period of treatment time. Therefore, a maximized SAR is required as MNPs possessing the high SAR value enable a smaller injection dose due to their excellent heat-generation capability, thus reducing the toxic effects.

The SAR values of core–shell nanoparticles were compared with single-component magnetic MNPs, randomly mixed MNPs and aggregated MNPs (Figure 3A). While the SARs of single-component MNPs range from 20 (FePt MNPs) to 300 Wg^{1} (Fe_3O_4 MNPs), the SAR of core–shell MNPs was of 550 Wg^{-1}. The significantly increased SAR value results from the mutual coupling between the magnetically hard (FePt) and soft (Fe_3O_4) materials, which enhances the efficiency of magnetic thermal induction and reduces the required dose of MNPs for hyperthermia. The heating effect depends on the particle geometry as well as the anisotropy. The SAR of core–shell nanoparticles can be precisely tuned by varying the combination of the differently sized core and shell components.

Using an adopted theoretical model, we then calculated SAR values as a function of particle size at varying polydispersity indices (σ). During the calculation, the values of the magnetic anisotropy constant and the saturation magnetization of FePt MNPs (M_d=1140 kA/m, K=206 kJ/m^3) and Fe_3O_4 MNPs (M_d=446 kA/m, K=9 kJ/m^3) were taken from the published data [50]. The K values have been reported to vary from 206 to 7000 kJ/m^3 for FePt MNPs with the fcc structure and fct structure after annealing at 500 °C for 5 h [51]. As our FePt MNPs were annealed at a lower temperature and a shorter time, the un-annealed value was used in the theoretical calculation. The calculated SAR of both MNP types increased with particle sizes up to a maximum of 183 W/g for 16.2-nm FePt MNPs and 132 W/g for 18.3-nm Fe_3O_4 MNPs. Single-domain superparamagnetic nanoparticles primarily generate heat in an alternating field by a relaxation losses mechanism, which is collectively ruled by two distinct modes, Néel relaxation and Brownian relaxation [19, 52]. Néel relaxation refers to an internal magnetic moment vector rotation along the crystal easy axis, and the power loss corresponding to this process is exponentially proportional to the magnetic anisotropy constant and the MNPs volume. In the Brownian mode, however, MNPs undergo oscillation as a whole towards the external field, and the corresponding power loss correlates linearly with the hydrodynamic volume of the MNPs. Due to the exponential correlation between the relaxation time versus the product of the magnetic anisotropy constant and the particle size in the Néel mode, the Néel relaxation typically dominates the effective relaxation process for the MNPs with smaller size[19]. In our study, the optimal size is 16.2 nm for FePt MNPs and18.3 nm for Fe_3O_4 MNPs (Figure 3B). Beyond this

point, the dominant relaxation process changed to the Brownian relaxation, which is independent of the magnetic anisotropy and only relies on the particle size. Size distribution of the MNPs also appeared to play a critical role to achieve high SAR. As shown in Figure 2B, when the polydispersity index (σ) increased from zero to 40%, the SAR values decreased accordingly by 32.74 % for FePt MNPs and 62.17% for Fe_3O_4 MNPs. We have also observed that the measured SAR value of FePt MNPs is much lower than the calculated value using the theoretical model, probably due to the achieved partial fct sturcture using the relatively lower annealing temperatures during the synthesis.

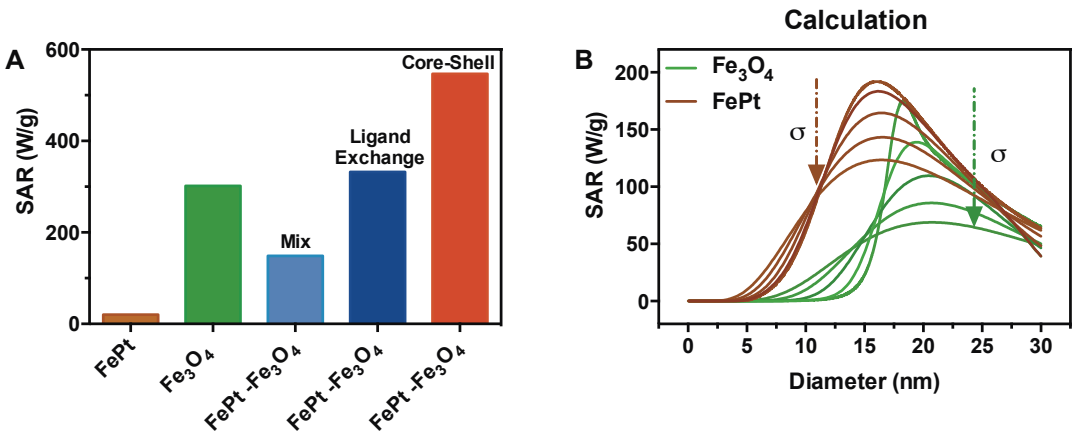

Figure 3. Hyperthermia characteristics of exchange coupled MNPs; (A) Magnetic field dependence of Specific Absorption Rate (SAR) for FePt hard MNPs, Fe_3O_4 soft magnetic MNPs, 1:1 mixed FePt and Fe_3O_4 MNPs before ligand exchange, 1:1 mixed FePt and Fe_3O_4 MNPs after ligand exchange and core/shell FePt@Fe_3O_4 MNPs; (B) Calculated FePt and Fe_3O_4 MNP diameter dependence of SAR (field amplitude: 5000 Am^{-1}; frequency: 366 kHz). The σ corresponds to the particle distribution parameter in the lognormal distribution used in the calculation to simulate the effect of polydispersity of the sample. The arrows in the Figure 2(B) indicate that σ values increase from 0% to 40% in a 10%-increment.

3.2 Surface PEGylation and characterization of core/shell FePt@Fe_3O_4 MNPs

Colloidal stability and biocompatibility are two essential requirements for clinical application of exchange-coupled magnetic nanoparticles. The core/shell FePt@Fe_3O_4 MNPs synthesized in organic solvent and coated with oleic acid are not easily dispersed in water. These as-made MNPs are hydrophobic and they are subject to rapid elimination from the blood circulation before reaching tumor sites by macrophages of the mononuclear phagocyte system. Modification of the core/shell FePt@Fe_3O_4 MNPs was achieved by exchanging oleic acid with hydrophilic PEG molecules using silane-PEG, and the success of PEGylation was confirmed by FTIR. The three FTIR peaks resolved between 840 and 1040 cm^{-1} in the purified PEG-MNPs dry power (Figure 4) were assigned to the Si-O-Fe stretching. The peaks at 1100 cm^{-1} and 1360 cm^{-1} corresponded to the ether group C-O-C stretch band and the vibration band, respectively. Detection of these characteristic peaks confirmed the presence of a silane-PEG coating on the surface of magnetic nanoparticles.

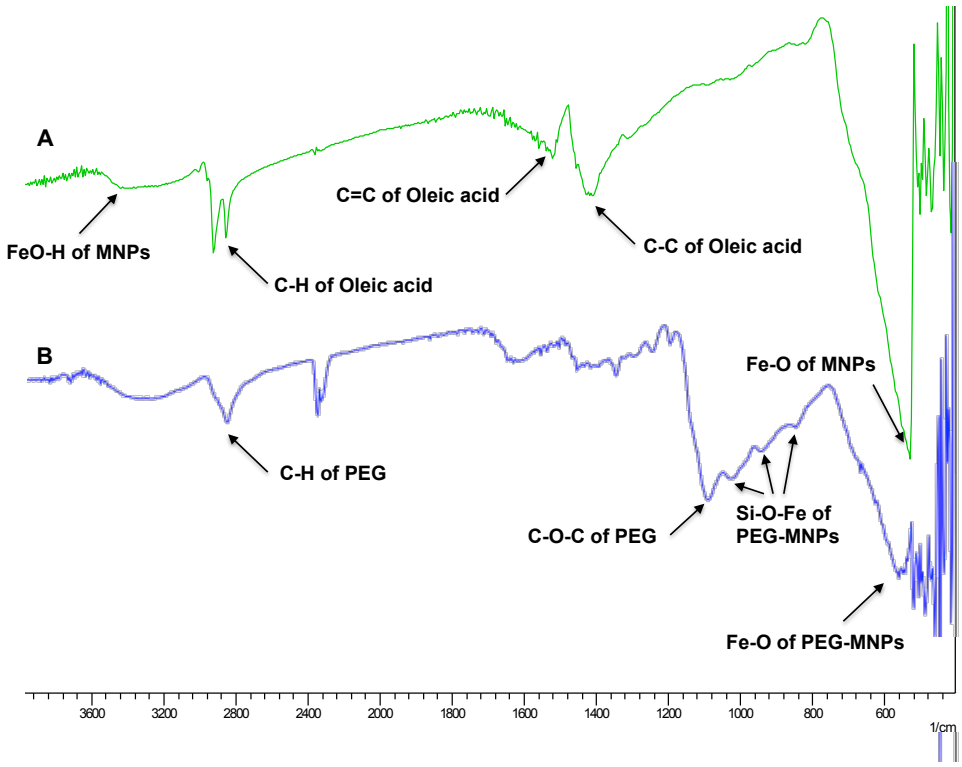

Figure 4. FTIR of (A) as-made $FePt@Fe_3O_4$ MNPs, (B) PEGylated $FePt@Fe_3O_4$ MNPs.

The weight percentage of silane-PEG was estimated to be 21.34% using thermal gravimetric analysis (TGA) (Figure 5), based on a 21.34% mass loss from 17.28 to 455.01 °C. In addition, the longitudinal relaxivity value for PEG-MNPs was determined to be 0.2084 mL $(s^{-1})(mg^{-1})$ with a good linear correlation (R^2 = 0.99629) (Figure 6).

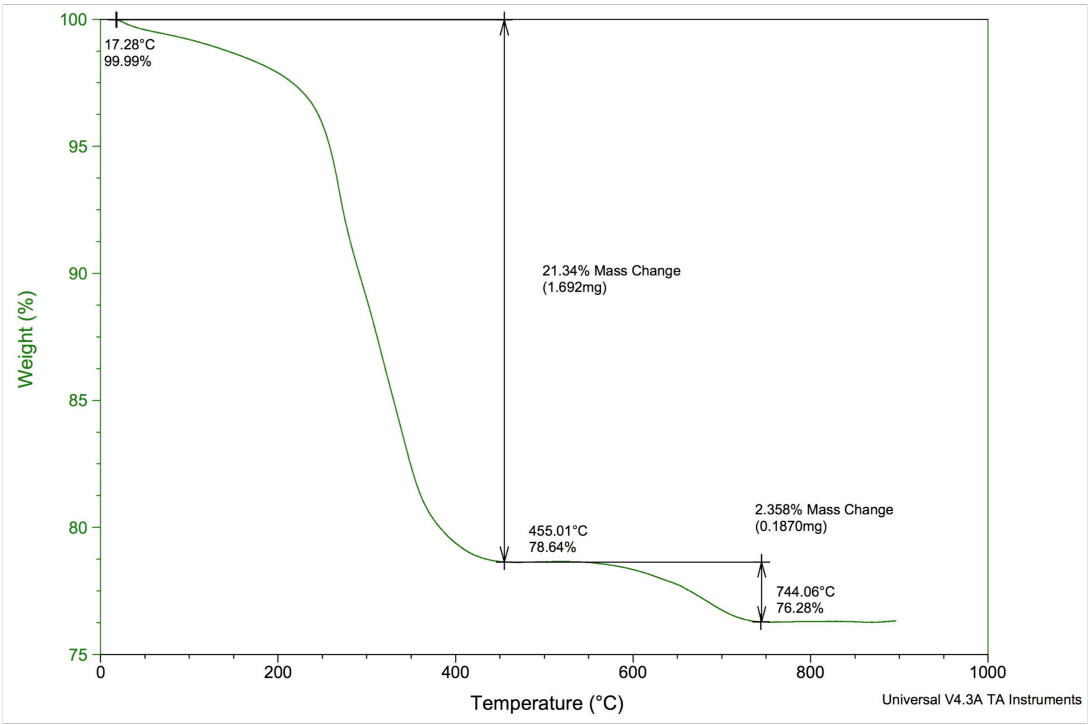

Figure 5. Thermogravimetric analysis of the PEG-MNPs

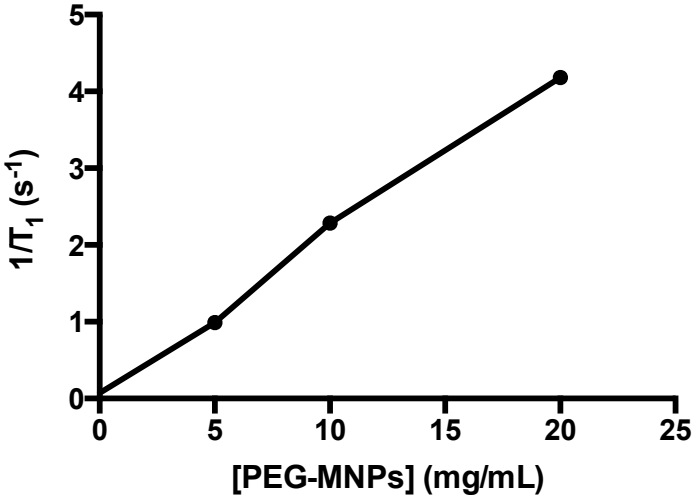

Figure 6. $1/T_1$ values measured by NMR as a function of the PEG-MNPs concentrations

PEGylated FePt@Fe_3O_4 MNPs were well dispersed in aqueous solutions with a hydrodynamic diameter of 25.9 ± 2.8 nm and a narrow colloid size distribution (Figure 7).

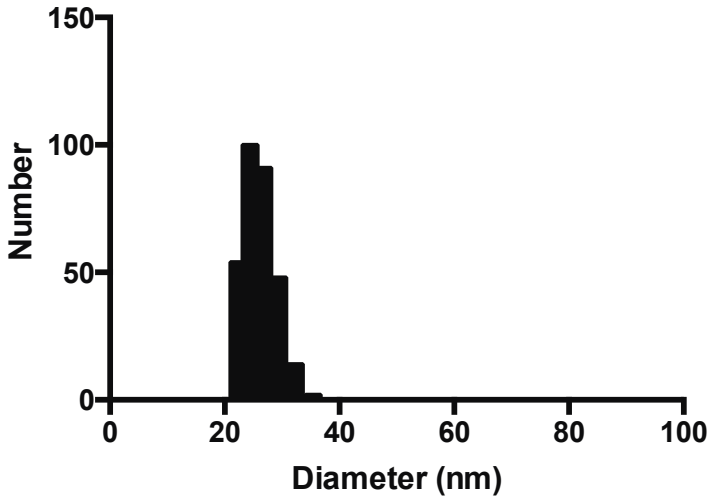

Figure 7. DLS of the freshly prepared PEG-MNPs in PBS at 25^{o} C (size distribution in number). Hydrodynamic diameter= 25.9 ± 2.8 nm.

The stability of monodisperse PEG-MNPs was investigated in PBS, DMEM with 10% (v/v) FBS and PBS with 10% (v/v) FBS, at both room temperature and refrigerated temperature for a week. Although hydrodynamic diameters of all six of the PEG-MNPs dispersions increased (Table1), from 9.26 % in PBS at 4 °C to 29.7% in DMEM at room temperature, no agglomeration was observed during this period of time (Figure 8), indicating high colloidal stability due to the steric repulsion between the PEG chains.

Table 1. DLS measurements of PEG-MNP dispersion stored in physiological media for one week (Size of freshly prepared PEG-MNPs: 25.9 ± 2.8 nm).

	2-5 °C, nm	**r.t., nm**
PBS	28.3 ± 3.2	31.2 ± 3.3
DMEM	30.3 ± 3.0	33.6 ± 3.2
10% FBS	29.9 ± 3.3	31.3 ± 3.2

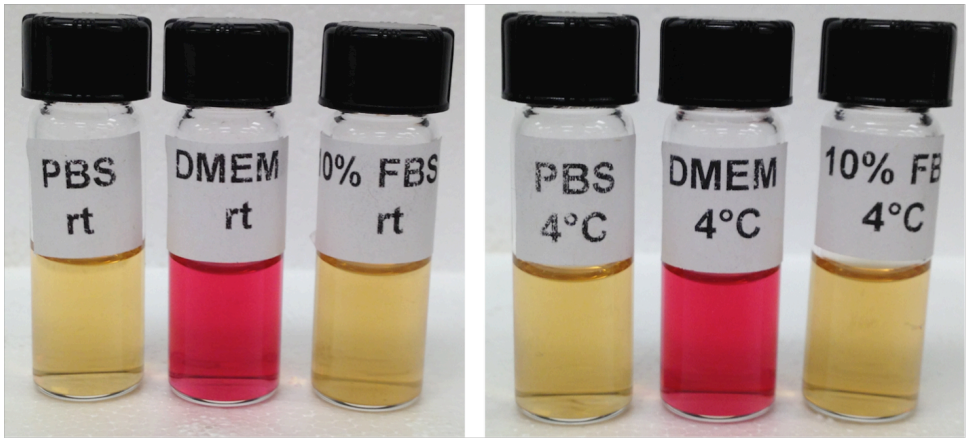

Figure 8. PEG-MNP dispersion (1 mg/mL) in PBS, DMEM, and 10% FBS stored for one week at room temperature (left) and 4 ^{o}C (right)

3.3 Intracellular uptake and *in vitro* cytotoxicity of PEG-MNPs

The PEG-MNPs had low toxicity and high uptake in cells. The IC_{50} of silane-PEG-coated was determined as 0.487 ± 0.073 mg/mL in murine breast cancer 4T1.2 Neu cells, and the cells were approximately 85% to 100% viable at the concentrations of 4 μg/mL to 100 μg/mL after incubation for 72 h (Figure 9A). The ICP-MS iron analysis of digested cell pellets after a 24-h PEG-MNPs treatment demonstrated significant intracellular uptake of PEG-MNPs with 0.95 ± 0.21 pg/cell (Figure 9B), which is probably due to the enhanced nanoparticles internalization of the particles provided by the PEG chain [53].

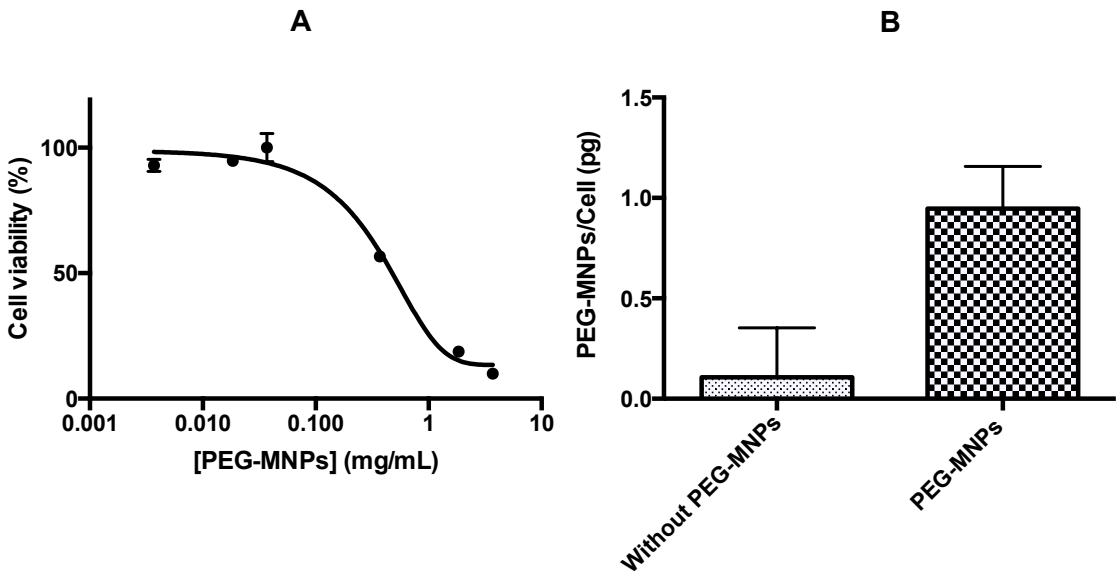

Figure 9. (A) Effect of the PEG-MNPs on the proliferation of murine breast cancer 4T1.2-Neu cells. After 72-h incubation, the relative number of the viable cells was determined by a resazurin assay. IC_{50}=0.487 ± 0.073 mg/mL; (B) Intracellular uptake of the PEG-MNPs by 4T1.2-Neu cells after 24-h incubation at the IC_{50} concentration. (Iron analysis by ICP-MS: detection limits=3.79 ppb; R^2=0.9982)

3.4 Tumor accumulation of PEG-MNPs

Healthy Balb/c mice were dose escalated by i.v. administration of PEG-MNPs and monitored for toxic reactions for up to ten days. All of the mice remained in good condition, with body scores above 2.5 and body weight losses less than 20% (Figure 10). No toxic reactions including lethargy, paralysis, orrespiratory depression were observed during the study. Therefore, a dosage of 100 mg/kg was chosen for subsequent animal experiments.

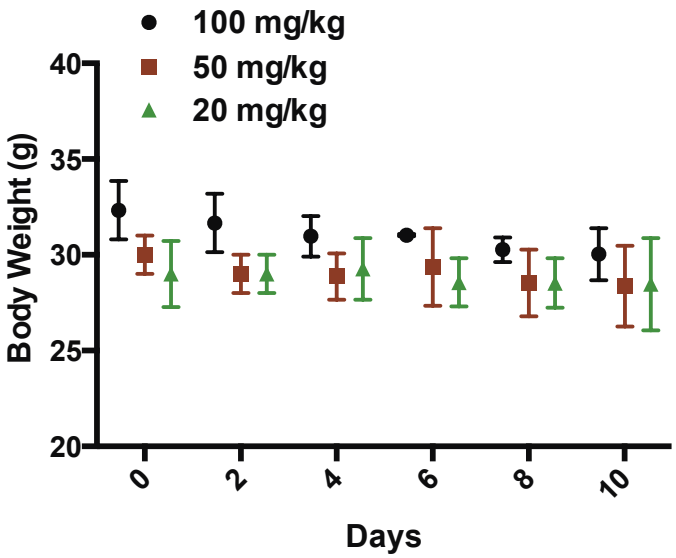

Figure 10. Balb/c mice were intravenously injected with 100, 50 and 20 mg/kg of PEG-MNPs via the tail vein.

It has been reported that nano-sized bare SPIONs are susceptible to opsonization by plasma proteins, followed by rapid clearance from systemic circulation by macrophages of the reticuloendothelial system[54] . For example, the plasma half-life of SPIONs sized at 40 nm was less than 10 min after intravenous injection, and approximately 90% of the injected particles accumulated in mononuclear phagocyte system organs including the liver, spleen and bone marrow [55]. Therefore, the amount of MNPs that reached the target tissues was substantially reduced, limiting their biomedical applications. In this study, the surface of as-synthesized core/shell MNPs was grafted with hydrophilic and steric PEG chains to minimize their clearance by macrophages [40] and thus prolong their retention time. Figure 11 shows that PEG-MNPs exhibited a half-life of 1.35 h (Figure 11A) after intravenous injection into tumor-bearing Balb/c mice. Pharmacokinetic analysis of PEG-MNPs was performed by fitting data (0 to 24 h) to a two-compartment model (Table 2). The plasma PEG-MNPs concentration decreased by 98.24 ± 0.33 % in the first 4 h as PEG-MNPs distributed from the central compartment to peripheral compartments, followed by slow clearance in the beta phase. Long-circulating PEG-MNPs gradually accumulated in the leaky vasculature of the breast tumor region from 4 h to 96 h (Figure 11B, Table 3) due the enhanced permeability and retention effect, achieving enhanced tumor delivery.

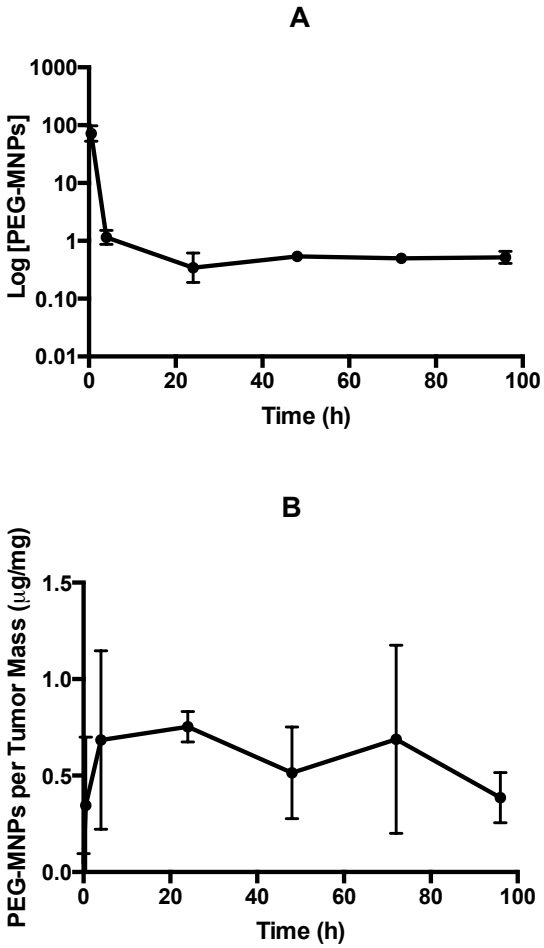

Figure 11. After intravenous administration, PEG-MNPs were (A) cleared from the systemic circulation, and (B) accumulated in the 4T1.2-Neu breast tumors. N=3 per time point. (Platinum analysis by ICP-MS: detection limits=10.01 ppt; r^2=0.9998)

Table 2. Pharmacokinetics of 2.5-mg i.v. PEG-MNPs in Balb/c mice with 4T1.2-Neu breast tumors (average ± SD; N=3)

Parameters (unit)	**PEG-MNPs i.v.**
V_d (mL)	0.768 ± 0.489
C_p^0 (mg mL^{-1})	131.609 ± 51.074
$AUC_{0\text{-}24\ h}$ (mg h mL^{-1})	154.467 ± 31.428
Cl (ml h^{-1})	0.017 ± 0.003
k (h^{-1}) (β)	0.033 ± 0.026

Table 3. Tumor tissue AUC (average ± SD) and C_{max} (average ± SD; N=3) of 2.5-mg i.v. PEG-MNPs.

Parameters (unit)	**PEG-MNPs i.v.**
$AUC_{0\text{-}96\ h}$ (mg h mL^{-1})	58.870 ± 12.953
C_{max} (µg mg^{-1})	0.932 ± 0.279

3.5 PEG-MNPs-mediated hyperthermia and MR imaging

Hyperthermia may cause the shrinkage or sometimes a complete eradication of tumors by killing cancer cells and damaging proteins within the cancer cells [20]. The effectiveness of hyperthermia treatment mainly depends on the degree of temperature increase during a defined length of treatment. The excellent thermal energy transfer capability of the PEG-MNPs was demonstrated in a phantom test using PEG-MNPs in saline solution (25 mg/mL). After applying an inductive magnetic field for 5 min, the temperature of the PEG-MNP solution increased from 22.5 °C to 64.5 °C. For the animals that received PEG-MNPs plus inductive magnetic field, the tumor size increased 2.32 fold two weeks after the treatment (Figure 12). In comparison, for the animals in the saline group, PEG-MNPs only group, and inductive magnetic field only group, the tumor size increased 8.66, 12.96 and 8.05 fold, respectively in the same time period. PEG-MNPs-mediated hyperthermia demonstrated a significantly enhanced inhibition of the tumor progression, which is likely due to the fact that PEG-MNPs in the tumor region induced efficient magnetic-heat energy transfer to albate the cancer cells, achieving improved local tumor control.

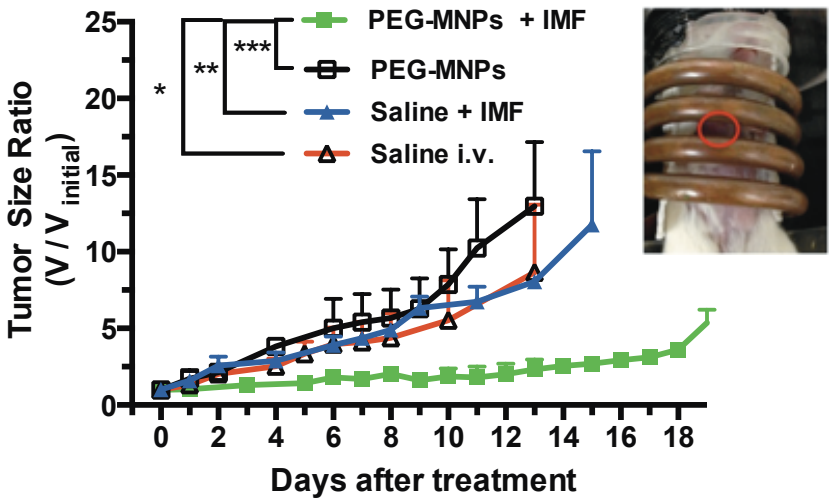

Figure 12. Tumor Volume ($V/V_{initial}$) after treatment, $3 \leq N \leq 5$. PEG-MNPs were injected intravenously once tumors reached approximately 150 mm^3, and an inductive magnetic field of 400 kHz at 25.6 kAm^{-1} was applied for 5 min in the following two days. Tumor inhibition was observed in the mice treated with PEG-MNPs hyperthermia. (* $p<0.05$, ** $p<0.01$, and *** $p<0.001$). Inset shows a mouse with a 150 mm^3-sized breast tumor (red circle) in a water-cooled coil receiving hyperthermia treatment.

The potential application of PEG-MNPs as an MRI contrast agent for cancer diagnosis was evaluated by T_2 –weighted MRI on Balb/c mice implanted with 4T1.2-Neu breast tumors. Mice injected with the i.v. PEG-MNPs were randomly divided into three groups: MRI at 24 h post-injection (n=3), 48 h post-injection (n=2), and 48 h post-injection with hyperthermia at 24 h post-injection (n=3). T_2-weighted MR images of animals in all three of the PEG-MNP injected groups showed significant signal reduction within the tumor region when compared to the untreated animals (Figure 13). Region of interest analysis showed T_2 values in the tumor were remarkably lower (Table 4) in animals with PEG-MNPs injection compared with controls.

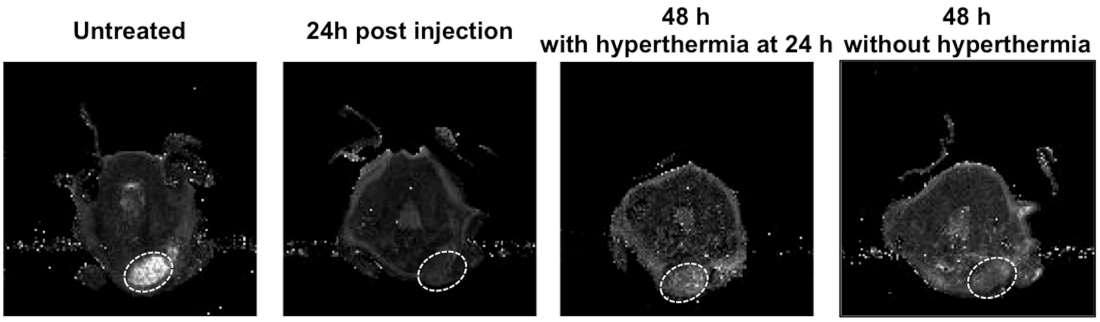

Figure 13. Representative axial T_2-weighted spin-echo MR images of Balb/c mice with 4T1.2-Neu breast tumors (circled) without PEG-MNPs injection, and at 24 and 48 h after PEG-MNPs injection (i.v.). Significant signal decrease was observed in the tumor region at 24 h and 48 h post-injection.

Table 4. T_2 values of the breast tumor regions.

Group	**Average T_2 (ms)**	**Standard Deviation (ms)**
Untreated	37.07	13.97
24 h post-injection	20.77	0.34
48 h post-injection	26.65	1.28
48 h post-injection with hyperthermia	31.21	2.61

4. Conclusions

In conclusion, we developed formulations of biocompatible core/shell exchanged-coupled magnetic nanoparticles as a novel theranostics agent through surface-PEGylation. PEG-MNPs-induced hyperthermia in a breast orthotopic tumor model in immune-competent animals demonstrated the enhanced anti-tumor effectiveness due to the high magnetic-thermal energy transfer capability of PEG-MNPs. In addition, augmented MRI contrast in the tumor region suggested application potential of PEG-MNPs for cancer diagnosis. Our further studies will focus on developing targeted core/shell PEG-MNPs to expand the scope of their bio-application in theranostics.

5. References

1. Wang, Y.X., S.M. Hussain, and G.P. Krestin, *Superparamagnetic iron oxide contrast agents: physicochemical characteristics and applications in MR imaging.* Eur Radiol, 2001. **11**(11): p. 2319-31.
2. Wu, W., Q. He, and C. Jiang, *Magnetic iron oxide nanoparticles: synthesis and surface functionalization strategies.* Nanoscale Res Lett, 2008. **3**(11): p. 397-415.
3. Singh, A. and S.K. Sahoo, *Magnetic nanoparticles: a novel platform for cancer theranostics.* Drug Discov Today, 2013. **19**(4): p. 474-81.
4. Shubayev, V.I., T.R. Pisanic, 2nd, and S. Jin, *Magnetic nanoparticles for theragnostics.* Adv Drug Deliv Rev, 2009. **61**(6): p. 467-77.

5. Hayashi, K., et al., *Superparamagnetic nanoparticle clusters for cancer theranostics combining magnetic resonance imaging and hyperthermia treatment.* Theranostics, 2013. **3**(6): p. 366-76.

6. Laurent, S., et al., *Magnetic fluid hyperthermia: focus on superparamagnetic iron oxide nanoparticles.* Adv Colloid Interface Sci, 2011. **166**(1-2): p. 8-23.

7. Gupta, A.K., et al., *Recent advances on surface engineering of magnetic iron oxide nanoparticles and their biomedical applications.* Nanomedicine, 2007. **2**(1): p. 23-39.

8. McCarthy, J.R., et al., *Targeted delivery of multifunctional magnetic nanoparticles.* Nanomedicine, 2007. **2**(2): p. 153-67.

9. Mikhaylova, M., et al., *Superparamagnetism of magnetite nanoparticles: dependence on surface modification.* Langmuir, 2004. **20**(6): p. 2472-7.

10. Pollert, E., et al., *Search of new core materials for magnetic fluid hyperthermia: Preliminary chemical and physical issues.* Prog Solid State Chem, 2009. **37**(1): p. 1-14.

11. Chou, S.W., et al., *In vitro and in vivo studies of FePt nanoparticles for dual modal CT/MRI molecular imaging.* J Am Chem Soc, 2010. **132**(38): p. 13270-8.

12. Kim, J., et al., *Dispersible Ferromagnetic FePt Nanoparticles.* Adv Mater, 2009. **21**(8): p. 906-909.

13. Lee, S.J., et al., *Synthesis of highly magnetic graphite-encapsulated FeCo nanoparticles using a hydrothermal process.* Nanotechnology, 2011. **22**(37): p. 375603.

14. Ennas, G., et al., *Influence of Metal Content on Size, Dispersion, and Magnetic Properties of Iron–Cobalt Alloy Nanoparticles Embedded in Silica Matrix.* Chem Mater, 2004. **16**(26): p. 5659-5663.

15. Mori, K., Y. Kondo, and H. Yamashita, *Synthesis and characterization of FePd magnetic nanoparticles modified with chiral BINAP ligand as a recoverable catalyst vehicle for the asymmetric coupling reaction.* Phys Chem Chem Phys, 2009. **11**(39): p. 8949-54.

16. Ho, D., X. Sun, and S. Sun, *Monodisperse Magnetic Nanoparticles for Theranostic Applications.* Acc Chem Res, 2011. **44**(10): p. 875-882.

17. Zeng, H., et al., *Bimagnetic Core/Shell FePt/Fe3O4 Nanoparticles.* Nano Letters, 2003. **4**(1): p. 187-190.

18. Zeng, H., et al., *Tailoring magnetic properties of core/shell nanoparticles.* Appl Phys Lett, 2004. **85**(5): p. 792-794.

19. Rosensweig, R.E., *Heating magnetic fluid with alternating magnetic field.* J Magn Magn Mater, 2002. **252**(0): p. 370-374.

20. Lee, J.H., et al., *Exchange-coupled magnetic nanoparticles for efficient heat induction.* Nat Nanotechnol, 2011. **6**(7): p. 418-22.

21. Daniel, M.-C. and D. Astruc, *Gold Nanoparticles: Assembly, Supramolecular Chemistry, Quantum-Size-Related Properties, and Applications toward Biology, Catalysis, and Nanotechnology.* Chem Rev, 2003. **104**(1): p. 293-346.

22. Chen, M., et al., *Gold-coated iron nanoparticles for biomedical applications.* J Appl Phys, 2003. **93**(10): p. 7551-7553.

23. Santra, S., et al., *Synthesis and Characterization of Silica-Coated Iron Oxide Nanoparticles in Microemulsion: The Effect of Nonionic Surfactants.* Langmuir, 2001. **17**(10): p. 2900-2906.

24. Tartaj, P., T. González-Carreño, and C.J. Serna, *Single-Step Nanoengineering of Silica Coated Maghemite Hollow Spheres with Tunable Magnetic Properties.* Adv Mater, 2001. **13**(21): p. 1620-1624.

25. Berry, C.C., et al., *Dextran and albumin derivatised iron oxide nanoparticles: influence on fibroblasts in vitro.* Biomaterials, 2003. **24**(25): p. 4551-7.

26. Carmen Bautista, M., et al., *Surface characterisation of dextran-coated iron oxide nanoparticles prepared by laser pyrolysis and coprecipitation.* J Magn Magn Mater, 2005. **293**(1): p. 20-27.

27. Hee Kim, E., et al., *Synthesis of ferrofluid with magnetic nanoparticles by sonochemical method for MRI contrast agent.* J Magn Magn Mater, 2005. **289**(0): p. 328-330.

28. Li, G.-Y., et al., *Kinetics of adsorption of Saccharomyces cerevisiae mandelated dehydrogenase on magnetic Fe3O4–chitosan nanoparticles.* Colloids Surf, A, 2008. **320**(1–3): p. 11-18.

29. Li, G.-y., et al., *Preparation and characterization of carboxyl functionalization of chitosan derivative magnetic nanoparticles.* Biochem Eng J, 2008. **40**(3): p. 408-414.

30. Chen, F., et al., *Synthesis of magnetite core–shell nanoparticles by surface-initiated ring-opening polymerization of l-lactide.* J Magn Magn Mater, 2008. **320**(13): p. 1921-1927.

31. Gómez-Lopera, S.A., et al., *Colloidal Stability of Magnetite/Poly(lactic acid) Core/Shell Nanoparticles.* Langmuir, 2006. **22**(6): p. 2816-2821.

32. Gupta, A.K. and A.S. Curtis, *Surface modified superparamagnetic nanoparticles for drug delivery: interaction studies with human fibroblasts in culture.* J Mater Sci Mater Med, 2004. **15**(4): p. 493-6.

33. Liu, Z., et al., *PEGylated nanographene oxide for delivery of water-insoluble cancer drugs.* J Am Chem Soc, 2008. **130**(33): p. 10876-7.

34. Liu, D., et al., *Effective PEGylation of Iron Oxide Nanoparticles for High Performance In Vivo Cancer Imaging.* Adv Funct Mater, 2011. **21**(8): p. 1498-1504.

35. Larsen, E.K.U., et al., *Size-Dependent Accumulation of PEGylated Silane-Coated Magnetic Iron Oxide Nanoparticles in Murine Tumors.* ACS Nano, 2009. **3**(7): p. 1947-1951.

36. Larsen, E.K., et al., *Accumulation of magnetic iron oxide nanoparticles coated with variably sized polyethylene glycol in murine tumors.* Nanoscale, 2012. **4**(7): p. 2352-61.

37. Cole, A.J., et al., *Polyethylene glycol modified, cross-linked starch-coated iron oxide nanoparticles for enhanced magnetic tumor targeting.* Biomaterials, 2011. **32**(8): p. 2183-93.

38. Cole, A.J., et al., *Magnetic brain tumor targeting and biodistribution of long-circulating PEG-modified, cross-linked starch-coated iron oxide nanoparticles.* Biomaterials, 2011. **32**(26): p. 6291-301.

39. Mills, N., *150 and More Basic NMR Experiments: A Practical Course, 2nd Edition (Braun, S.; Kalinowski, H.-O.; Berger, S.).* J Chem Educ, 2000. **77**(7): p. 831.

40. Zhang, Y., N. Kohler, and M. Zhang, *Surface modification of superparamagnetic magnetite nanoparticles and their intracellular uptake.* Biomaterials, 2002. **23**(7): p. 1553 - 1561.

41. Cohen, M.S., et al., *A novel intralymphatic nanocarrier delivery system for cisplatin therapy in breast cancer with improved tumor efficacy and lower systemic toxicity in vivo.* Am J Surg, 2009. **198**(6): p. 781-6.

42. Sun, C., R. Sze, and M. Zhang, *Folic acid-PEG conjugated superparamagnetic nanoparticles for targeted cellular uptake and detection by MRI.* J Biomed Mater Res, Part A, 2006. **78A**(3): p. 550--557.

43. Strupp, J., *Stimulate: a GUI based fMRI analysis software package.* Neuroimage, 1996. **3**(3): p. S607.

44. Wei, D.H. and Y.D. Yao, *Magnetization Reversal Mechanism and Microstructure Refinement of the FePt (001) Nanogranular Films With SiO2 Capping Layer.* IEEE Trans Magn, 2009. **45**(10): p. 4092-4095.

45. Lin, Z., et al., *Effects of annealing temperature on the microstructure, optical, ferroelectric and photovoltaic properties of BiFeO3 thin films prepared by sol–gel method.* Ceram Int, 2013. **39**(8): p. 8729-8736.

46. Mei Hyie, K. and I.I. Yaacob, *Annealing Behavior of FePt Ferromagnetic Nanoparticles Prepared in Water‐in‐Oil Microemulsions.* AIP Conf Proc, 2009. **1138**(1): p. 117-128.

47. Nguyen, H.L., et al., *Synthesis of Size-Controlled fcc and fct FePt Nanoparticles.* Chem Mater, 2006. **18**(26): p. 6414-6424.

48. Kang, S., et al., *Synthesis, self-assembly, and magnetic properties of [FePt]_{1-x}Au_x nanoparticles.* IEEE Trans Magn, 2003. **39**(5): p. 2753-2757.

49. Habib, A.H., et al., *Evaluation of iron-cobalt/ferrite core-shell nanoparticles for cancer thermotherapy.* J Appl Phys, 2008. **103**(7).

50. Maenosono, S. and S. Saita, *Theoretical assessment of FePt nanoparticles as heating elements for magnetic hyperthermia.* IEEE Trans Magn, 2006. **42**(6): p. 1638-1642.

51. Inomata, K., T. Sawa, and S. Hashimoto, *Effect of large boron additions to magnetically hard Fe‐Pt alloys.* J Appl Phys, 1988. **64**(5): p. 2537-2540.

52. Ma, M., et al., *Size dependence of specific power absorption of Fe3O4 particles in AC magnetic field.* J Magn Magn Mater, 2004. **268**(1–2): p. 33-39.

53. Yamazaki, M. and T. Ito, *Deformation and instability in membrane structure of phospholipid vesicles caused by osmophobic association: mechanical stress model for the mechanism of poly(ethylene glycol)-induced membrane fusion.* Biochemistry, 1990. **29**(5): p. 1309-14.

54. Moghimi, S.M., A.C. Hunter, and J.C. Murray, *Long-circulating and target-specific nanoparticles: theory to practice.* Pharmacol Rev, 2001. **53**(2): p. 283-318.

55. Duguet, E., et al., *Magnetic nanoparticles and their applications in medicine.* Nanomedicine, 2006. **1**(2): p. 157-68.

Chapter 4

Cabozantinib Loaded DSPE-PEG_{2000} Micelles as Delivery System: Formulation, Characterization and Cytotoxicity Evaluation

1. Introduction

Receptor tyrosine kinases (RTKs) are a family of transmembrane cell surface receptors for diverse cell-signaling molecules such as cytokines, growth factors, and hormones. Functionally, RTKs regulate many critical cellular processes, including cell growth, differentiation and angiogenesis. Dysregulation of RTK activity is associated with several tumorigenic pathways, including the stimulation of malignant transformation, angiogenesis and tumor growth. RTK overexpression has been observed in a wide variety of highly invasive human tumors, including head and neck squamous cell carcinomas [1], medullary thyroid cancer (MTC) [2-5], glioblastoma multiforme (GBM) [6-8] and non small cell lung cancer (NSCLC) [9, 10].

Dysregulation of RTKs can be activated via multiple mechanisms such as gene mutations, overexpression of ligands, and receptor overexpression. Aberrant activation of mesenchymal-epithelial transition factor (MET) [11-15] and vascular endothelial growth factor receptor 2 (VEGFR-2) [16-18] signaling pathways are two main contributors to tumor angiogenesis, pathogenesis, and progression. These pathways also promote tumor malignancy and invasion with poor prognostic parameters and poor survival [19, 20]. In light of the strong correlation of MET/VEGFR-2 overexpression with tumor malignancies, inhibiting the signaling pathways influenced by MET or VEGFR-2 has been suggested as an important therapeutic strategy for attenuating tumor growth [21-24]. Indeed, several FDA-

approved VEGF pathway inhibitors, such as sunitinib [25], sorafenib [26, 27] and VEGFR2-targeting antibody bevacizumab [22, 28], have shown temporary antitumor effects that can last from weeks to approximately two years in patients. Despite their effectiveness, drug resistance can develop in these tumor cells via adaptation to hypoxia, which strongly implicates MET expression [29-31]. Such resistance from the VEGF pathway-targeted inhibition has led to aggressive tumor invasion and metastasis in murine models of pancreatic cancer [27, 32], glioblastoma [32] and breast cancer [33]. Given their interdependence and connection, simultaneous inhibition of MET and VEGFR2 pathways may achieve enhanced efficacy over the VEGFR2 inhibition alone, leading to the development of broad-spectrum RTK inhibitors such as Cabozantinib.

Cabozantinib is a potent pan-tyrosine kinase inhibitor targeting MET, VEGFR2 and a variety of other RTKs that have been associated with tumor pathobiology [21], such as RET, mast/stem cell growth factor receptor, endothelial-specific receptor and FMS-like tyrosine kinase 3 [34-36]. It has been reported that *in vitro* and *in vivo* cancer cell invasion were significantly reduced through inhibition of MET/VEGFR2 phophorylation following cabozantinib treatment. In addition, antitumor efficacy studies demonstrated that cabozantinib disrupts tumor vasculature, decreases tumor and endothelial cell proliferation, and inhibits tumor growth in mouse models of breast cancers, lung cancers, and glioblastomas [37]. In 2012, cabozantinib was approved by the US Food and Drug administration as the second targeted therapeutic (following vandetanib) for the treatment of medullary thyroid cancer. Currently it is being tested in clinical trials in numerous cancers,

including non-small cell lung cancer, ovarian cancer, hepatocellular carcinoma, glioblastoma, melanoma, colorectal cancer, and prostate cancer [38, 39]. Cabozantinib is reasonably well tolerated by patients with a side effect profile (mainly gastrointestinal and skin effects) similar to other TKIs in the clinic. Early clinical efficacy results in MTC demonstrate a small percentage of patients with partial responses similar to vandetanib [37, 39].

Cabozantinib however is hydrophobic and is practically insoluble in water, so it has been administered mainly via the oral route in a powder or capsule formulation in both preclinical and clinical trials. Daily dosing was calculated to maintain the targeted drug plasma concentration. To improve the solubility of Cabozantinib, some animal studies added hydrochloric acid (10 mM) in saline to formulate cabozantinib in an aqueous solution [37]. Alternatively, cabozantinib was formulated in a vehicle mixture of ethanol/polyethylene glycol (PEG) /reverse osmosis water (5:45:50) in some toxicity and toxicokinetic studies in rats [40]. Assessed by a mass balance study, the bioavailability of the clinical formulation of cabozantinib is at least 27% [41]. However, the poor solubility of cabozantinib may present a challenge for its parental formulation.

Polymeric micelles systems have been extensively evaluated for the delivery of poorly soluble chemotherapeutic agents, due to their attractive bio-physicochemical and structural properties [42-45]. In aqueous solution, amphiphilic polymers, such as 1,2-distearoyl-sn-glycero-3-phosphoethanolamine-N- [methoxy (polyethylene glycol)-2000] (DSPE-PEG_{2000}), poly (ethylene glycol)-poly (ε-

caprolactone (PEG-PCL) or poly (ethylene glycol) -poly (amino acid), self-assemble into core-shell structured nanoparticles with sizes from 10 to 100 nm. In particular, PEG-phospholipid- based micelles have generated significant interest for their sustained delivery of anticancer drugs and excellent biocompatibility [46-49]. In such micelles the hydrophobic environment formed by the long fatty acyl chains can accommodate lipophilic drug molecules to efficiently solubilize these poorly water-soluble drugs and restrict the mobility of the incorporated drugs at the same time, leading to a sustained drug release. Furthermore, the PEG moiety on the hydrophilic shell creates steric hindrance that stabilizes micelles from aggregation, reduces the clearance rate by the reticuloendothelial system (RES), prolongs the circulation time of the drug-loaded micelles [50, 51] and in turn facilitates the tumor accumulation of drug-loaded micelles due to the compromised leaky vasculature [52] found in many solid tumors.

In this study, we have developed a stable cabozantinib-encapsulated DSPE-PEG_{2000} micelles formulation, with sustained release and enhanced delivery into cancer cells. The micellar formulation showed enhanced cytotoxicity and comparable cellular uptake of cabozantinib by human glioblastoma cancer cells and non-small lung cancer cells. The micellar formulation could be stored in the lyophilized form for an extended period of time with 96 % drug recovery, making the micelle formulation a potential candidate for cancer therapy.

2. Materials and Methods

2.1. Materials

N-(Carbonyl-methoxypolyethyleneglycol 2000)-1,2-distearoyl-sn-glycero-3-phosphoethanolamine (DSPE-PEG $_{2000}$ sodium salt) was purchased from NOF AMERICA CORPORATION (White Plains, NY, USA). Cabozantinib was obtained from Chemietek® (Indianapolis, IN, USA). HEPES (BioPerformance Certified, ≥99.5%) and penicillin/streptomycin (in 0.9% NaCl, sterile-filtered, BioReagent) were purchased from Sigma-Aldrich Co (St. Louis, MO, USA). Ammonium acetate (≥97 % HPLC), acetonitrile (≥99.9%) and methanol (≥99.9%) were obtained from Fisher Scientific (Pittsburgh, PA, USA). Dulbecco's Modified Eagle's Medium and trypsin-EDTA were purchased from Life Technologies (Grand Island, NY, USA). Fetal bovine serum (U.S.D.A Origin) was purchased from Biowest LLC (Kansas City, MO, USA). Human malignant glioblastoma cell lines U87 and U251 were kindly provided by Jann Sakaria, (Mayo Clinic, Rochester, MN). Human lung adenocarcinoma epithelial cell line A549 was kindly provided by Dr. Cory Berkland, University of Kansas (Lawrence, KS, USA). Double distilled water (ddH_2O) was used in syntheses, characterization and cell-culture (sterilized by autoclaving).

2.2 Micelles formation and drug loading

2.2.1 Preparation of cabozantinib encapsulated DSPE-PEG$_{2000}$ micelles

DSPE-PEG$_{2000}$ micelles were prepared by the lipid film rehydration method described elsewhere [53] with modifications. Briefly, 20 mg of DSPE-PEG$_{2000}$ and 1.5

mg of cabozantinib were weighed in a 15-mL round bottom flask and dissolved with methanol, followed by bath sonication for 1 min. A thin film of drug-polymer was formed after the organic solvent was removed under reduced pressure by rotary evaporator. Residual methanol was removed by placing the flask on a high vacuum pump (< 0.2 mbar) overnight to thoroughly dry the thin film. The resulting dry film was then rehydrated using 2 mL of 10-mM HEPES-buffered saline (HBS) (pH 7.4). The flask with the cabozantinib loaded DSPE-PEG_{2000} micelles was sonicated for 5 min, placed in a 50°C incubator for 1 h and then cooled to room temperature, followed by passing through a 0.22-μm Nylon syringe filter. The un-encapsulated cabozantinib was removed by ultracentrifugation (MWCO: 3KDa) at 3000 rpm for 10 min. Freshly prepared cabozantinib loaded DSPE-PEG_{2000} micelles were stored at -20 °C overnight and then transferred to -80°C for 2 h, followed by lyophilization below 0.01mbar.

2.2.2 Gel-permeation chromatography

The DSPE-PEG_{2000} micelles encapsulating cabozantinib were characterized by gel-permeation chromatography (GPC) on a Shimadzu 2010CHT HPLC with an evaporative light scattering detector (ELSD-LTII, Shimadzu Scientific Instruments, Inc., Columbia, MA, USA). GPC was performed with a Shodex OHpak SB-803 HQ column (Showa Denko America, Inc., New York, NY) using ddH_2O as the mobile phase at a flow rate of 0.8 mL/min.

2.2.3 ^{1}H Nuclear magnetic resonance (NMR) spectroscopy

The cabozantinib loaded DSPE-PEG_{2000} micelles solution was freshly prepared with ddH_2O and then frozen at -80 °C for 4 h, followed by lyophilization overnight. The ^{1}H NMR spectra of the cabozantinib in $CDCl_3$, DSPE-PEG_{2000} in D_2O and reconstituted dry cabozantinib loaded micelles in D_2O or $CDCl_3$ were collected on a Bruker Avance 400 MHz NMR Spectrometer (Bruker Corporation, MA, USA).

2.2.4 Quantification of cabozantinib amount in the micelles

The amount of cabozantinib incorporated into the DSPE-PEG_{2000} micelles was quantified by gradient reverse phase high-pressure liquid chromatography (HPLC). The HPLC system consisted of a Shimadzu LC-2010CHT (Shimadzu Scientific Instruments, Inc., Columbia, MA, USA) and a SPD-M20A Prominence HPLC Photo Diode Array Detector (Shimadzu Scientific Instruments, Inc., Columbia, MA, USA). An ODS-100 C_{18} analytical column (250 × 4.6 mm; 5 μm) was used for the analysis. The mobile phase consisted of A (10 mM ammonium acetate, pH 5.2) and B (acetonitrile), and the linear gradient was 30-90% B over 12 min at a flow rate of 1.0 mL/min. UV absorption was measured at 240 nm, and the drug loading efficiency (DL %) and encapsulation efficiency (EE %) of cabozantinib in DSPE-PEG_{2000} micelles were calculated using the equations:

DL % = (Weight of the cabozantinib in micelles/ Weight of the cabozantinib and the DSPE-PEG_{2000}) × 100%

EE % = (Weight of the cabozantinib in micelles/ Weight of fed cabozantinib) × 100%

2.3 Micelle size and zeta potential measurements

The hydrodynamic diameter of the micelles was measured by dymanic light scattering (DLS) at 25 °C on a ZetaPALS (Brookhaven Instruments Corp., Holtsville, NY), with measurements repeated three times. Zeta potential of micelles prepared in 10-mM HBS was measured at 25 °C on a ZetaPALS (Brookhaven Instruments Corp., Holtsville, NY), with measurements repeated three times.

2.4 *In vitro* drug release profile of cabozantinib from DSPE-Micelles

The release behavior of cabozantinib from micelles was evaluated using a dialysis method under a sink conditions. Approximately 5 mL of the cabozantinib micellar formulation or the free drug solution was transferred into dialysis tubing (SnakeSkin™, MWCO: 3.5K) (Thermo Scientific Inc., Rockford, IL, USA). To prepare the aqueous solution of cabozantinib, the drug was first dissolved in DMSO and then diluted with 1-mM HCl to reduce the DMSO content to below 0.5% (v/v). The dialysis tubing was closed at both ends with clips and placed in 4.0 L of phosphate buffered saline (PBS) (pH7.4) at 37 °C. A sample of 50 µL was withdrawn from the dialysis tubing at pre-determined time intervals, and the PBS was changed every 4 h to ensure sink condition. The drug amount in each sample was measured according

to section 2.2.4.

2.5 *In vitro* cytotoxicity of cabozantinib from DSPE-Micelles

Two human malignant glioblastoma cell lines (U87 and U251) and a human lung adenocarcinoma epithelial cell line (A549) were used to investigate the *in vitro* cytotoxicity of the cabozantinib micelles. The cell lines were maintained in DMEM supplemented with 10% FBS and 1 % penicillin/streptomycin at 37 °C in a humidified, 5% CO_2 atmosphere. Cancer cells in growth medium were seeded at a concentration of 3,000 cells per well in 96-well flat-bottomed plates and allowed to attach overnight. The cabozantinib aqueous solution (< 0.5% v/v DMSO) or micellar solution was incubated with cells at different final concentrations from 5 to 20 μM. Trichloroacetic acid (TCA) and 10-mM HBS and were added as positive and negative control, respectively. Cell media were refreshed 24 or 48 h after the treatment, and a resazurin-based colorimetric assay was used to assess viability of cell cultures at 72 h post treatment using GraphPad Prism 6 (GraphPad Software Inc., La Jolla, CA).

2.6 Determination of cellular uptake of cabozantinib DSPE-PEG_{2000} micelles

In order to evaluate the cellular uptake and accumulation of cabozantinib micelles, cell lines were seeded at a density of 2×10^5 cells/mL in a 12-well plate. The cells were incubated with free drug solution or cabozantinib micelles at final drug concentrations of 10 or 20 μM for 2 h at conditions described in section 2.5.

Non-internalized drug in the medium was removed, and the attached cells were then washed three times with ice-cold PBS. The cell pellets were collected at 5000 rpm for 10 min at 4 °C after the trypsinization, and they then were resuspended in 0.5 mL of methanol for the quantification following the procedures in section 2.2.4.

2.7 Statistical analysis

All values are expressed as the mean ± standard deviation. One phase exponential association was applied for the curve fitting of the in vitro drug release kinetics to calculate the release half-life ($t_{1/2}$). Statistical analyses were performed using two-way ANOVA with GraphPad Prism 6 and the significance was set at $P < 0.05$.

3. Results and Discussion

3.1 Preparation of cabozantinib in DSPE-PEG_{2000} micelles and determination of drug loading

The poorly-water soluble drug cabozantinib was successfully encapsulated into DSPE-PEG_{2000} micelles by a thin-film rehydration method, and the resulting purified micelle solution was clear without drug precipitates or aggregates (Figure 1A left). A lyophilization process was performed in this study to prepare the dry dosage form and to enhance physical stability for long-term shelf storage. The lyophilized cake (Figure 1A middle) could be redispersed in water (Figure 1A right)

within 30 s.

The formation of the drug-loaded micelles was confirmed by the eluted micelles peak at 6.233 min in the GPC (Figure 1B), which was much earlier than the PEG standard with a similar molecular weight (M_n 3070) as the DSPE-PEG_{2000} monomer. A peak with approximately 3% of the total area under the curve was also detected in the GPC at 12.299 min, which corresponded to the DSPE-PEG_{2000} unimers loss by the micelle dissociation, probably due to the dilution below the critical micelle concentration (CMC) by the HPLC system. The CMC of DSPE-PEG_{2000} micelles is as low as approximately 0.5 – 1.0 uM in HEPES buffer [54] resulting from the strong hydrophobic interaction among the saturated C_{18} acyl chains [54, 55]. The final concentration of the DSPE-PEG_{2000} in this micellar formulation was 7 mM, which is about 7000 fold above the CMC, leading to a successful micelle formation and efficient drug loading.

Drug leakage from colloidal drug delivery systems and subsequent drug precipitation and degradation during extended periods of storage have been observed in several studies due to the nanoparticle aggregation and the hydrolysis of the building blocks of the polymers that formed the nanoparticles [56, 57]. Lyophilization has been used to stabilize a variety of drug nanocarriers [58-62]. Sugars such as trehalose, sucrose, glucose and mannitol are often added at 5 – 20% (w/v) into the particulate systems as cryo/lyoprotectants to spare the products from the freezing/drying stress that may induce aggregation or fusion of nanoparticles. However, collapse of the lyophilized cake was observed for some

formulations containing glucose (5% and 10%, w/v) and mannitol (5%) [63]. In this study, a lyohplized micellar formulation of cabozantinib was prepared without adding cryo/lyoprotectants, and the reconstitution of the resultant lyophilized polymer-drug with water successfully regenerated the micelles. The GPC of the reconstituted drug-loaded micelles (Figure 1C) was found to be same as that of the freshly prepared micelle formulation. The ability of PEG-DSPE micelles to reconstitute without cryoprotectant is probably due to the large hydrophilic-lipophilic balance of the micelles. Successful reconstitution of the indisulam-encapsulated DSPE micelle formulations without a cryoprotectant has also been reported [64].

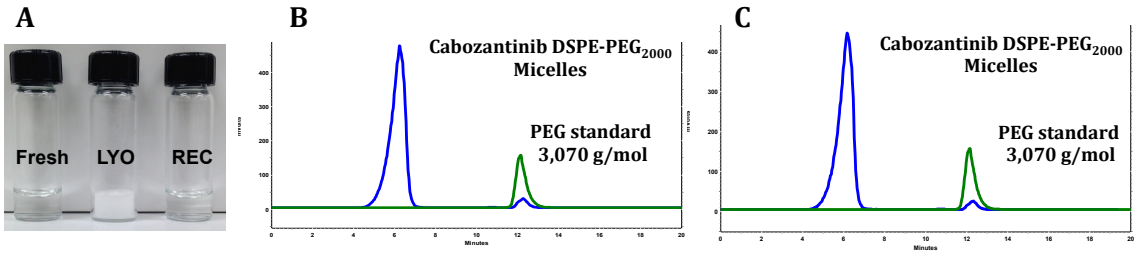

Figure 1. (A) Representative pictures of cabozantinib DSPE-PEG_{2000} micelles in forms of freshly prepared solution (Fresh), lyophilized powder (LYO), and reconstituted solution from the LYO (REC). Gel-permeation chromatography of Freshly prepared cabozantinib DSPE-PEG_{2000} micelles (B) and REC (C) with PEG standard (M.W.: 3,070 g/mol) as an indicator of the DSPE-PEG_{2000} monomer.

^{1}H NMR measurements were used to further demonstrate the encapsulation of the cabozantinib inside the micelle core formed by the DSPE segments [46, 65]. ^{1}H NMR spectra of cabozantinib dissolved in $CDCl_3$ (Figure 2A) and the DSPE-PEG_{2000} in D_2O (Figure 2B) clearly showed the distinct resonance peaks of the drug and the polymer, respectively, which include protons of methoxy groups (4.1240 ppm and 4.1834 ppm), aromatic rings (6.7053 – 8.4693), amino groups (10.2444 ppm) and cyclopropane (1.2754 ppm) for cabozantinib, and the di-saturated C18 acyl chains at 1.2183 ppm and PEG block at 3.6241 ppm for DSPE-PEG_{2000}. By comparison, only prominent peaks corresponding to DSPE-PEG_{2000} could be observed in the ^{1}H NMR spectrum of the cabozantinib loaded micelles (Figure 2C) that were prepared with D_2O due to the restricted motion of the drug molecules in the micelles' hydrophobic cores, indicating efficient drug incorporation. When the lyophilized cabozantinib loaded micelles were reconstituted in the organic solvent, $CDCl_3$, resonance peaks of both the drug and polymer were present ^{1}H NMR spectrum (Figure 2D) as a consequence of the disrupted micelles structure in the organic solvent, which in turn released the drug from the core of micelles.

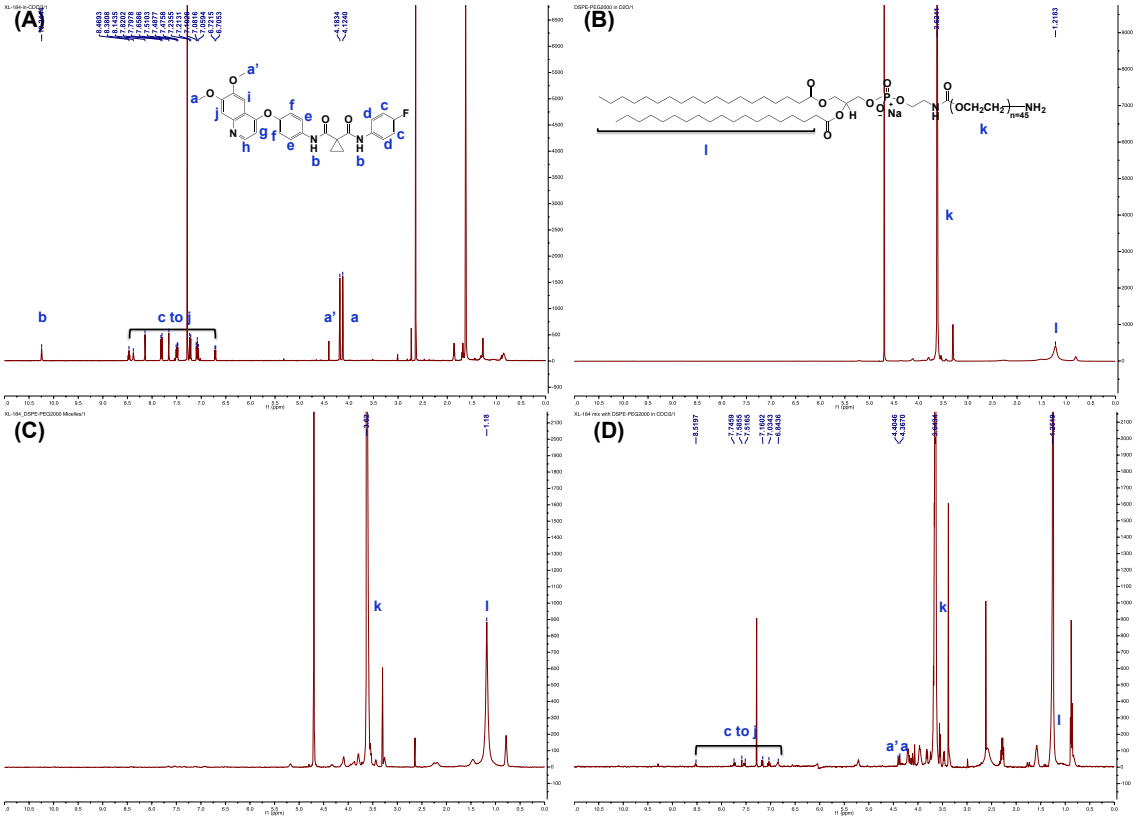

Figure 2. ^{1}H NMR spectra of: (A) Cabozantinib in $CDCL_3$, (B) DSPE-PEG_{2000} in D_2O, (C) Reconstituted cabozantinib loaded micelles in D_2O, (d) Reconstituted cabozantinib loaded micelles in $CDCl_3$.

The loading efficiency (DL %) and encapsulation efficiency (EE %) of the cabozantinib into the DSPE-PEG_{2000} micelles were quantified by the reverse phase HPLC and found to be 5.45 ± 0.09% and 78.37 ± 1.34 %, respectively. Cabozantinib in the neutral form was practically insoluble in water. Remarkably, the aqueous solubility of cabozantinib was increased to 2.23 ± 0.01 mg/mL after being encapsulated into the DSPE-PEG_{2000} micelles. Cabozantinib loaded micelles in the lyophilized cake could be easily rehydrated with water, and the detected drug amount was 96.00 ± 0.87 % of the freshly prepared micelles solution. This high drug recovery indicates a promising prolonged shelf life of the lyophilized cabozantinib micelles for clinical applications.

3.2 Micelle characterization

The average hydrodynamic size of the oblate spheroidal cabozantinib loaded micelles was 11.7 nm with a narrow size distribution (Figure 3), which is favorable for sustained circulation for *in vivo* delivery of the drug-incorporated micelles. It has been reported that micelles with size in the nano-scale range (10 -100 nm) can resist the systemic clearance by renal filtration and the reticuloendothelial system after administration [51, 66], thus providing a prolonged pharmacological effect. In addition, cabozantinib molecules incorporated into the hydrophobic core of micelles are protected from the liver enzyme metabolism. Consequently, drug transportation to targeted extravascular tumor tissues through diffusion from the leaky blood vessels [52] is expected to be significantly enhanced due to the prolonged systemic

circulation of the drug-loaded micelles.

The zeta potential value indicates the potential colloidal stability of the micellar formulation. Colloidal systems with zeta potential above ± 30 mV have been generally accepted as moderately stable to prevent aggregation. The zeta potential of the cabozantinib-loaded micelles was -15.70 ± 1.24 mV, indicating an incipient instability. However, the hydrophilic PEG segment on the surface could prevent aggregation of micelles in solution due to its steric hindrance.

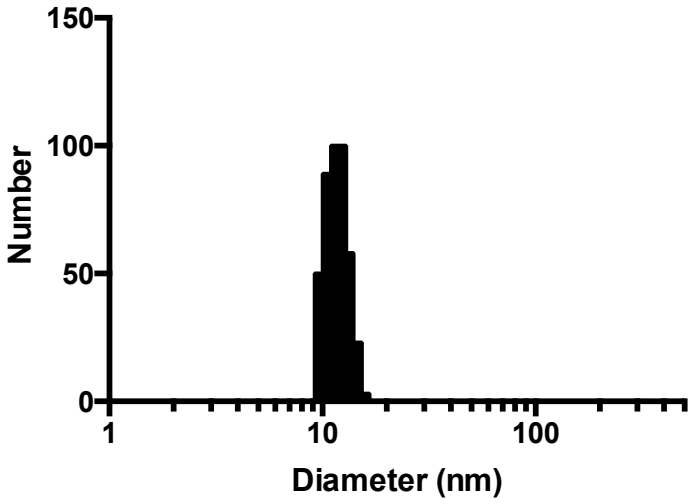

Figure 3. Dynamic Light Scattering (DLS) of the freshly prepared cabozantinib DSPE-PEG_{2000} micelles at 25° C (size distribution in number). Hydrodynamic diameter= 11.7 ± 1.2 nm. (Mean ± SD) (N = 3).

3.3 *In vitro* drug release profile of cabozantinib from DSPE-PEG_{2000} micelles

The *in vitro* release behaviors of the micellar formulation of cabozantinib and the free drug were evaluated in PBS (pH 7.4) solution at 37 °C under the sink conditions to simulate the significant dilution of the administered micelle solution by physiological fluids. As shown in Figure 4, approximately 81% of cabozantinib in the free drug solution was released within 4h. DSPE-PEG_{2000} micelles containing cabozantinib, on the other hand, exhibited sustained drug release over a period of greater than 10 days, with only 21.92% of the cabozantinib released in the first 8h. Release half-times of the drug in both forms were calculated from a curve fitting using one phase exponential association analysis. The $t_{1/2}$ was significantly enhanced from less than 10min to 80h after the drug was incorporated into the micelles formulation, and similar *in vitro* controlled drug release profiles of DSPE-PEG micelles have been reported when hydrophobic drugs such as doxorubicin [67] and ridaformolimus [68] were encapsulated.

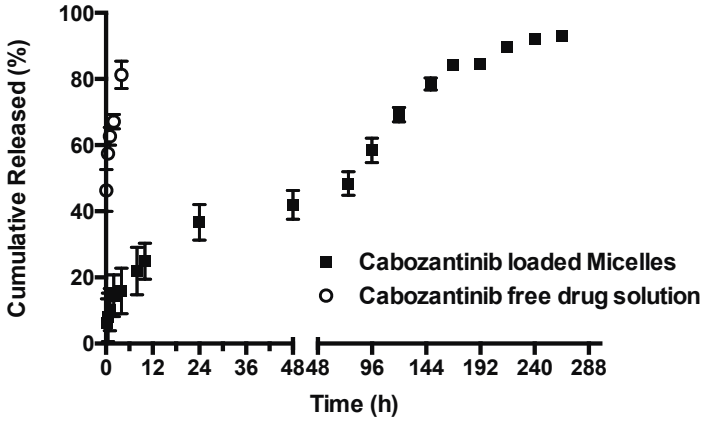

Figure 4. *In vitro* drug release profiles of cabozantinib in free drug form (O) and in DSPE-PEG_{2000} formulation (■). (Mean ± SD; N=3).

Repeat-dose toxicity and toxicokinetic studies with cabozantinib in rats that received daily oral gavage have shown debilitating side effects, including hematopoietic, hepatic, gastrointestinal or renal toxicity [40].Polymeric micelles that incorporate PEG segment have been employed as long-circulating drug vehicles [65, 69, 70], as the presence PEG in the outer hydrophilic shell spares micelles from aggregation and also decreases the adsorption of protein such as immunoglobulins to the hydrophobic surfaces, thus reducing the fast clearance of the micelles by RES [71, 72]. Moreover, following the intravenous injection, the nanoscale drug-loaded micelles have been found to preferentially accumulate in the tumor tissues from their leaky endothelial vasculature, due to the enhanced permeability and retention effect [73-75]. Our study demonstrated a significantly prolonged in vitro release profile of the cabozantinib from the micellar formulation due to the strong drug interaction and association with the hydrophobic micelle core, which is responsible for maintaining a steady-state drug release at a partial level from day 6, and indicates a potentially enhanced *in vivo* drug stability and increased systemic circulation. After intravenously administered into the patients, cabozantinib-loaded DSPE-PEG_{2000} micelles are expected to target the tumor tissue and then controllably release the active chemotherapeutic agent. Consequently, the systemic toxicity of the drug could be minimized as the chemotherapy exposure to normal tissues, especially hematopoietic cells and epithelial cells in the gastrointestinal tract, is reduced.

3.4 Cellular uptake of cabozantinib from DSPE-PEG_{2000} micelles

Human lung adenocarcinoma epithelial cell line A549 and human malignant glioblastoma cell lines U87 and U251 were treated with free cabozantinib solution or drug loaded DSPE-PEG_{2000} micelles for 2h, and the drug amounts internalized in cells were then quantified using the RP-HPLC. As shown in Figure 5, micellar formulation of cabozantinib significantly enhanced the cellular accumulation of the drug in all cell lines under study at the concentration of 10 μM. Similarly, enhanced cellular uptake of hydrophobic drug-loaded micelles has been reported in the case of doxorubincin [76]. The enhanced intracellular uptake was possibly due to the different internalization mechanisms employed by the micellar formulation and the free drug. Several groups have investigated the mechanisms of micelle internalization by cancer cells using biocompatible fluorescent micelles [77]. Drug-loaded micelles have been shown to enter the cytoplasmic compartment by the endocytosis process, followed by the diffusion of the incorporated molecules into organelles such as lyposomes, mitochondria and the Golgi apparatus. In comparison, free drug molecules slowly traversed through the cell membrane and then entered the cytoplasmic space. To our surprise, no statistical significance was observed at the fed cabozantinib concentration of 20 μM. We hypothesized that the increased initial drug concentration may generate an elevated drug gradient to facilitate the passive diffusion of the free drug solution, leading to intracellular drug uptake comparable with drug-loaded micelles. On the other hand, the relatively small number of experiment replicate probably should also be taken into account.

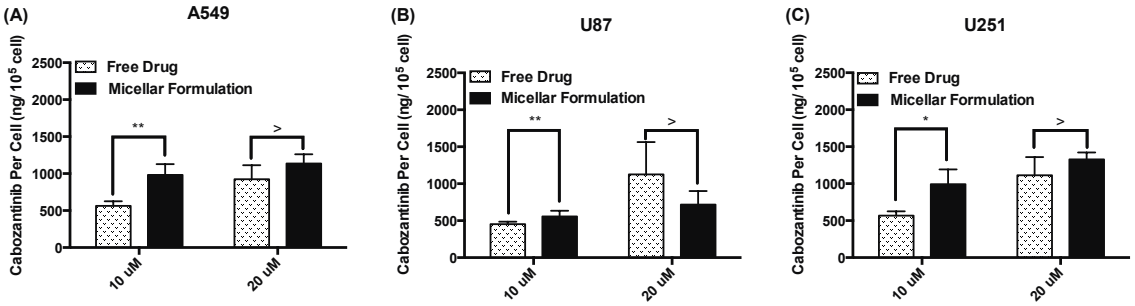

Figure 5. Celluar uptake of cabozantinib in the micellar formulation (solid) or aqueous solution (shaded) by (A) A549 cells, (B) U87 cells and (C) U251 cells. (Mean ± SD; N=3) (*:p<0.05; **: p<0.01).

3.5 *In vitro* cytotoxicity of cabozantinib from DSPE-PEG$_{2000}$ Micelles

Cabozantinib is currently being tested in cancer patients with non-small cell lung cancer, glioblastoma, melanoma, ovarian cancer and hepatocellular carcinoma, etc. We chose one human non-small cell lung cancer cell line A549 and two human malignant glioblastoma cell lines U87 and U251 in this pilot study to investigate the cytotoxicity of the cabozantinib-loaded DSPE-PEG$_{2000}$ micelles. The results of cytotoxicity study on free cabozantinib and cabozantinib-loaded micelles solution against the three cell lines are shown in Figure 6. Overall, we observed strong dose and time-dependent inhibitory activity in all cell lines under study from 5 to 20 μM. Compared to the free drug solution, the cabozantinib micellar formulation exhibited significantly enhanced cytotoxicity after 24h or 48h of incubation. Higher cytotoxic activity has also been demonstrated in other anticancer drug-loaded nanoparticles. For example, a doxorubicin-loaded polymeric nanoparticle was found to be over 30 times more active drug-resistant MCF-7 tumor cells than free drug [78], and it was attributed to the increased intracellular drug concentration. Diao et al later reported reversed multidrug resistance using doxorubicin-loaded PEG-PCL copolymer micelles in multidrug-resistant K562 cells [76]. Among the three human tumor cell lines, the U87 and A549 cell lines were more sensitive to the treatment than the U251 cell line, probably due to varying levels of VEGFR-2/MET expression and intracellular drug concentration.

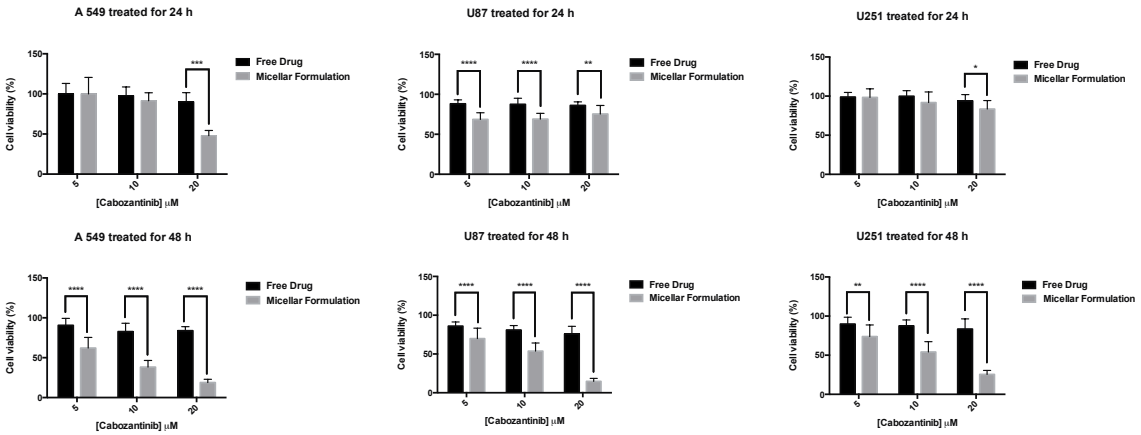

Figure 6. Cytotoxicity determined by Resazurin Assay in A549 cells, U87 cells and U251 cells after 24 h or 48 h treatment with cabozantinib loaded DSPE-PEG2000 micelles (black) or cabozantinib solution (gray). (Mean ± SD; N=3) (*: $p < 0.05$; **: $p<0.01$; ****: $p<0.0001$).

4. Conclusions

In the present work, we successfully solubilized cabozantinib, a dual MET/VEGFR2 inhibitor, in an 11-nm DSPE-PEG_{2000} micellar formulation with encapsulation efficiency of approximately 80 %. The drug-loaded micelles were stabilized in the lyophilized form. Therefore, it could provide extended shelf life without using cryo/lyoprotectants. The sustained *in vitro* release profiles indicated a potentially prolonged *in vivo* circulation after administration for the long-acting chemotherapy. Compared with the free cabozantinib solution, drug-loaded micelles exhibited increased intracellular drug uptake and higher cytotoxicity in one human lung adenocarcinoma epithelial cell line and two human malignant glioblastoma cell lines. In conclusion, cabozantinib can be formulated as a highly concentrated drug in an aqueous injectable solution above the solubility limit of the free drug, thus lowering the required dosage volume. Therefore, administration of cabozantinib-incorporated micelles may serve as a promising approach to parenteral formulation of a chemotherapeutic agent against human malignant solid tumors.

5. References

1. Di Renzo, M.F., et al., *Somatic mutations of the MET oncogene are selected during metastatic spread of human HNSC carcinomas.* Oncogene, 2000. **19**(12): p. 1547-55.
2. Ball, D.W., *Medullary thyroid cancer: therapeutic targets and molecular markers.* Curr Opin Oncol, 2007. **19**(1): p. 18-23.

3. Machens, A., K. Lorenz, and H. Dralle, *Constitutive RET tyrosine kinase activation in hereditary medullary thyroid cancer: clinical opportunities.* J Intern Med, 2009. **266**(1): p. 114-25.

4. Drosten, M. and B.M. Putzer, *Mechanisms of Disease: cancer targeting and the impact of oncogenic RET for medullary thyroid carcinoma therapy.* Nat Clin Pract Oncol, 2006. **3**(10): p. 564-74.

5. Castellone, M.D. and M. Santoro, *Dysregulated RET signaling in thyroid cancer.* Endocrinol Metab Clin North Am, 2008. **37**(2): p. 363-74, viii.

6. Reardon, D.A. and P.Y. Wen, *Therapeutic advances in the treatment of glioblastoma: rationale and potential role of targeted agents.* Oncologist, 2006. **11**(2): p. 152-64.

7. Cancer Genome Atlas Research, N., *Comprehensive genomic characterization defines human glioblastoma genes and core pathways.* Nature, 2008. **455**(7216): p. 1061-8.

8. Kunkel, P., et al., *Expression and localization of scatter factor/hepatocyte growth factor in human astrocytomas.* Neuro Oncol, 2001. **3**(2): p. 82-8.

9. Dy, G.K. and A.A. Adjei, *Emerging therapeutic targets in non-small cell lung cancer.* Proc Am Thorac Soc, 2009. **6**(2): p. 218-23.

10. Horn, L. and A.B. Sandler, *Angiogenesis in the treatment of non-small cell lung cancer.* Proc Am Thorac Soc, 2009. **6**(2): p. 206-17.

11. Rong, S., et al., *Invasiveness and metastasis of NIH 3T3 cells induced by Met-hepatocyte growth factor/scatter factor autocrine stimulation.* Proc Natl Acad Sci U S A, 1994. **91**(11): p. 4731-5.

12. Michieli, P., et al., *Targeting the tumor and its microenvironment by a dual-function decoy Met receptor.* Cancer Cell, 2004. **6**(1): p. 61-73.

13. Abounader, R. and J. Laterra, *Scatter factor/hepatocyte growth factor in brain tumor growth and angiogenesis.* Neuro Oncol, 2005. **7**(4): p. 436-51.

14. Laterra, J., et al., *Scatter factor/hepatocyte growth factor expression enhances human glioblastoma tumorigenicity and growth.* Biochem Biophys Res Commun, 1997. **235**(3): p. 743-7.

15. Lamszus, K., et al., *Scatter factor promotes motility of human glioma and neuromicrovascular endothelial cells.* Int J Cancer, 1998. **75**(1): p. 19-28.

16. Viglietto, G., et al., *Upregulation of vascular endothelial growth factor (VEGF) and downregulation of placenta growth factor (PlGF) associated with malignancy in human thyroid tumors and cell lines.* Oncogene, 1995. **11**(8): p. 1569-79.

17. Belletti, B., et al., *Modulation of in vivo growth of thyroid tumor-derived cell lines by sense and antisense vascular endothelial growth factor gene.* Oncogene, 1999. **18**(34): p. 4860-9.

18. Capp, C., et al., *Increased expression of vascular endothelial growth factor and its receptors, VEGFR-1 and VEGFR-2, in medullary thyroid carcinoma.* Thyroid, 2010. **20**(8): p. 863-71.

19. Xin, X., et al., *Hepatocyte growth factor enhances vascular endothelial growth factor-induced angiogenesis in vitro and in vivo.* Am J Pathol, 2001. **158**(3): p. 1111-20.

20. Van Belle, E., et al., *Potentiated angiogenic effect of scatter factor/hepatocyte growth factor via induction of vascular endothelial growth factor: the case for paracrine amplification of angiogenesis.* Circulation, 1998. **97**(4): p. 381-90.

21. Exelixis, I., *Exelixis Files IND Application for Anticancer Compound XL184*, 2005, PR Newswire.

22. Donovan, E.A. and S. Kummar, *Targeting VEGF in cancer therapy.* Curr Probl Cancer, 2006. **30**(1): p. 7-32.

23. Abounader, R., et al., *In vivo targeting of SF/HGF and c-met expression via U1snRNA/ribozymes inhibits glioma growth and angiogenesis and promotes apoptosis.* FASEB J, 2002. **16**(1): p. 108-10.

24. Abounader, R., et al., *Reversion of human glioblastoma malignancy by U1 small nuclear RNA/ribozyme targeting of scatter factor/hepatocyte growth factor and c-met expression.* J Natl Cancer Inst, 1999. **91**(18): p. 1548-56.

25. Motzer, R.J., et al., *Overall survival and updated results for sunitinib compared with interferon alfa in patients with metastatic renal cell carcinoma.* J Clin Oncol, 2009. **27**(22): p. 3584-90.

26. Escudier, B., et al., *Sorafenib in advanced clear-cell renal-cell carcinoma.* N Engl J Med, 2007. **356**(2): p. 125-34.

27. Zhao, J., et al., *Sorafenib or sunitinib as postoperative adjuvant therapy for Chinese patients with locally advanced clear cell renal cell carcinoma at high risk for disease recurrence.* Urol Oncol, 2013. **31**(8): p. 1800-5.

28. Hurwitz, H., et al., *Bevacizumab plus irinotecan, fluorouracil, and leucovorin for metastatic colorectal cancer.* N Engl J Med, 2004. **350**(23): p. 2335-42.

29. Kitajima, Y., et al., *Induction of hepatocyte growth factor activator gene expression under hypoxia activates the hepatocyte growth factor/c-Met system via hypoxia inducible factor-1 in pancreatic cancer.* Cancer Sci, 2008. **99**(7): p. 1341-7.

30. Pennacchietti, S., et al., *Hypoxia promotes invasive growth by transcriptional activation of the met protooncogene.* Cancer Cell, 2003. **3**(4): p. 347-61.

31. Bergers, G. and D. Hanahan, *Modes of resistance to anti-angiogenic therapy.* Nat Rev Cancer, 2008. **8**(8): p. 592-603.

32. Paez-Ribes, M., et al., *Antiangiogenic therapy elicits malignant progression of tumors to increased local invasion and distant metastasis.* Cancer Cell, 2009. **15**(3): p. 220-31.

33. Ebos, J.M., et al., *Accelerated metastasis after short-term treatment with a potent inhibitor of tumor angiogenesis.* Cancer Cell, 2009. **15**(3): p. 232-9.

34. Timar, J. and B. Dome, *Antiangiogenic drugs and tyrosine kinases.* Anticancer Agents Med Chem, 2008. **8**(5): p. 462-9.

35. Small, D., *FLT3 mutations: biology and treatment.* Hematology Am Soc Hematol Educ Program, 2006: p. 178-84.

36. Castellone, M.D., et al., *Receptor tyrosine kinase inhibitors in thyroid cancer.* Best Pract Res Clin Endocrinol Metab, 2008. **22**(6): p. 1023-38.

37. Yakes, F.M., et al., *Cabozantinib (XL184), a novel MET and VEGFR2 inhibitor, simultaneously suppresses metastasis, angiogenesis, and tumor growth.* Mol Cancer Ther, 2011. **10**(12): p. 2298-308.

38. Exelixis, I., *Exelixis Clinical Trials*, 2014: http://www.exelixis.com.

39. Zhang, Y., et al., *XL-184, a MET, VEGFR-2 and RET kinase inhibitor for the treatment of thyroid cancer, glioblastoma multiforme and NSCLC.* IDrugs, 2010. **13**(2): p. 112-21.

40. Brower, M., *Pharmacology/toxicology NDA review and evaluation-Cabozantinib (S)-malate (Cometriq)*, 2012: http://www.accessdata.fda.gov/drugsatfda_docs/nda/2012/203756Orig1s000PharmR.pdf.

41. Agency, E.M., *Cometriq International non-proprietary name: cabozantinib*, 2013.

42. Gaucher, G., et al., *Polymeric micelles for oral drug delivery.* Eur J Pharm Biopharm, 2010. **76**(2): p. 147-58.

43. Lukyanov, A.N. and V.P. Torchilin, *Micelles from lipid derivatives of water-soluble polymers as delivery systems for poorly soluble drugs.* Adv Drug Deliv Rev, 2004. **56**(9): p. 1273-89.

44. Torchilin, V.P., *Micellar nanocarriers: pharmaceutical perspectives.* Pharm Res, 2007. **24**(1): p. 1-16.

45. Sezgin, Z., N. Yuksel, and T. Baykara, *Preparation and characterization of polymeric micelles for solubilization of poorly soluble anticancer drugs.* Eur J Pharm Biopharm, 2006. **64**(3): p. 261-8.

46. Gill, K.K., S. Nazzal, and A. Kaddoumi, *Paclitaxel loaded PEG(5000)-DSPE micelles as pulmonary delivery platform: formulation characterization, tissue distribution, plasma pharmacokinetics, and toxicological evaluation.* Eur J Pharm Biopharm, 2011. **79**(2): p. 276-84.

47. Torchilin, V.P., *Lipid-core micelles for targeted drug delivery.* Curr Drug Deliv, 2005. **2**(4): p. 319-27.

48. Croy, S.R. and G.S. Kwon, *Polymeric micelles for drug delivery.* Curr Pharm Des, 2006. **12**(36): p. 4669-84.

49. Dabholkar, R.D., et al., *Polyethylene glycol-phosphatidylethanolamine conjugate (PEG-PE)-based mixed micelles: some properties, loading with paclitaxel, and modulation of P-glycoprotein-mediated efflux.* Int J Pharm, 2006. **315**(1-2): p. 148-57.

50. Jones, M. and J. Leroux, *Polymeric micelles - a new generation of colloidal drug carriers.* Eur J Pharm Biopharm, 1999. **48**(2): p. 101-11.

51. Alexis, F., et al., *Factors affecting the clearance and biodistribution of polymeric nanoparticles.* Mol Pharm, 2008. **5**(4): p. 505-15.

52. Maeda, H., et al., *Tumor vascular permeability and the EPR effect in macromolecular therapeutics: a review.* J Control Release, 2000. **65**(1-2): p. 271-84.

53. Sawant, R., et al., *Nanosized cancer cell-targeted polymeric immunomicelles loaded with superparamagnetic iron oxide nanoparticles.* Journal of Nanoparticle Research, 2009. **11**(7): p. 1777-1785.

54. Ashok, B., et al., *In vitro characterization of PEGylated phospholipid micelles for improved drug solubilization: effects of PEG chain length and PC incorporation.* J Pharm Sci, 2004. **93**(10): p. 2476-87.

55. Uster, P.S., et al., *Insertion of poly(ethylene glycol) derivatized phospholipid into pre-formed liposomes results in prolonged in vivo circulation time.* FEBS Lett, 1996. **386**(2-3): p. 243-6.

56. Chacon, M., et al., *Stability and freeze-drying of cyclosporine loaded poly(D,L lactide-glycolide) carriers.* Eur J Pharm Sci, 1999. **8**(2): p. 99-107.

57. Moretton, M.A., et al., *Molecular implications in the nanoencapsulation of the anti-tuberculosis drug rifampicin within flower-like polymeric micelles.* Colloids Surf B Biointerfaces, 2010. **79**(2): p. 467-79.

58. Hu, Y., et al., *Physical stability and lyophilization of poly(epsilon-caprolactone)-b-poly(ethyleneglycol)-b-poly(epsilon-caprolactone) micelles.* J Nanosci Nanotechnol, 2006. **6**(9-10): p. 3032-9.

59. Abdelwahed, W., et al., *Freeze-drying of nanoparticles: formulation, process and storage considerations.* Adv Drug Deliv Rev, 2006. **58**(15): p. 1688-713.

60. Moretton, M.A., D.A. Chiappetta, and A. Sosnik, *Cryoprotection-lyophilization and physical stabilization of rifampicin-loaded flower-like polymeric micelles.* J R Soc Interface, 2012. **9**(68): p. 487-502.

61. Richter, A., et al., *Polymeric micelles for parenteral delivery of sagopilone: physicochemical characterization, novel formulation approaches and their toxicity assessment in vitro as well as in vivo.* Eur J Pharm Biopharm, 2010. **75**(2): p. 80-9.

62. Yang, Z.L., et al., *Amphotericin B-loaded poly(ethylene glycol)-poly(lactide) micelles: preparation, freeze-drying, and in vitro release.* J Biomed Mater Res A, 2008. **85**(2): p. 539-46.

63. Di Tommaso, C., et al., *Investigations on the lyophilisation of MPEG-hexPLA micelle based pharmaceutical formulations.* Eur J Pharm Sci, 2010. **40**(1): p. 38-47.

64. Cesur, H., et al., *Self-associated indisulam in phospholipid-based nanomicelles: a potential nanomedicine for cancer.* Nanomedicine, 2009. **5**(2): p. 178-83.

65. Shin, H.C., et al., *Multi-drug loaded polymeric micelles for simultaneous delivery of poorly soluble anticancer drugs.* J Control Release, 2009. **140**(3): p. 294-300.

66. McDonald, D.M. and P. Baluk, *Significance of blood vessel leakiness in cancer.* Cancer Res, 2002. **62**(18): p. 5381-5.

67. Kumar, R., et al., *In vitro evaluation of theranostic polymeric micelles for imaging and drug delivery in cancer.* Theranostics, 2012. **2**(7): p. 714-22.

68. Remsberg, C.M., et al., *Pharmacokinetic Evaluation of a DSPE-PEG2000 Micellar Formulation of Ridaforolimus in Rat.* Pharmaceutics, 2012. **5**(1): p. 81-93.

69. Adams, M.L., D.R. Andes, and G.S. Kwon, *Amphotericin B encapsulated in micelles based on poly(ethylene oxide)-block-poly(L-amino acid) derivatives exerts reduced in vitro hemolysis but maintains potent in vivo antifungal activity.* Biomacromolecules, 2003. **4**(3): p. 750-7.

70. Kwon, G.S. and K. Kataoka, *Block copolymer micelles as long-circulating drug vehicles.* Adv Drug Deliv Rev, 1995. **16**(2–3): p. 295--309.

71. Kwon, G., et al., *Enhanced tumor accumulation and prolonged circulation times of micelle-forming poly (ethylene oxide-aspartate) block copolymer-adriamycin conjugates.* J Control Release, 1994. **29**(1–2): p. 17-23.

72. Jeon, S.I., et al., *Protein—surface interactions in the presence of polyethylene oxide: I. Simplified theory.* J Colloid Interface Sci, 1991. **142**(1): p. 149-158.

73. Dand, N., et al., *Polymeric micelles as a drug carrier for tumor targeting.* CYS, 2013. **4**(2): p. 94-101.

74. Matsumura, Y. and H. Maeda, *A new concept for macromolecular therapeutics in cancer chemotherapy: mechanism of tumoritropic accumulation of proteins and the antitumor agent smancs.* Cancer Res, 1986. **46**(12 Pt 1): p. 6387-92.

75. Maeda, H., *The enhanced permeability and retention (EPR) effect in tumor vasculature: the key role of tumor-selective macromolecular drug targeting.* Adv Enzyme Regul, 2001. **41**: p. 189-207.

76. Diao, Y.Y., et al., *Doxorubicin-loaded PEG-PCL copolymer micelles enhance cytotoxicity and intracellular accumulation of doxorubicin in adriamycin-resistant tumor cells.* Int J Nanomedicine, 2011. **6**: p. 1955-62.

77. Savic, R., et al., *Micellar nanocontainers distribute to defined cytoplasmic organelles.* Science, 2003. **300**(5619): p. 615-8.

78. Yi, Y., et al., *A polymeric nanoparticle consisting of mPEG-PLA-Toco and PLMA-COONa as a drug carrier: improvements in cellular uptake and biodistribution.* Pharm Res, 2005. **22**(2): p. 200-8.

Chapter 5

Synthesis and *In Vitro* Evaluation of A Hyaluronic Acid-Deferoxamine Conjugate for Local Treatment of Bone Regeneration

1. Introduction

Radiotherapy is currently applied in approximately 67% of all cancer patients, either alone or in combination with chemotherapy and surgery [1]. Radiation treatment uses high-energy waves such as x-ray, γ-ray, or electron beams to induce double-strand DNA breaks in cancer cells, thus disrupting tumor vessel and inhibiting tumor growth [2]. In spite of its therapeutic efficacy, radiation has been well known to suppress angiogenesis [3] and destruct microvasculature as well, causing many severe complications including teleangectasia, capillary rupture and thrombosis to capillaries or sinusoids, and fibrinoid necrosis, thrombosis and acute arteritis to medium-sized vessels[4, 5]. Moreover, the pathologic effects of radiotherapy are also evident in appreciable low bone density and bone fractures [6, 7].

Deferoxamine (DFO) is a bacterial siderophore naturally synthesized by Streptomyces pilosus and has the ability to strongly bind to the excess free iron ions in plasma. Such bindings can prevent the iron-driven free-radical reactions that lead to various deleterious events such as lipids peroxidation and damage of proteins and nucleic acids[8-10]. DFO has been clinically used as a first-line iron-chelating agent to treat acute iron overload and transfusion-related blood poisoning [11-18]. Iron also serves as a co-

factor in a degradation process, known as prolyl hydroxylation, of the hypoxia-inducible factor-1α (HIF-1 α). HIF-1 α has been reported to be associated with bone deposition and normal skeletal development. In a rat model, HIF-1 α stimulates the release of the vascular endothelial growth factor to subsequently promote angiogenesis, which is necessary for bone formation[19]. The iron-removal ability of DFO has been experimentally implicated to stimulate angiogenesis, accelerate bone regeneration and activate the HIF-1 α pathway by inhibiting the prolyl hydroxylation process [20-22].

Recently, a novel clinical application of DFO has been reported in reversing radiation-induced bone damages via targeting angiogenesis. In this application, adult rats were first subjected to a human-equivalent dose of radiotherapy to induce the lesion and then received local DFO injection treatment. Compared with the untreated animals, the treated group showed a substantially enhanced vascular proliferation illustrated by micro-computed tomography angiography [23]. Some similar studies observed a nearly full recovery in terms of callus size, quality, strength and a 3-fold increase in the bony union rate after the localized DFO injection [24, 25].

Despite such encouraging experimental results, two major limitations hinder a wide clinical application of DFO therapy. One limitation is its poor oral bioavailability (~15%)

due to its high hydrophilicity, charge and susceptibility to the highly acidic environment in the stomach lumen [26-28]. DFO is therefore administered primarily via either subcutaneous, intravenous infusion or occasionally by intramuscular injection. The other limitation of DFO is its short plasma half-life, which is typically 5 - 10 min in humans after intravenous bolus injections [29]. Moreover, the amide bonds of DFO are also subject to the proteolytic cleavage, accelerating the rapid renal excretion of DFO. Collectively, these limitations necessitate continuous infusion or repeated injections of DFO, which might raise issues in hypotension, tachycardia, neurotoxicity, ocular dysfunction and patients' compliance [30-32], rendering treatments ineffective. To achieve the extended release of DFO, researchers have tested numerous delivery systems, including liposomal formulation [33, 34] and high-molecular-weight polymer-DFO conjugates [35-38]. Particularly one delivery system, drug conjugates prepared with starch or dextran, has led to both enhanced tolerability and prolonged drug residence time following the intravenous infusion.

In this study, we set out to strategically enhance the therapeutic efficacy of the DFO via covalently attaching the drug molecule hyaluronic acid (HA). HA plays critical role in cell differentiation, tissue morphogenesis, proliferation and wound healing [39, 40]. HA-based biomaterials have been widely applied for tissue engineering and regenerative medicine [41, 42]. For example, HA with high molecular weight is currently used as a

symptom-modifying treatment as a lubricant and shock-adsorbent for human osteoarthritis, the most common joint disorder, to improve chondrocytes density and matrix appearance [43-45]. Herein, we first prepared a HA conjugated deferoxamine (HA-DFO) using a two-step synthesis method. We then examined the *in vitro* release characteristics and the potential cell toxicity of the HA-DFO. Biodegradability of the HA-DFO conjugate was compared with the unmodified HA in a simulated physiological medium. Our results suggested that HA-DFO bio-conjugate offered the sustained release of the active DFO. Moreover, the combined therapeutic effects of DFO and HA could be achieved after a local administration.

2. Materials and Methods

2.1. Materials

Hyaluronan sodium salts (215-kDa and 752-kDa) were purchased from Lifecore Biomedical, Inc. (Chaska, MN). Dowex® 50W X8, Tetrabutylammonium hydroxide solution, deferoxamine mesylate, N-(3-dimethylaminopropyl)-N′-ethylcarbodiimide (EDC), 1,4-piperazine-bis (ethanesulfonic acid) (PIPES) and Hyaluronidase from bovine testes (EC 3.2.1.35, 750-3000 U/mg) were purchased from Sigma Aldrich (St. Louis, MO). Sulfo- NHS

was purchased from ChemPep, Inc. (Wellington, FL). 8-Hydroxyquinoline-5-sulfonic acid monohydrate was purchased from TCI America (Portland, OR). Iron (III) chloride (anhydrous, 98%) was obtained from Alfa Aesar (Ward Hill, MA). Human umbilical vein endothelial cells (ATCC®, Manassas, VA) were grown in endothelial cell growth media kit from Lonza (Allendale, NJ). Double distilled water (ddH_2O) was used in syntheses, characterization and cell-culture (sterilized by autoclaving). Organic solvents are of analytical grade from Fisher Scientific (Lenexa, KS).

2.2 Synthesis of hyaluronic acid (HA)-deferoxamine (DFO) conjugate (Figure 1)

HA-tetrabutylammonium salt (HA-TBA) The HA-TBA was prepared from the hyaluronan sodium salts according to a previously disclosed ion-exchange method [46]. Briefly, 30 mg of HA (215 kDa or 752 kDa) was first dissolved in 30 mL of ddH_2O in a round bottom flask, and then approximately 600 mg of Dowex® 50W X8 cation exchange resin was added into the flask and stirred overnight. The HA/resin mixture was filtered through a syringe filter (5-μm Nylon, Thermo Scientific, Rockwood, TN), and the pH of the filtrate was adjusted with the TBA hydroxide solution until the color of the solution turned to light pink. The resultant HA-TBA solution was lyophilized to afford the dried HA-TBA salt.

HA-deferoxamine (HA-DFO) Approximately 30 mg of lyophilized HA-TBA was dissolved in 10 mL of DMSO with vigorous stirring, followed by EDC (3 eq; 22.52 mg) and sulfo-NHS (3 eq; 39.62 mg) to activate the carboxylic acid group on HA. After 2 h, DFO (3 eq; 94.87 mg) in 250 μL of DMSO was added into the mixture. The reaction was carried out for 24 h at ambient temperature. The resultant solution was first dialyzed against 50-mM sodium chloride (MWCO 10 kDa) for 24 h with dialysis medium replaced every 2h, and then the dialysis was performed in ddH_2O for 72 h before lyophilization to yield the HA-DFO in a dry form.

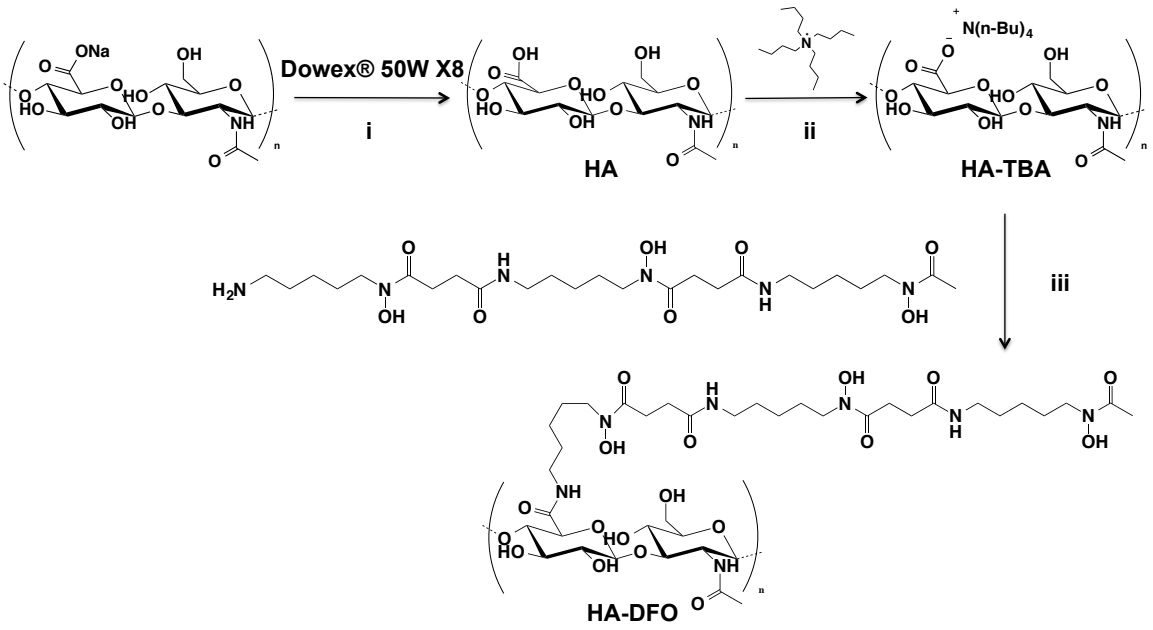

Figure 1. Synthetic scheme of HA-TBA and HA-DFO: (i) overnight, rt; (ii)pH 8.0; (iii) EDC/Sulfo-NHS, DMSO, rt

2.3 ^{1}H Nuclear magnetic resonance (NMR) spectroscopy

The HA sodium salts, DFO, and HA (215 kDa or 752 kDa) were dissolved in deuterium oxide (D_2O) and their 1H NMR spectra were collected on a Bruker Avance 400 MHz NMR Spectrometer (Bruker Corporation, MA, USA).

2.4 Quantification of DFO in the HA-DFO conjugates

DFO has been reported to chelate iron in the oxidation state of +3 to form a 1:1 DFO-Iron (III) chelate complex, ferrioxamine [47], which has a maximum absorption at 430 nm ($\Delta\varepsilon = 2500 M^{-1}\cdot cm^{-1}$) [48, 49]. The degree of conjugation (DS%) was determined spectrophotometrically by converting the HA-DFO to the iron-saturated ferrioxamine using a modified method[35]. Typically, 3 mM of iron (III) chloride ($FeCl_3$) was incubated with a series of standard solutions of DFO (0.05–0.5 mg/mL), 1-mg/mL HA (215 kDa)-DFO or HA (752 kDa)-DFO at ambient temperature for 16 h, followed by recording the absorption at 430 nm using a UV microplate reader (SpectraMax Gemini; Molecular Devices, Sunnyvale, CA). The DS% of HA with DFO was determined by quantitating respective HA-DFO-generated ferrioxamine species with the calibration curve of the ferrioxamine standard solutions prepared from unmodified DFO.

2.5 Fourier Transform Infrared Spectroscopy (FTIR)

FTIR spectra of 2 mg of chelating materials and iron complexes were recorded on an IRAffinity-1 FTIR (Shimadzu Scientific Instruments, KS). For each spectrum, 100 scans were collected between 500 and 4000 cm^{-1} at a resolution of 1 cm^{-1}.

2.6 Determination of relative binding affinity for iron

The binding affinity of DFO and HA-DFO for Fe (III) was determined using a competitive spectrophotometric assay reported by Poreddy et al., [35]. In brief, 1-mM $FeCl_3$ in 1-mM HCl solution was added into the same volume of 10-mM 8-hydroxyquinoline-5-sulfonic acid (sodium sulfoxine) in 20-mM PIPES, and then the mixture was diluted with 20-mM PIPES (pH 7.0) to obtain a sodium (600 μM)-iron (III) (60 μM) solution. Freshly prepared 1-mM DFO (15 μL) or 1-mM HA-DFO conjugates (on DFO basis) (15 μL) was added into the sulfoxine-Fe (III) solution, followed by gentle shaking on an orbital shaker (Madell Technology Corp, Ontario, CA) for 16 h at ambient temperature. The absorbances at 570 nm of resultant solutions were measured on a UV microplate reader (SpectraMax Gemini; Molecular Devices, Sunnyvale, CA). A solution consisting of ddH_2O instead of

DFO/HA-DFO served as a negative control. The percentage of Fe (III) stripped by the DFO-containing solutions from the sulfoxine-Fe (III) was calculated using the equation:

$$\text{Fe (III) Stripped\%} = [A_0 - A_t]/[A0] \times 100\%$$

A_0: Absorbance of negative control at 570 nm

A_t: Absorbance of test solution at 570 nm

2.7 *In vitro* release of DFO from the HA-DFO conjugates

The evaluation of *in vitro* DFO release from the HA-DFO conjugates was carried out in 4 L of phosphate buffered saline (PBS) (pH 7.4, 10 mM) at 37 °C and stirring at 250 rpm. Solutions of free DFO solutions or HA-DFO conjugates were transferred into a dialysis bag (SnakeSkinTM, MWCO: 10 KDa) (Thermo Scientific Inc., Rockfor, IL). The release medium was replaced with fresh PBS every 4 h to maintain the sink condition. At predetermined time points, a 60-μL solution was sampled and mixed with 3 mM of $FeCl_3$ (1:1 v/v). The amounts of DFO left in the solutions were quantified according to section 2.4.

2.8 *In vitro* evaluation of Iron (III)-retention capacity of the HA-DFO conjugates

The evaluation of Iron (III)-retention capacity of the HA-DFO conjugates was carried out in 4 L of phosphate buffered saline (PBS) (pH 7.4, 10 mM) at 37 °C and stirring at 250 rpm. To spectrophotometrically quantify the amount of remained DFO in the samples, Fe (III) chelate complex with free DFO, HA/DFO mixture or HA-DFO was first prepared according to the procedures described in section 2.4, and then transferred into a dialysis bag (SnakeSkinTM, MWCO: 10 KDa) (Thermo Scientific Inc., Rockfor, IL). The release medium was replaced with fresh PBS every 4 h to maintain the sink condition. A 60-μL solution was sampled in predetermined time points, and the DFO-Fe (III) chelate complex left in the solution was quantified according to section 2.4.

2.9 *In vitro* cytotoxicity of HA-DFO in normal cells

The cytotoxicity of DFO and HA-DFO to a normal human cell line was evaluated using a cell growth inhibition assay in HUVECs cultured in EGMTM Complete Medium supplemented with human Epidermal Growth Factor, hydrocortisone, bovine brain extract, ascorbic acid, fetal bovine serum, and Gentamicin/Amphotericin-B. HUVECs were grown in 96-well plates at 3,000 cells/well (n=3 plates, 12 wells/concentration). After a 16-h incubation, DFO, HA-215kDa-DFO or HA-752kDa-DFO dissolved in PBS were added to each

well with final concentrations ranging from 0.01 μM to 100 μM. Subsequently, a resazurin-based colorimetric assay was performed to quantify viability of cell cultures at 72 h post-treatment [50].

2.10 *In vitro* enzymatic degradation

The kinetics of enzymatic degradation of HA was studied by monitoring the molecular weight change. First, 2 mg/mL of unmodified HA or HA-DFO conjugate solutions were prepared in 4 mL of PBS (10 mM, pH7.4), and then hyaluronidase solution (0.35 mg/mL) was added into the reaction system. While the mixture was incubated at 37 °C, the molecular weights of 100- μL aliquots of the samples were monitored by gel-permeation chromatography (GPC) at 25 °C on a Shimadzu 2010CHT with a refractive index detector (RID-10A, Shimadzu Scientific Instruments, KS), using a Shodex OHpak SB-806 HQ column (Showa Denko America, Inc., New York, NY) with 5-mM ammonium acetate as the mobile phase at a flow rate of 0.8 mL/min.

2.11 Preliminary animal experiments

Three groups of rats (controls, DFO, HA-DFO conjugates; n = 5 for each group) underwent surgical external fixation and subsequent distraction. During the distraction stage, the experimental deferoxamine group was treated with twice weekly injections into the distraction gap compared to single dose application of a lyophilized HA-DFO conjugates. After 21 days of consolidation, mandibles were harvested and prepared for histologic analysis.

2.12 Statistical analyses

Summarized values from multiple measurements are expressed as mean ± standard deviation. Statistical analyses were performed using GraphPad Prism 6 software with a significance threshold setting of P= 0.05. Student's *t*-tests were applied to analyze the iron-binding affinity, and a two-way ANOVA analysis was conducted for comparing cell viability and the molecular weight of enzyme-catalyzed hydrolysis products.

3. Results

3.1 Synthesis and quantification of HA-DFO conjugates

The primary amine group of DFO was covalently conjugated to the carboxylic acid groups of the HA backbone using a modified EDC/sulfo-NHS coupling chemistry. The chemical structures of purified HA-DFO conjugates were characterized with ^{1}H-NMR spectra. The successful conjugation was confirmed by the presence of the characteristic peaks of DFO and HA in their ^{1}H-NMR spectra (Figure 2) and a significant change in chemical shift of the methyl group, f, from 2.71 ppm in the spectrum of DFO to 2.82 in spectra of HA-215kDa-DFO and HA-752kDa-DFO.

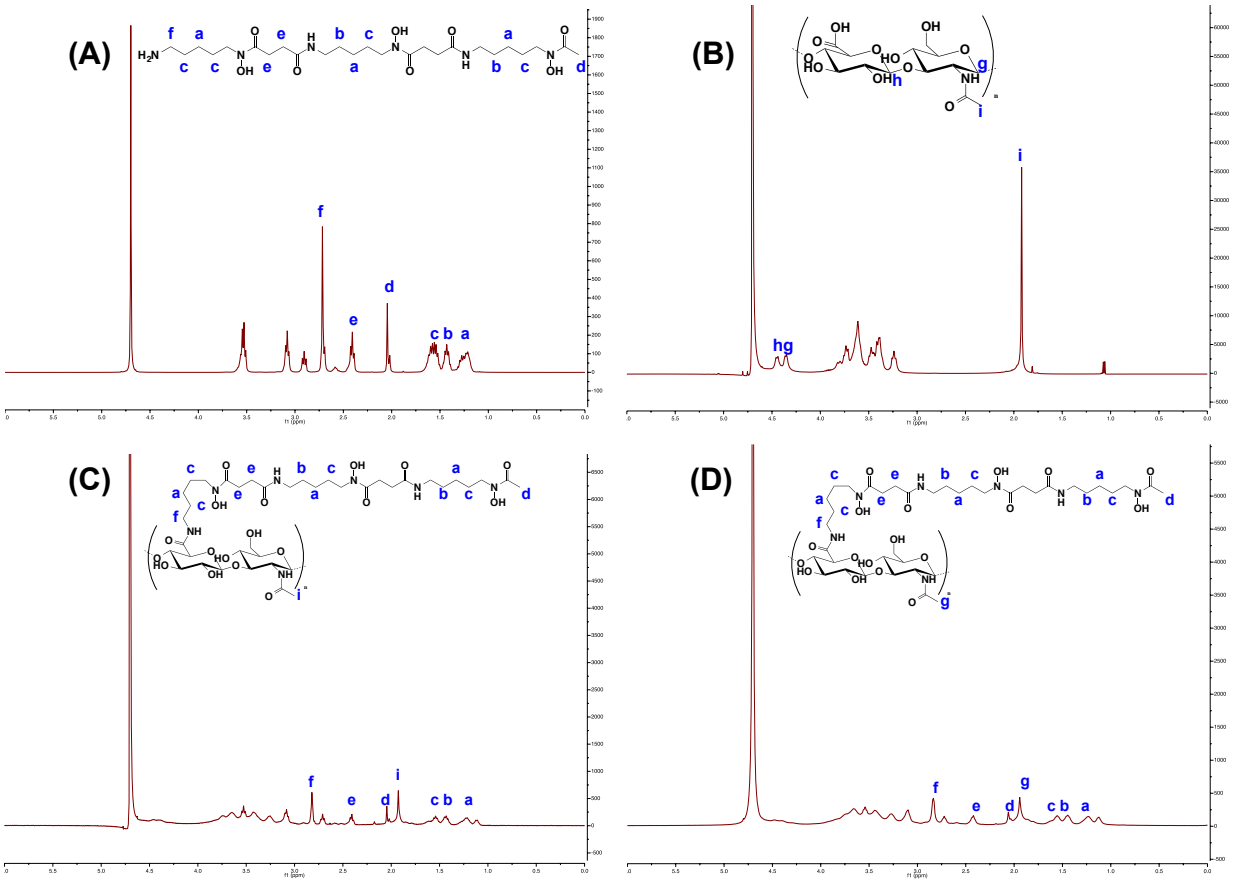

Figure 2. ^{1}H-NMR spectra (D_2O, 400 MHz) of (A) DFO, (B) HA, (C) HA-215kDa-DFO, (D) HA-752kDa-DFO. The peak at $\delta = 4.70$ in each spectrum corresponds to the solvent residue.

Deferoxamine has a high binding affinity ($K_d \approx 10^{-30}$ M) [51, 52] for ferric ions to form a light-amber ferric chelate, ferroxiamine, with a maximum absorption at 430 nm. Upon chelating with ferric iron, both unmodified DFO and HA-DFO conjugates exhibited stronger absorption at 430 nm compared with the iron-free forms (Figure 3A and B). The DS % of the DFO to HA backbones was observed to be molecular weight-dependent and it was found to be 12.59 ± 1.85 % (wt. %) and 9.60 ± 0.28 % (wt.%) for HA-215kDa-DFO and HA-752kDa-DFO, respectively. Such a difference in DS% was probably due to the higher accessibility of the reactive groups in the relatively less viscous HA-215kDa.

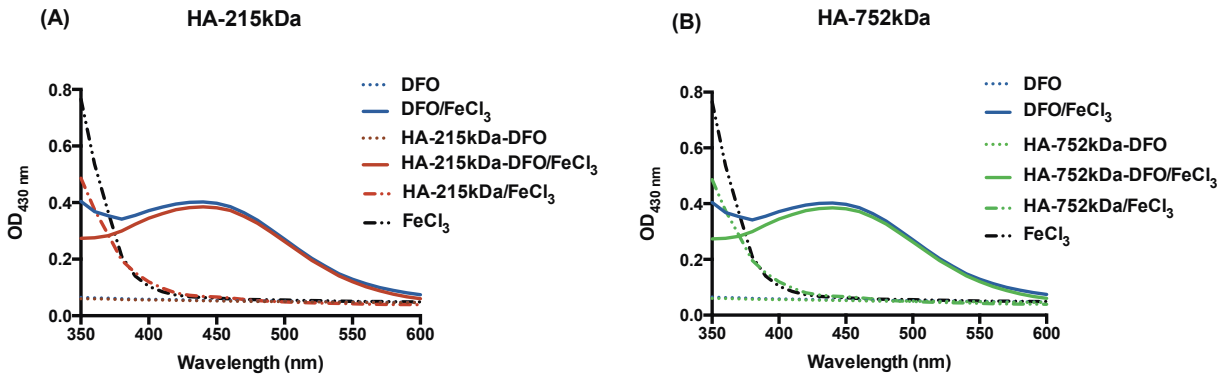

Figure 3. UV-Visible spectra of aqueous solution of Fe (III)-DFO (0.6 mg/mL), Fe (III)-HA-215kDa-DFO (3.0 mg/mL). The spectra of $FeCl_3$ (3mM), DFO (0.6 mg/mL), HA-215kDa-DFO (3.0 mg/mL) and the mixture of $FeCl_3$ with HA-215kDa were also shown for comparison.

3.2 Characterization of HA-DFO conjugates

FTIR spectroscopy was performed to study the effect of the iron chelation on the structural changes of deferoxamine. Figure 4 and 5 show the FT-IR spectra of the unmodified DFO, the unmodified HA, HA-215kDa-DFO and the lyophilized ferrioxamine prepared from DFO or HA-DFO conjugates in the region of 4000 to 400 cm^{-1}. The FTIR spectrum of DFO was collected and compared with its iron-chelated form, ferrrioxamine. Distinct spectrum changes at 3500-2900 cm^{-1} and 1700-1500 cm^{-1} ranges revealed structural differences between deferoxamine and ferrrioxamine as a consequence of the involvements of the hydroxaminc groups during iron chelating. As shown in the Figure 4, the sharp band at 3307 cm^{-1} (assigned as the N-H of the secondary amide group) in DFO decreased and shifted to 3269 cm^{-1}, forming a broad peak in ferrrioxamine due to the prominent effect of iron-chelation. Moreover, the wide peak at 3095 cm^{-1} (assigned as C-NH overtone of the secondary amide group) observed in DFO disappeared in the ferrioxamine , in which a small sharp peak at 3080 cm^{-1} corresponds to the assignment of C-NH overtone instead. In the lower frequency range, the stretching band of carbonyl group in hydroxamate shifted from 1622 cm^{-1} in DFO to 1606 cm^{-1} in the DFO-Iron (III) complex , indicating the metal-oxygen atoms binding. These results are in great agreement with

observations in other spectral analysis of DFO and its chelated form, ferrioxamine, using the Thermal-FTIR [53].

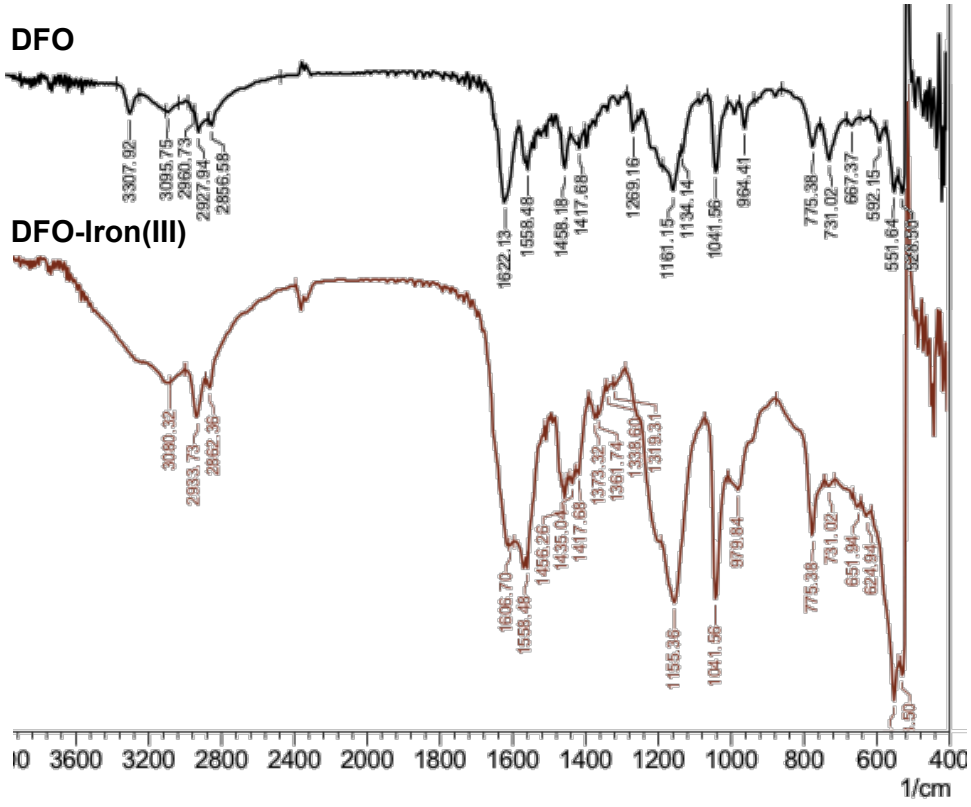

Figure 4. FT-IR spectra of unmodified deferoxamine, and DFO-Iron (III) chelate.

As shown in the Figure 5, the FTIR spectra of the unmodified HA (215 kDa and 752 kDa) and DFO overlapped to great extent at 3600-2800 cm^{-1} and 1650-1000 cm^{-1} intervals, as both compounds share multiple functional groups. However, the broad band around 3273 cm^{-1} can be exclusively assigned to hydrogen-bonded O-H and N-H stretching in the HA backbone. The sharp peaks at 1614 cm^{-1} and 1411 cm^{-1} result from the asymmetric C=O stretching and symmetric C-O stretching of the amide groups [54, 55] of the native HA, respectively. The FTIR spectrum of the HA-DFO conjugates resolved the characteristic peaks of DFO at 2920 cm^{-1} and 2850 cm^{-1}, and 1151 cm^{-1} and peaks of HA-215kDa at 3273 cm^{-1}, 1076 cm^{-1}, and 1039 cm^{-1}, resulting from the successful conjugation of DFO to HA. Compared with the FTIR spectra of HA-DFO conjugates, significant peak shifts were observed in the spectra of HA-DFO-Fe (III) chelates prepared from both HA-215kDa-DFO and HA-752-DFO conjugates. As the peak shifting upon iron chelation mostly occurred in the highly overlapped region, it is very difficult to accurately assign peaks.

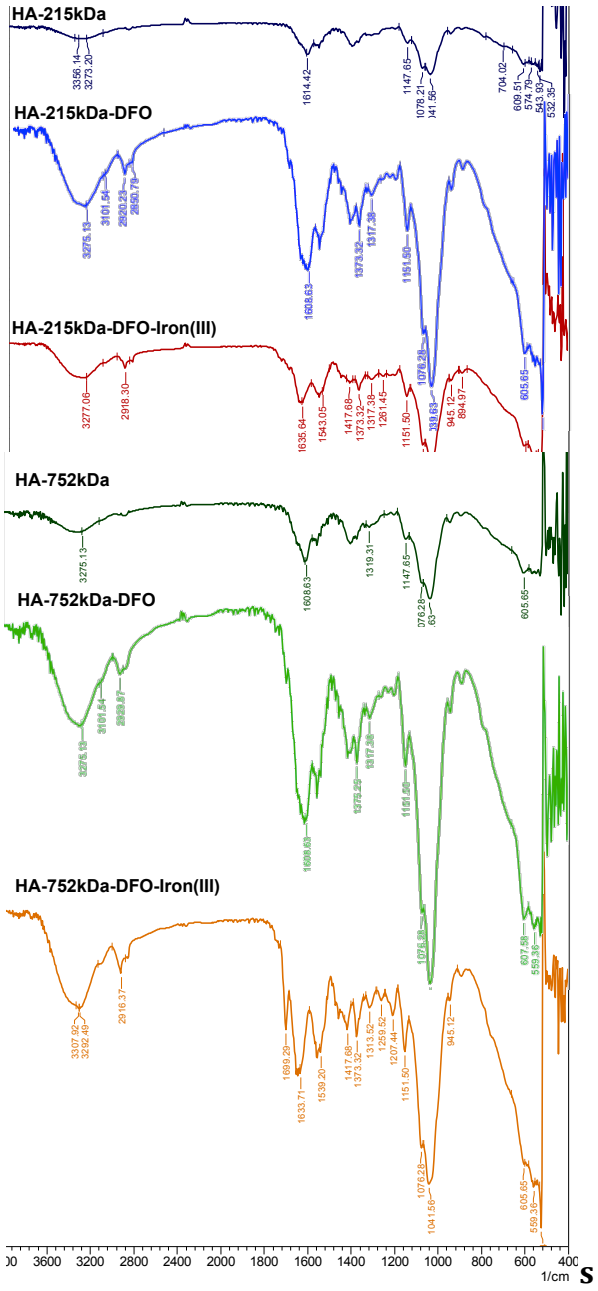

Figure 5. FT-IR spectra of HA-215kDa, HA-215kDa-DFO, HA-215kDa-DFO-Iron (III) chelate, HA-752kDa, HA-752kDa-DFO and HA-752kDa-DFO-Iron (III) chelate.

3.3 Effect of polymer-conjugation of DFO on binding affinity for Ferric Ion

The iron-chelating properties of unmodified DFO and HA-DFO conjugates were assessed using a competitive iron-binding experiment. A solution of sulfoxine was first mixed with $FeCl_3$ to form a sulfoxine-iron (III) complex (λ_{max} = 570 nm). The subsequent addition of the DFO or HA-DFO displaced the sulfoxine to form a chelator-ferric ion complex that had weak absorbance at 570 nm. The reaction mixture was incubated at ambient temperature for 16 h to strip chelated iron. As a result, the reduced absorption at 570 nm is proportional to the iron affinity of chelator, and can be readily read out on a 96-well microplate spectrophotometer. The structural modification to DFO via conjugation to the high molecular weight HA was found to reduce iron-chelating capabilities (Figure 6). Compared to unmodified DFO, HA-215kDa-DFO and HA-752kDa-DFO retained 94.34 % and 84.30% iron-binding capacity, respectively.

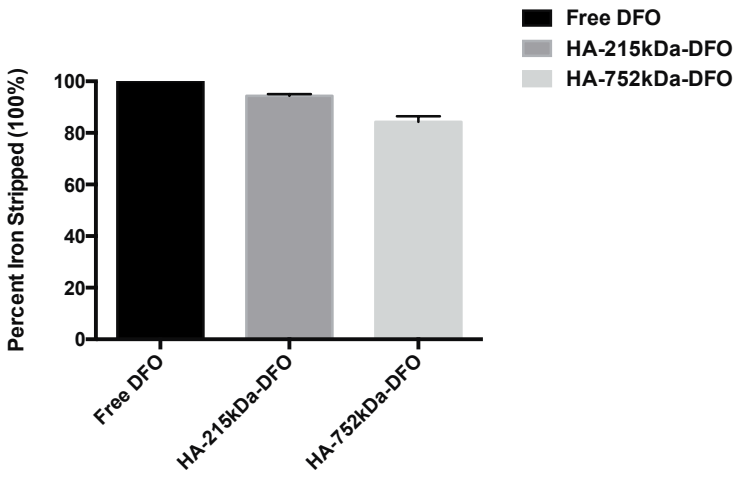

Figure 6. Measurment of iron-binding affinities of unmodified deferoxamine, HA-215kDa-DFO and HA-752kDa-DFO (Mean ± SD; N=3).

3.4 *In vitro* evaluation of Iron (III)-retention capacity of the HA-DFO conjugates

The release profiles of free DFO and HA-DFO conjugates are shown in Figure 7, and their release kinetics were fitted using a first-order model. The release half-lives of free DFO, is 0.5 h. Compared with the unmodified DFO samples, sustained release of the DFO were observed for the HA-DFO conjugates. The remained percentages of DFO in the HA-215kDa-DFO and HA-752kDa-DFO were 78% and 81% after two-day dialysis, respectively, due to the stable amide bonds formed between the drug molecules and the HA backbones.

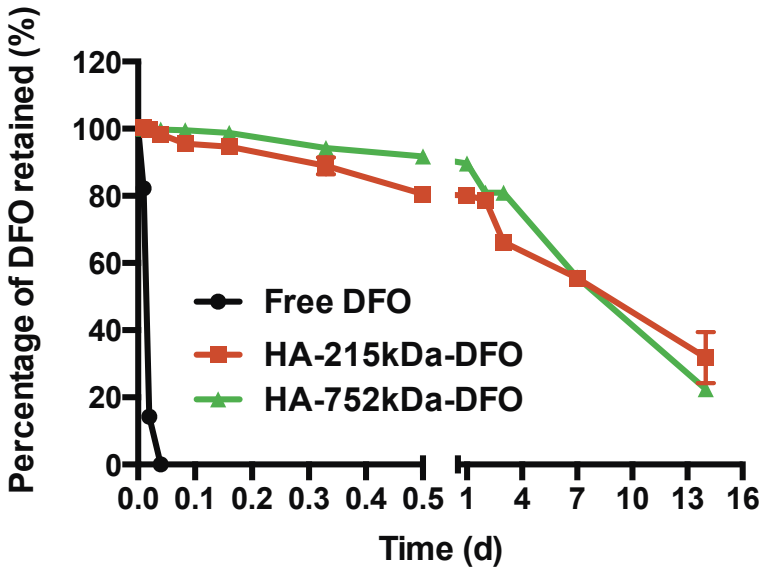

Figure 7. *In vitro* release profiles of deferoxamine, HA-215kDa-DFO and HA-752kDa-DFO in PBS at 37 °C (Mean ± SD; N=3).

3.5 *In vitro* evaluation of Iron (III)-retention capacity of the HA-DFO conjugates

The release profiles of DFO, HA/DFO mixture and HA-DFO conjugates in the Fe (III)-chelated forms are shown in Figure 8. The Fe (III) chelate complexes with unmodified DFO and HA/DFO mixture were not retained in the dialysis bag, and their release kinetics were fitted using a first-order model with release half-lives of 0.52 h and 0.64 h, respectively. In comparison, a biphasic release pattern was shown in the release kinetics profiles of HA-DFO conjugates with an initial burst release of approximately 20% of the loading dose within 1 h, probably due to the release of the complex on the surface of HA-DFO conjugate nanparticles. Thereafter, sustained release with half-lives of 4.35 d and 14.17 d were observed for HA-215kDa-DFO and HA-752kDa-DFO, respectively.

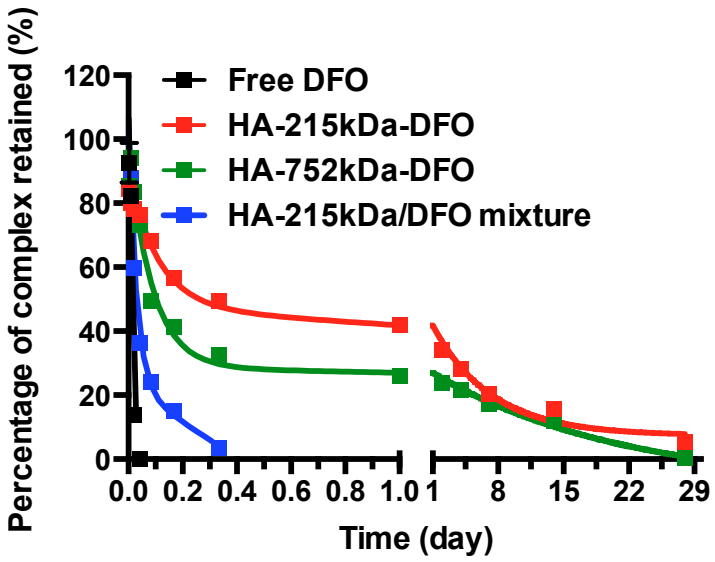

Figure 8. *In vitro* release profiles of Fe (III) chelate complexes prepared from deferoxamine, HA-215kDa-DFO and HA-752kDa-DFO in PBS at 37 °C (Mean ± SD; N=3).

3.6 *In vitro* cytotoxicity of HA-DFO in normal HUVEC cells

The cell viability tests in the presence of free DFO or HA-DFO conjugates demonstrated a concentration-dependent cytotoxicity to HUVECs (Figure 9). The free DFO was significantly more toxic to the HUVECs from 5-50 μM, compared with the HA-DFO conjugates. Particularly, after incubating the cells with either free DFO for 72 h, the cell viability was approximately 79.38 % at 5 μM, and it decreased to 52.79% at a DFO concentration of 50 μM. At the equivalent HA-DFO dose range, however, the survival rates of cells treated with HA-215kDa-DFO were 1.14 - 1.53 fold higher than that of the free DFO-treated cells. Similar increased cell viability was observed in the HA-752kDa-DFO group, and the apparent toxic effects of both two HA-DFO conjugates could only be observed at high DFO concentration above 50 μM.

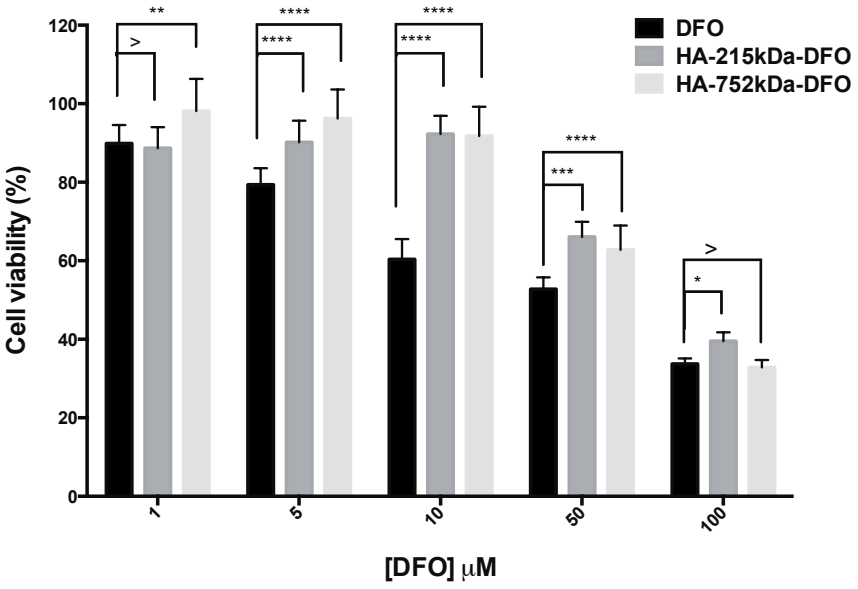

Figure 9. Cell viability assay of deferoxamine and two HA-DFO conjugates in normal HUVEC cells (Mean ± SD; N=3; *$p < 0.05$).

3.7 *In vitro* enzymatic degradation

The effects of hyaluronidase on the molecular weight of unmodified HA and HA-DFO conjugates are shown in Figure 10. The molecular weights of both unmodified HA and HA-DFO conjugates decreased within 1 h to less than 10% of their initial molecular weights and to approximately 5% as the incubation proceeded. No significant difference in the enzyme-catalyzed hydrolysis degree was found between unmodified HA and the HA-DFO conjugates. Moreover, by the end of the incubation at 72h, the retained molecular weight of the unmodified HA-215kDa, HA-215kDa-DFO, HA-752kDa and HA-752kDa-DFO were 7.83%, 7.82%, 8.23% and 6.63%, respectively. These findings established that chemical modification of the HA with DFO did not affect the biodegradability of HA in simulated physiological environments.

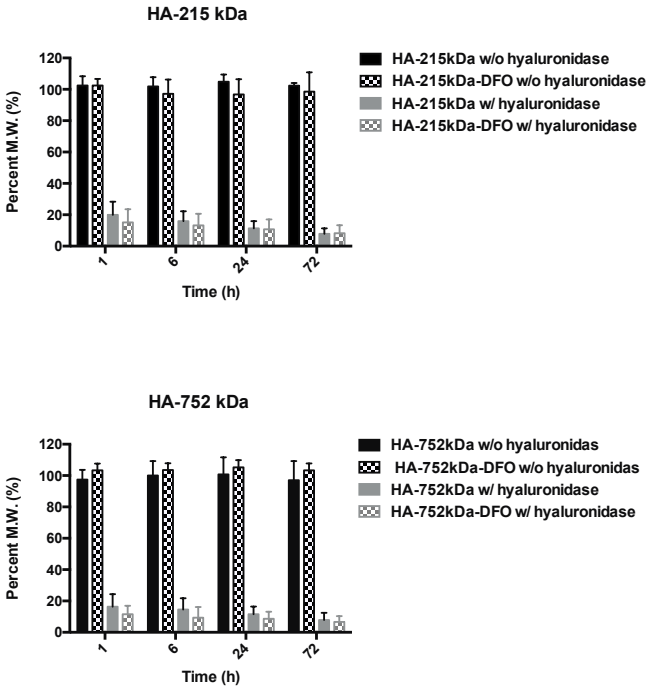

Figure 10. Comparison of the enzymatic hydrolysis of unmodified HA and HA-DFO conjugates by GPC measurement in PBS (10 mM, pH7.4) at 37 °C with and without hyaluronidases. (Mean ± SD; N=3; $^{*}p < 0.05$).

3. 8 Preliminary animal experiments

A proliferation of osteocytes was observed in both the HA-DFO conjugate and DFO-treated groups when compared with the regenerate of the control group. Deferoxamine affected a significant increase in osteocytes and an increase in bone volume fraction, with subsequent decreased osteoid volume fraction. The data also demonstrated no significant difference in empty lacunae. After 3 weeks, the mice treated with the HA-DFO conjugates had slightly faster proliferation of osteocytes than the standard DFO injection group.

4. Discussion

Our motivation to design a macromolecular DFO complex using HA stems from its inherent biocompatibility, its exceptional viscoelastic and its therapeutic properties in the treatment of arthritis and wound healing. The relatively simple chemical structure of HA allows us to perform further modifications to create versatile drug carriers with controlled release profiles. Chemical modifications of HA generally focus on four structural sites, including the reducing end, N-acetyl groups, hydroxyl groups, and carboxylic acid groups. Carbodiimide-mediated conjugations using EDC to couple HA to primary amine-containing molecules have been reported to result in low reaction yields [56, 57], which may be

caused by a fast formation of a stable N-acylurea adducts from O➔N rearrangement [57, 58]. Cross-linking strategies that require first forming modified HA with a variety of functional groups, such as thiol [59, 60], sym-collidine [61] and adipic acid dihydrazide [62, 63], on the other hand, have been shown to effectively graft poorly water soluble therapeutic agents to the carboxylic acid groups of HA. However, alterations physical characteristics of HA, such as decreased solubility or receptor-recognition, have been associated with the cross-linking method. Alternative carbodiimide-catalyzed approaches include reacting the primary amine group with the carboxyl group on HA using hydroxybenzotriazole or N-hydroxysuccinimide in an organic solvent/water mixture to prevent the O➔N rearrangement [64, 65]. In this study, we used a two-step approach for HA-DFO conjugation, which relies on first forming the tetrabutylammonium salt of hyaluronic acid (HA-TBA). HA-TBA posses excellent DMSO-solubility and thus remarkably stabilize the HA-NHS active ester during the HA-DFO conjugation reaction performed in DMSO, resulting in the facile grafting DFO to HA backbones without generating the N-acylurea adduct.

Deferoxamine consists of an aliphatic chain, two secondary amide groups, and three bidentate hydroxamic groups; the last component serves as a chelator for trivalent iron. Upon iron binding, the hydroxyl groups deprotonate and tform a stable octahedral complex

with three asymmetrical chelation rings around ferric iron. To verify that the binding behavior of DFO molecules was not altered after being immobilized to the high molecular weight HA, the spectra properties of the HA-DFO-Fe (III) complex was recorded and compared with that of the DFO-Fe (III) complex. Indeed, the virtually identical spectra profiles in the characteristic absorption region revealed that the HA-DFO conjugate chelated to the ferric ions in a similar manner as the free DFO molecules.

Compared with the unmodified DFO molecules, HA-DFO conjugate exhibited decreased iron-binding capability, which was probably caused by restricted movements and spatial arrangement of the hydroxamic groups on the DFO. Poreddy et al., [66] synthesized several libraries of structural DFO analogues that had modifications on the spacer and the C-terminal. They also prepared a number of DFO variants of non-amide, reverse-amide, or hybrid. Compared with the unmodified DFO, two thirds of these DFO analogues remain varying and relatively low binding affinities from 17% to 62%. In comparison, both HA-DFO conjugates made using our synthetic approach retained much higher iron-binding affinities, which were at least 84% of the unmodified DFO (Figure 5). Such improved iron-binding affinity observed in the present study was achieved by modifying the terminal amino group in DFO, which is located five methylene groups away from the nearest iron-binding hydroxamic groups.

The development of high-molecular-weight DFO-polymer conjugates has been suggested as an efficient approach for extending the retention of the DFO and sparing the rapid clearance of the chelator. In some cases, the DFO is covalently attached to biocompatible polymers such as polysaccharide (e.g. dextran and hydroxyethyl-starch) via a reductive amination [35] and poly (ethylene glycol) [36] through an amide linkage. These polymer-based macromolecular DFO retained the iron-binding properties and exhibited significantly reduced cytotoxicity in normal cells. In the present study, we observed that the hyaluronan derivatives of the DFO exhibited significantly prolonged release profiles in the simulated physiological medium compared with the free DFO, due to the stable amide bond between the DFO and the HA backbone. Therefore, the HA-DFO conjugate could provide an enhanced therapeutic index and maintain the effective drug levels in the region of interest after a local injection, ultimately averting the undesired systemic toxicity through reducing the necessary drug dose.

Deferoxamine is known for its acute [14-16] and chronic [67] toxicity, seriously diminishing its clinical values. The DFO-induced cytotoxicity has been previously reported in human neuroblastoma cells and astrocytoma cells, and two mechanisms of the DFO toxicity have been proposed [68, 69]. Becton et al., suggested that cytotoxicity of the DFO was related to its strong iron-binding affinity, leading to a cytosolic iron deficiency [68].

Lee et al., on the other hand, implicated an oxidation process producing hydroxyl radicals that leads to DFO cytotoxicity [69]. Conjugation of DFO to a large, biocompatible polymer such as dextran [35] or poly (ethylene glycol) [36] has been reported to efficiently reduce its toxicity. Our cell viability results are in consistent with these previous observations, and the lower toxicity of the HA-DFO conjugate may be attributed to its different cellular internalization pathways. HA-based nanoconjugates are mainly internalized by the CD44-expressing cells by an active transport mechanism via the HA receptors-CD44 in conjunction with a clathrin-dependent endocytic pathway [70, 71]. As HUVEC cells overexpress CD44H on the cell membrane [72], we hypothesize that HA-DFO molecules first bound to its surface receptor, CD44H, on the membrane of the HUVEC cells, and then were translocated into cells in a vesicular form. The internalized vesicles loaded with HA-DFO may fuse with endosomes for degradation or further delivery into other subcellular compartments, such as Golgi network or endoplasmic reticulum. We conjecture that the unique celluar internalization pathway of the HA-DFO may delay or reduce the cytosolic exposure of active DFO molecules, thus diminishing its cytotoxicity. On the other hand, Rossi et al. [36] proposed that the reduced toxicity of the polymer-based DFO to the HUVEC cells probably resulted from its lack of capability to permeate the cell membrane. The exact mechanism for the decreased cytotoxicity of the HA-DFO conjugates remains to be fully

elucidated by further investigation with the microscopy of living-cell labeled with fluorescent antibodies.

The *in vivo* degradation of HA is controlled by three types of enzymes, including two exoglycosidases (β-glucuronidase and β-N-acetyl glucosaminidase) and an endoglycosidase, hyaluronidase, which acts collaboratively with the first two. During this course, the HA backbone is enzymatically cleaved by hyaluronidases at β-N-acetylhexosamine-[1→4] glycosidic bonds into smaller oligosaccharides [73], followed by further degradations with the exoglycosidases for clearance through multiple metabolic pathways [74, 75]. Botzki et al., [76] has proposed an acid/base reaction mechanism for the hydrolysis of HA by testes-type hyaluronidases. The Glu-149 residue of hyaluronidase is a proton donor, while the N-acetyl carbonyl group of the HA acts as a nucleophile to form a inter-molecule covalent oxazolinium intermediate, which is later hydrolyzed by water molecule. HA derivatives prepared by full esterification of carboxylic groups in D-glucoronic acid unit have been found to result in delayed degradation by the testicular hyaluronidase [77], which was believed to caused by the restricted cleavage of β (1→4) glycoside bonds. Based on our results, HA-DFO conjugationes with partially modified carboxylic acid groups did not compromise the susceptibility of HA to the enzymatic

hydrolysis, consistent with what other research groups found with thiolated HA (1.32 wt.%) [60].

Distraction osteogenesis is a powerful reconstructive technique for bone growth and repair. An angiogenic means of enhancing the efficacy of this metabolically demanding procedure would be beneficial in expanding its therapeutic potential. We posit that the angiogenic effect of deferoxamine, an iron chelator that has been shown to increase angiogenesis, will improve bone regeneration by means of augmentations in quality and quantity of bone and bone-producing cells. Although no statistically significant difference was observed, mice treated with one time application of lyophilized HA-DFO conjugates showed faster proliferation rate of osteocytes than the mice treated with twice-weekly injections of DFO. Moreover, only one dose of the HA-DFO conjugate was determined sufficient to stimulate the proliferation osteocytes, which makes it a promising candidate as a translational medicine.

5. Conclusions

In this study, we synthesized a novel HA-based iron chelator using TBA modified HA for the facile amidation in an organic solvent to prevent the side reactions, and the

resultant HA-DFO conjugates retained high iron-binding capability. Compared with the free DFO-Fe (III) complex, the complexes prepared using the HA-DFO conjugates exhibited sustained release profiles in the physiological environments attributed to the stable amide bond, thus limiting body exposure to the toxic free DFO molecules. We also observed significantly decreased cytotoxicity to normal cells and excellent biodegradability of the HA-DFO conjugates. Collectively, these attractive properties render HA-DFO conjugate a potential candidate to promote pathologic fracture healing and bone regeneration.

6. References

1. Association, A.M., *Physician Characteristics and Distribution in the U.S.* 2014: American Medical Association
2. Garcia-Barros, M., et al., *Tumor response to radiotherapy regulated by endothelial cell apoptosis.* Science, 2003. **300**(5622): p. 1155-9.
3. Imaizumi, N., et al., *Radiotherapy suppresses angiogenesis in mice through TGF-betaRI/ALK5-dependent inhibition of endothelial cell sprouting.* PLoS One, 2010. **5**(6): p. e11084.

4. Fajardo, L.F., *The pathology of ionizing radiation as defined by morphologic patterns.* Acta Oncol, 2005. **44**(1): p. 13-22.

5. Baker, D.G. and R.J. Krochak, *The response of the microvascular system to radiation: a review.* Cancer Invest, 1989. **7**(3): p. 287-94.

6. Hopewell, J.W., *Radiation-therapy effects on bone density.* Med Pediatr Oncol, 2003. **41**(3): p. 208-11.

7. Currey, J.D., et al., *Effects of ionizing radiation on the mechanical properties of human bone.* J Orthop Res, 1997. **15**(1): p. 111-7.

8. Gutteridge, J.M., R. Richmond, and B. Halliwell, *Inhibition of the iron-catalysed formation of hydroxyl radicals from superoxide and of lipid peroxidation by desferrioxamine.* Biochem J, 1979. **184**(2): p. 469-72.

9. Graf, E., et al., *Iron-catalyzed hydroxyl radical formation. Stringent requirement for free iron coordination site.* J Biol Chem, 1984. **259**(6): p. 3620-4.

10. Hebbel, R.P., *Auto-oxidation and a membrane-associated 'Fenton reagent': a possible explanation for development of membrane lesions in sickle erythrocytes.* Clin Haematol, 1985. **14**(1): p. 129-40.

11. Fisher, S.A., et al., *Desferrioxamine mesylate for managing transfusional iron overload in people with transfusion-dependent thalassaemia.* Cochrane Database Syst Rev, 2013. **8**: p. CD004450.

12. Kalinowski, D.S. and D.R. Richardson, *The evolution of iron chelators for the treatment of iron overload disease and cancer.* Pharmacol Rev, 2005. **57**(4): p. 547-83.

13. Bernhardt, P.V., *Coordination chemistry and biology of chelators for the treatment of iron overload disorders.* Dalton Trans, 2007(30): p. 3214-20.

14. Westlin, W.F., *Deferoxamine in the treatment of acute iron poisoning. Clinical experiences with 172 children.* Clin Pediatr (Phila), 1966. **5**(9): p. 531-5.

15. Whitten, C.F., et al., *Studies in acute iron poisoning. I. Desferrioxamine in the treatment of acute iron poisoning: clinical observations, experimental studies, and theoretical considerations.* Pediatrics, 1965. **36**(3): p. 322-35.

16. Whitten, C.F., Y.C. Chen, and G.W. Gibson, *Studies in acute iron poisoning. II. Further observations on desferrioxamine in the treatment of acute experimental iron poisoning.* Pediatrics, 1966. **38**(1): p. 102-10.

17. Cohen, A. and E. Schwartz, *Iron chelation therapy with deferoxamine in Cooley anemia.* J Pediatr, 1978. **92**(4): p. 643-7.

18. Propper, R.D., et al., *Continuous subcutaenous administration of deferoxamine in patients with iron overload.* N Engl J Med, 1977. **297**(8): p. 418-23.

19. Fang, T.D., et al., *Angiogenesis is required for successful bone induction during distraction osteogenesis.* J Bone Miner Res, 2005. **20**(7): p. 1114-24.

20. Wan, C., et al., *Activation of the hypoxia-inducible factor-1alpha pathway accelerates bone regeneration.* Proc Natl Acad Sci U S A, 2008. **105**(2): p. 686-91.

21. Shen, X., et al., *Prolyl hydroxylase inhibitors increase neoangiogenesis and callus formation following femur fracture in mice.* J Orthop Res, 2009. **27**(10): p. 1298-305.

22. Wang, Y., et al., *The hypoxia-inducible factor alpha pathway couples angiogenesis to osteogenesis during skeletal development.* J Clin Invest, 2007. **117**(6): p. 1616-26.

23. Farberg, A.S., et al., *Deferoxamine reverses radiation induced hypovascularity during bone regeneration and repair in the murine mandible.* Bone, 2012. **50**(5): p. 1184-7.

24. Donneys, A., et al., *Deferoxamine restores callus size, mineralization, and mechanical strength in fracture healing after radiotherapy.* Plast Reconstr Surg, 2013. **131**(5): p. 711e-9e.

25. Donneys, A., et al., *Localized deferoxamine injection augments vascularity and improves bony union in pathologic fracture healing after radiotherapy.* Bone, 2013. **52**(1): p. 318-25.

26. Hamilton, K.O., et al., *The transport of two iron chelators, desferrioxamine B and L1, across Caco-2 monolayers.* Br J Haematol, 1994. **86**(4): p. 851-7.

27. Ihnat, P.M., J.L. Vennerstrom, and D.H. Robinson, *Synthesis and solution properties of deferoxamine amides.* J Pharm Sci, 2000. **89**(12): p. 1525-36.

28. Bergeron, R.J. and G.M. Brittenham, *The Development of iron chelators for clinical use*. 1994, Boca Raton: CRC Press. xiii, 416 p.

29. Summers, M.R., et al., *Studies in desferrioxamine and ferrioxamine metabolism in normal and iron-loaded subjects.* Br J Haematol, 1979. **42**(4): p. 547-55.

30. Freedman, M.H., et al., *Neurotoxicity associated with deferoxamine therapy.* Toxicology, 1988. **49**(2-3): p. 283-90.

31. Davies, S.C., et al., *Ocular toxicity of high-dose intravenous desferrioxamine.* Lancet, 1983. **2**(8343): p. 181-4.

32. Porter, J.B. and E.R. Huehns, *The toxic effects of desferrioxamine.* Baillieres Clin Haematol, 1989. **2**(2): p. 459-74.

33. Toliyat, T., M. Jorjani, and Z. Khorasanirad, *An extended-release formulation of desferrioxamine for subcutaneous administration.* Drug Deliv, 2009. **16**(7): p. 416-21.

34. Toliyat, T.K., Zeinab, *Development of a depofoam technology for the sustained delivery of desferrioxamine mesylate.* Daru, 2003. **11**(3): p. 88-94.

35. Hallaway, P.E., et al., *Modulation of deferoxamine toxicity and clearance by covalent attachment to biocompatible polymers.* Proc Natl Acad Sci U S A, 1989. **86**(24): p. 10108-12.

36. Rossi, N.A., et al., *In vitro chelating, cytotoxicity, and blood compatibility of degradable poly(ethylene glycol)-based macromolecular iron chelators.* Biomaterials, 2009. **30**(4): p. 638-48.

37. Dragsten, P.R., et al., *First human studies with a high-molecular-weight iron chelator.* J Lab Clin Med, 2000. **135**(1): p. 57-65.

38. Harmatz, P., et al., *Phase Ib clinical trial of starch-conjugated deferoxamine (40SD02): a novel long-acting iron chelator.* Br J Haematol, 2007. **138**(3): p. 374-81.

39. Knudson, C.B. and W. Knudson, *Hyaluronan-binding proteins in development, tissue homeostasis, and disease.* FASEB J, 1993. **7**(13): p. 1233-41.

40. Laurent, T.C. and J.R.E. Fraser, *Hyaluronan.* FASEB J, 1992. **6**(7): p. 2397-2404.

41. Prestwich, G.D., *Hyaluronic acid-based clinical biomaterials derived for cell and molecule delivery in regenerative medicine.* J Control Release, 2011. **155**(2): p. 193-9.

42. Park, J.K., et al., *Guided bone regeneration by poly(lactic-co-glycolic acid) grafted hyaluronic acid bi-layer films for periodontal barrier applications.* Acta Biomater, 2009. **5**(9): p. 3394-403.

43. Goldberg, V.M. and J.A. Buckwalter, *Hyaluronans in the treatment of osteoarthritis of the knee: evidence for disease-modifying activity.* Osteoarthritis Cartilage, 2005. **13**(3): p. 216-24.

44. Hiraoka, N., et al., *Intra-articular injection of hyaluronan restores the aberrant expression of matrix metalloproteinase-13 in osteoarthritic subchondral bone.* J Orthop Res, 2011. **29**(3): p. 354-60.

45. Barbucci, R., et al., *Hyaluronic acid hydrogel in the treatment of osteoarthritis.* Biomaterials, 2002. **23**(23): p. 4503-13.

46. Della Valle, F.R., Aurelio Esters of hyaluronic acid, US4851521 A

47. Gower, J.D., G. Healing, and C.J. Green, *Determination of desferrioxamine-available iron in biological tissues by high-pressure liquid chromatography.* Anal Biochem, 1989. **180**(1): p. 126-30.

48. Guittet, O., et al., *Differential sensitivity of the tyrosyl radical of mouse ribonucleotide reductase to nitric oxide and peroxynitrite.* J Biol Chem, 1998. **273**(34): p. 22136-44.

49. Kraemer, H.J. and H. Breithaupt, *Quantification of desferrioxamine, ferrioxamine and aluminoxamine by post-column derivatization high-performance liquid chromatography. Non-linear calibration resulting from second-order reaction kinetics.* J Chromatogr B Biomed Sci Appl, 1998. **710**(1-2): p. 191-204.

50. Cohen, M.S., et al., *A novel intralymphatic nanocarrier delivery system for cisplatin therapy in breast cancer with improved tumor efficacy and lower systemic toxicity in vivo.* Am J Surg, 2009. **198**(6): p. 781-6.

51. Keberle, H., *The Biochemistry of Desferrioxamine and Its Relation to Iron Metabolism.* Ann N Y Acad Sci, 1964. **119**: p. 758-68.

52. Fielding, J. and M. Brunstroem, *Estimation of Ferrioxamine and Desferrioxamine in Urine.* J Clin Pathol, 1964. **17**: p. 395-8.

53. Siebner-Freibach, H., et al., *Thermo-FTIR spectroscopic study of the siderophore ferrioxamine B: spectral analysis and stereochemical implications of iron chelation, pH, and temperature.* J Agric Food Chem, 2005. **53**(9): p. 3434-43.

54. Reddy, K.J. and K.T. Karunakaran, *Purification and characterization of hyaluronic acid produced by Streptococcus zooepidemicus strain 3523-7.* J BioSci Biotech, 2013. **2**(3): p. 173-179.

55. Wu, Y., *Preparation of low-molecular-weight hyaluronic acid by ozone treatment.* Carbohydr Polym, 2012. **89**(2): p. 709-12.

56. Ogamo, A., et al., *Preparation and properties of fluorescent glycosaminoglycuronans labeled with 5-aminofluorescein.* Carbohydr Res, 1982. **105**(1): p. 69-85.

57. Kuo, J.W., D.A. Swann, and G.D. Prestwich, *Chemical modification of hyaluronic acid by carbodiimides.* Bioconjug Chem, 1991. **2**(4): p. 232-41.

58. Kurzer, F. and K. Douraghi-Zadeh, *Advances in the chemistry of carbodiimides.* Chem Rev, 1967. **67**(2): p. 107-52.

59. Shu, X.Z., et al., *Disulfide cross-linked hyaluronan hydrogels.* Biomacromolecules, 2002. **3**(6): p. 1304-11.

60. Kafedjiiski, K., et al., *Synthesis and in vitro evaluation of thiolated hyaluronic acid for mucoadhesive drug delivery.* Int J Pharm, 2007. **343**(1-2): p. 48-58.

61. Coradini, D., et al., *Hyaluronic acid as drug delivery for sodium butyrate: improvement of the anti-proliferative activity on a breast-cancer cell line.* Int J Cancer, 1999. **81**(3): p. 411-6.

62. Cai, S., et al., *Localized doxorubicin chemotherapy with a biopolymeric nanocarrier improves survival and reduces toxicity in xenografts of human breast cancer.* J Control Release, 2010. **146**(2): p. 212-8.

63. Luo, Y., M.R. Ziebell, and G.D. Prestwich, *A hyaluronic acid-taxol antitumor bioconjugate targeted to cancer cells.* Biomacromolecules, 2000. **1**(2): p. 208-18.

64. Bulpitt, P. and D. Aeschlimann, *New strategy for chemical modification of hyaluronic acid: preparation of functionalized derivatives and their use in the formation of novel biocompatible hydrogels.* J Biomed Mater Res, 1999. **47**(2): p. 152-69.

65. Zhao, Y., et al., *CD44-tropic polymeric nanocarrier for breast cancer targeted rapamycin chemotherapy.* Nanomedicine, 2014.

66. Poreddy, A.R., et al., *Hydroxamate-based iron chelators: combinatorial syntheses of desferrioxamine B analogues and evaluation of binding affinities.* J Comb Chem, 2004. **6**(2): p. 239-54.

67. Olivieri, N.F., et al., *Visual and auditory neurotoxicity in patients receiving subcutaneous deferoxamine infusions.* N Engl J Med, 1986. **314**(14): p. 869-73.

68. Becton, D.L. and P. Bryles, *Deferoxamine inhibition of human neuroblastoma viability and proliferation.* Cancer Res, 1988. **48**(24 Pt 1): p. 7189-92.

69. Lee, Y.S. and R.D. Wurster, *Deferoxamine-induced cytotoxicity in human neuronal cell lines: protection by free radical scavengers.* Toxicol Lett, 1995. **78**(1): p. 67-71.

70. Contreras-Ruiz, L., et al., *Intracellular trafficking of hyaluronic acid-chitosan oligomer-based nanoparticles in cultured human ocular surface cells.* Mol Vis, 2011. **17**: p. 279-90.

71. Cai, S., et al., *Cellular uptake and internalization of hyaluronan-based doxorubicin and cisplatin conjugates.* J Drug Target, 2014. **22**(7): p. 648-57.

72. Price, E.A., D.R. Coombe, and J.C. Murray, *Endothelial CD44H mediates adhesion of a melanoma cell line to quiescent human endothelial cells in vitro.* Int J Cancer, 1996. **65**(4): p. 513-8.

73. Kreil, G., *Hyaluronidases--a group of neglected enzymes.* Protein Sci, 1995. **4**(9): p. 1666-9.

74. Fraser, J.R., T.C. Laurent, and U.B. Laurent, *Hyaluronan: its nature, distribution, functions and turnover.* J Intern Med, 1997. **242**(1): p. 27-33.

75. Leach, J.B. and C.E. Schmidt, *HYALURONAN*, in *Encyclopedia of Biomaterials and Biomedical Engineering*. p. 1421-1431.

76. Botzki, A., et al., *L-Ascorbic acid 6-hexadecanoate, a potent hyaluronidase inhibitor. X-ray structure and molecular modeling of enzyme-inhibitor complexes.* J Biol Chem, 2004. **279**(44): p. 45990-7.

77. Zhong, S.P., et al., *Biodegradation of hyaluronic acid derivatives by hyaluronidase.* Biomaterials, 1994. **15**(5): p. 359-65.

Chapter 6

In Vivo Efficacy of Nano-hyaluronan-Conjugated Cisplatin for Treatment of Murine Melanoma

1. Introduction

Melanoma is a deadly skin cancer, killing more than 9,000 Americans in 2012. Incidence is rising rapidly, to the point where 1 in 50 Americans will develop melanoma [1]. Stage at diagnosis is the main determinant of survival. While 5-year survival for localized melanoma is 98%, involvement of regional lymph nodes drops survival to 62%, and in distant metastatic disease survival is only 15% [1].

The main reason is that very early disease can generally be successfully treated with simple excision. However, once it has spread to the lymph nodes and beyond, melanoma becomes very hard to treat and survival decreases accordingly. This applies to "locally advanced" melanoma with lymph node involvement as well as widespread metastatic disease. One important reason for this is that melanoma is notoriously resistant to chemotherapy. Conventional chemotherapy does not result in high levels of penetration into tumors or lymph nodes. Therefore efficacy is limited by systemic toxicity. It has long been a goal to increase relative penetration of chemotherapy into tumors and lymph nodes. Here we report the first use of a novel peri--tumor injectable chemotherapy compound in an *in-vivo* murine model for locally advanced melanoma. We seek to answer the question of whether increased peri-tumoral dose translates into a measurable *in-vivo* response.

2. Materials and Methods

2.1 Materials

All chemicals were obtained from commercial suppliers and used without further purification unless otherwise noted. Hyaluronan (HA; 35 kDa) was purchased from Lifecore Biomedical (Chaska, MN) as sodium hyaluronate, which was cultured and produced by a microbial fermentation process. Cisplatin (CDDP) was obtained from AK Scientific (Union, CA). All other chemicals and cell culture supplies were purchased from Sigma-Aldrich Co (St. Louis, MO) or Fisher Scientific (Pittsburgh, PA). Distilled water was used in syntheses, cell culture (sterilized by autoclaving) and animal experiments (sterilized by autoclaving). Human melanoma cell lines A-2058 was were obtained from American Type Culture Collection (ATCC, MA) and cultured according to ATCC protocol.

2.2 Methods

2.2.1 Synthesis of hyaluronan-cisplatin conjugates

HA-Cisplatin (HA-Pt) conjugate was prepared as previously described [2]. Briefly, HA (50 mg) and CDDP (40 mg) were dissolved in a total of 80 mL double distilled water (ddH_2O) and stirred in the dark for 96 hr at ambient temperature (~25°C). By the end of the reaction, the mixture was filtered through a 0.22 μm nylon membrane filter (Fisher Scientific; Pittsburgh, PA), followed by dialysis (MWCO 10,000 Da; Pierce, IL) against ddH_2O for 24 hr in dark with 4 water changes. The crude HA-Pt conjugate was concentrated by evaporation under reduced pressure and then stored at room temperature in dark.

The CDDP substitution degree was determined by an Inductively Coupled Plasma Mass Spectrometry (ICP-MS, Agilent Technologies 7500a) using terbium as internal standard. High purity argon (>99.996%) was used as carrier gas. The calibration concentrations of platinum included 1, 10, 20, 40, and 50 ppb.

2.2.2 Induction of human melanoma xenografts

Human melanoma cell line A-2058 was cultured in Dulbecco's Modified Eagle Medium (DMEM) supplemented with 10% (v/v) fetal bovine serum and 1% (v/v) L-glutamine-alanine in at 37°C in a humidified atmosphere containing 5% CO_2. A-2058 cells were trypsinized and suspended in cell culture grade phosphate buffered saline (1×, PH 7.4) at a concentration of 5×10^7 cells/mL for tumor inoculation.

All experimental procedures were approved by the University of Kansas Institutional Animal Care and Use Committee (IACUC). Female athymic nude mice (~25 g, Charles River Laboratories; Wilmington, MA) were anesthetized with 2% isoflurane in oxygen, and 100 μL of A-2058 cell suspension was subcutaneously injected in the distal aspect of left mouse thigh and upper hind limb using a 27-ga needle to establish the tumor xenografts. Tumor growth was monitored twice per week via bi-dimensional measurement with a digital caliper, and the tumor volume was calculated using equation:

$$\text{Tumor volume } (mm^3) = 0.52\times(\text{width})^2\times(\text{length})$$

2.2.3 Treatment

Female Nu/Nu nude mice bearing melanoma tumors of roughly 50~100 mm^3 were randomly divided into five groups, including a non-treated group (N= 7) and four treatment groups (N=6-8). Three doses of 10 mg/kg CDDP or HA-Pt (on cisplatin basis) were administered weekly via tail vein for i.v. CDDP (N=6) group and i.v. HA-Pt (N=7) group; or subcutaneously near the tumor for s.c. CDDP (N=6) and s.c. HA-Pt (N=8) group. Following the treatment, the primary tumor size was measured twice weekly, and animals were euthanized once the tumor volumes reached 3000 mm^3 or in the presence of necrosis or ulceration unrelated to tumor growth, or if weight loss >20% occurred.

2.3 Statistical analyses

Tumor volumes and body weights for all five experimental groups were analyzed and expressed at mean ± standard deviation. Statistical analyses were conducted using unpaired t-test by GraphPad Prism 5 software with significance set at $p < 0.05$.

3. Results

3.1 Synthesis and characterization of HA-Pt conjugate

Cisplatin was efficiently conjugated to HA with a conjugation degree of 20% wt through formation of ester linkages with polycarboxyl groups of the HA polymer [2] The conjugate exhibited an in vitro release half-life of merely 10 hours [2]. A diameter of 7.55±1.72 nm of individual particles or 25.2 ± 4.43 nm of large clusters formed by HA-Pt conjugate was revealed using Transmission Electron Microscopy [2].

3.2 Therapeutic efficacy

The maximum tolerated dose (MTD) of cisplatin has been determined at 10 mg/kg body weight in mice [3]. The anti-tumor effect of HA-Pt and CDDP at MTD was evaluated by measuring tumor volume and survival times in nude mice bearing A2058 tumor xenografts. Skin tumors were observed in hind legs of nude mice within one week after tumor cell injection, and tumor volume typically reached ~100 mm^3 in two weeks. Following treatment, tumor burden was monitored up to nine weeks. For mice receiving no anticancer treatment, average tumor size was 1,600 mm^3 by week 5 (Figure 1A) and an average of 19-fold increase in tumor volume was observed from week-1 to week-4 (Figure 1B). In contrast, tumors in animals treated with s.c. HA-Pt ($p< 0.01$) or i.v. HA-Pt ($p< 0.05$) developed at a significantly slower rate during the same period, with week-4 tumor volumes 83% smaller than those in the non-treatment group (Figure 1A). Animals that received s.c. CDDP and i.v. CDDP showed delayed tumor initial progression, but by week 4 their tumors had respectively re-grown by 12-fold and 7-fold versus week-1 sizes. In

addition, 100% of the animals in two CDDP treated groups were euthanized within 5 weeks (Figure 2) either due to deteriorating body condition (Figure 3B) or necrosis of the injection site on the tail induced by the extravasation side effect of CDDP. By comparison, one mouse that was treated with s.c. HA-Pt showed complete tumor eradication and the mouse lived through this study (Figure 3D). Other s.c. HA-Pt mice were euthanized primarily due to weight loss, not tumor growth or ulceration.

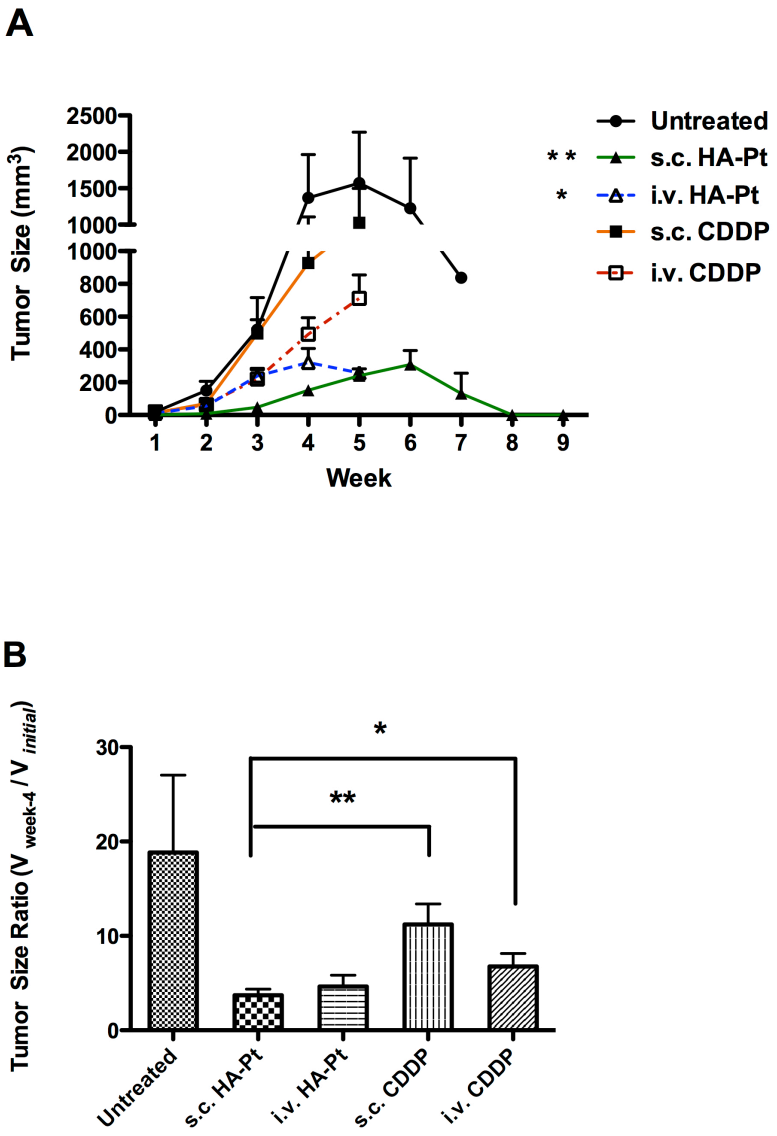

Figure 1. (A) Tumor growth after treatment with s.c. HA-Pt, i.v. HA-Pt, s.c. CDDP, i.v. CDDP, and untreated control. CDDP and HA-Pt on equivalent platinum basis (10 mg/kg) were injected either by i.v. tail vein or s.c around tumor, 6≤N≤8. (B) Tumor Volume ($V/V_{initial}$) at week-four after treatment, 5≤N≤8. (*: $p < 0.05$; **: $p < 0.01$)

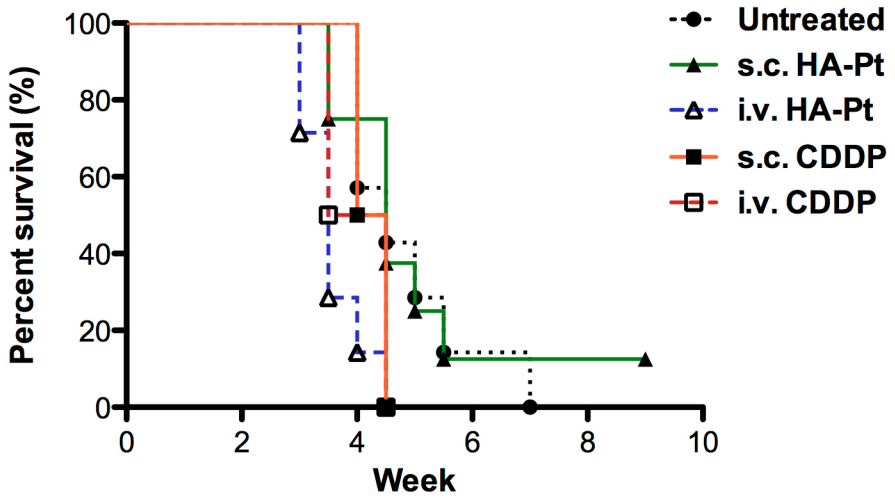

Figure 2. Survival curve after treatment with untreated control, CDDP, or HA-Pt, respectively. CDDP and HA-Pt on equivalent platinum basis (10 mg/kg) were injected either by i.v. tail vein or s.c around tumor, 6≤N≤8. Of note, untreated and conventionally treated animals were euthanized either due to tumor size or severe necrosis at the injection site, while the s.c. HA-Pt animals were euthanized due to weight loss and body condition score<2. * Body condition scoring (BCS) [4] is a useful tool for evaluating overall condition of the mouse.

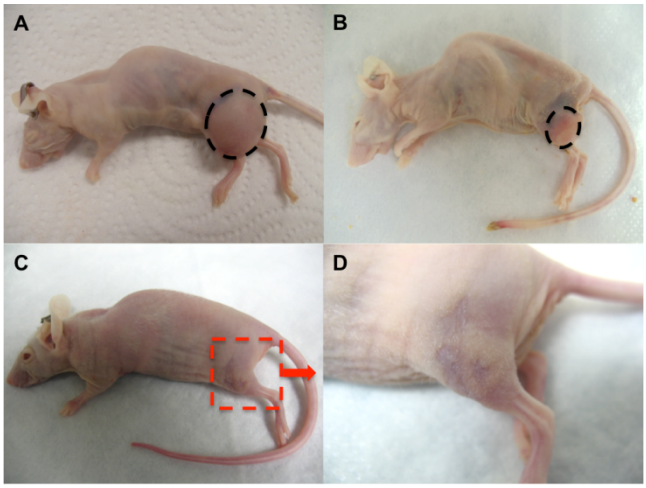

Figure 3. Nude mice bearing human A2058 melanoma tumor xenografts with untreated control (A, BCS*=2, tumor size = 2429 mm^3), i.v. CDDP (B, BCS =1, tumor size = 502 mm^3), s.c. HA-Pt (C &D, BCS = 3, tumor size = 0 mm^3). BCS of 1 or 2 indicates that the mouse is emaciated or under-conditioned, respectively. A mouse with BCS of 3, in comparison, is well conditioned.

4. Discussion

Locally advanced cancer refers to cancers that have spread from where they started to nearby tissues or lymph nodes [5]. Such cancers generally cannot adequately be treated by surgical resection alone. This report presents the results of a locally-delivered chemotherapy treatment in a murine model for locally advanced melanoma.

Although treatment of melanoma has demonstrated incremental improvement over the last few decades, in 2011 the 5-year death rate for stage 3 locally advanced melanoma with lymphatic metastases was still 37.6% [1]. Over 6000 people are diagnosed with stage 3 melanoma per year in the US [6]. There is at present no chemotherapy approved for direct delivery into locally advanced melanoma. Current standard-of-care treatment relies on surgery, and, in certain cases, local radiation and/or immunomodulators such as interferon-α or interleukin-2. Chemotherapy is generally reserved for disease that has progressed to distant metastases. Even so, traditional chemotherapeutic agents have not shown prolonged responses in most patients.

While newer agents have shown promise, none has yet demonstrated sustained efficacy for most treated patients. For instance the BRAF inhibitor vermurafenib has recently demonstrated a 4-month survival advantage in patients with unresectable melanoma [7]. The immune modulator ipilimumab, an anti-CTLA4 monoclonal antibody, has been shown to promote antitumor immunity and improve survival rates in patients with metastatic melanoma [8]. A metanalysis

showed a 6-month increase in overall survival time for ipilimumab compared to chemotherapy [9]. In patients with stage III and stage IV unresectable melanoma, combining ipilumimab with a gp100 peptide vaccine showed a four-month survival advantage versus vaccine alone (10.1 months vs. 6.4 months) [8]. Though not yet approved, numerous vaccines are currently being developed for the treatment of melanoma, including dendritic cell vaccines and herpes simplex virus oncolytic "vaccines".

Current immune treatments such as ipilumimab carry risks for significant side effects including hepatic and gastrointestinal toxicity, endocrine dysfunction and permanent retinal damage [10]. Ocular side effects include conjunctivitis, scleritis, uveitis [10], decreased visual actuity, photophobia, and painful tearing [11], as well as Graves opthalmopathy [10, 12].

Traditional chemotherapy is not typically used in locally advanced melanoma, but it can play a role in treating distant metastases. Cisplatin, also known as CDDP, is one such potential chemotherapy candidate. CDDP is a DNA-damaging chemotherapeutic agent that induces apoptosis in tumor cells. CDDP achieves higher concentrations in melanoma tissue than plasma. In a patient receiving IV CDDP for cutaneous melanoma metastases, platinum levels in tumor tissue were three times higher than plasma [13]. Although widely used across a broad variety of cancers, CDDP has played only a limited role in melanoma treatment. CDDP has not shown great efficacy as melanoma monotherapy, likely due to dosing limitations.

CDDP has been studied in combination with other melanoma treatments including immunotherapy [14-16], gene therapy [17-19], and other small-molecule anticancer agents [3, 20, 21]. These studies have used both murine and human melanoma lines in mouse xenotransplantation models, and have demonstrated synergistic inhibitory effects resulting in significant retardation or even complete tumor growth inhibition. The enhanced cytostatic/cytotoxic effects might be attributed to coupling tumor cell apoptosis induced by CDDP with anti-proliferatitive, antiangiogenic or anti-cell cycle effects of other agents. The precise mechanisms underlying the synergies have not yet been fully elucidated.

Of note, when augmented anti-tumor effects were found in combination immuno-chemo studies, they typically used intensive CDDP treatment schedules that would not likely be tolerated by human patients. [17] Delivering chemotherapy directly to tumor and local lymph nodes could result in much more of the chemotherapy actually getting to where it is needed. This might be even more advantageous in treating locally advanced disease.

Here we present a new method for achieving very high doses of CDDP in locally advanced melanomas. We previously reported synthesis of an injectable hyaluronan–CDDP nano-conjugate (HA-Pt) using the FDA-approved biocompatible carrier hyaluronan (HA) [22]. HA-Pt can be administered subcutaneously as a peri- or intra-tumoral injection. As such, it has the potential to enhance drug accumulation in the primary tumor and adjacent lymph nodes, while simultaneously reducing overall systemic exposure [2, 22]. Nodal penetration is important since

local nodes are where most tumor metastases start. HA-Pt has previously demonstrated improved anti-tumor efficacy in *in vivo* murine models of locally advanced head and neck squamous cell carcinoma [23] and breast cancer [24]. The present study provides the first experimental evidence that HA-Pt can inhibit human melanoma growth in mice.

HA-conjugation may be especially helpful because HA is a ligand for the tumor-associated surface receptor CD44. Numerous studies have shown that CD44 is expressed in both primary and metastatic melanoma [25, 26]. CD44 is the main hyaluronic acid surface receptor on melanoma cells, and CD44 expression increases during melanoma progression [27]. CD44 expression in melanoma cells has also been associated with worsening Clark's stage [25]. Although CD44-hyaluronic acid interaction has been reported to induce melanoma cell proliferation [27], when the hyaluronan in question is conjugated to a poison it is would not appear likely to promote tumor survival. Furthermore, a recent report found that not only was CD44 expressed in all tumor stromal cells studied, but CD44 expression by tumor stromal precursors played vital roles in tumor migration, incorporation, and functionality [12]. Therefore HA-Pt could potentially target tumor stroma as well as neoplastic cells.

The ability to shrink melanomas via direct injection of HA-Pt could be of clinical interest in several circumstances, including augmentation or even substitution for complete lymph node dissection (CLND) or radiation, preoperative

shrinkage of very large primary tumors, palliative shrinkage of large or awkwardly located metastases, and synergistic combination with immunotherapy.

Radiation therapy has been used as adjuvant therapy following CLND, and as alternate therapy for affected regional lymph nodes. When used as adjuvant therapy after lymphadenectomy, only 10% of patients who received radiation developed regional reoccurrence after five years, as opposed to 40% of patients who did not receive radiation [28]. Another study demonstrated doubling of disease-free survival time when radiation therapy was used to treat regional lymph nodes [29]. Radiation has also been used in the treatment of skin metastases; however, treatments of over 6 Gy were needed to elicit response rates above 90% [30]. Since cisplatin has been shown to sensitize cancer cells to ionizing radiation, targeting CDDP to nodes via HA-Pt could be useful [31]. This might be especially helpful in patients who are not candidates for full-dose systemic CDDP or high-dose radiation.

Furthermore, because complete lymph node dissection is associated with serious morbidities, including lymphedema, bleeding, infection, and deep vein thrombosis [32], some patients are unable or unwilling to undergo CLND despite positive sentinel lymph node or other risk factors for nodal involvement. Such patients may benefit from such a treatment that can deliver a large dose to the local nodes with relatively low systemic exposure and a correspondingly high therapeutic index.

Shrinking very large melanomas prior to surgery could improve cosmesis and also improve cure rates especially in certain areas the body such as the face,

hands or feet where wide margins are hard to achieve. Similarly, patients with large or obstructive metastases could potentially benefit from direct injection of HA-Pt for palliative tumor masses shrinkage. Doing so might provide benefit with fewer side effects than such conventional treatments as high-dose chemotherapy or repeated surgical debulking.

Mouse and human studies have explored combined use of platinum-based antineoplastic drugs (e.g. cisplatin or carboplatin) and immunotherapy (e.g. interleukin-2 or interferon-alpha 2a). One combination therapy demonstrated synergistic inhibition of advanced B16-F1 melanoma growth in syngeneic mice [15] and another combination therapy study showed at least additive benefit with mostly moderate toxicity in two consecutive phase II trials with a total of 85 patients[16]. In our murine melanoma study, local administration of HA-Pt showed improved efficacy versus standard i.v. CDDP. HA-Pt may therefore potentially be of benefit in sequential chemo/immunotherapy protocols.

5. Conclusions

Although further work is needed, these data provide preliminary support for the proposition that HA-Pt may potentially play a role in treating locally advanced melanoma and other similar conditions.

6. References

1. Institute, N.C. *SEER Stat Fact Sheets: Melanoma of the Skin*. 2013 [cited 2013 July 9th]; Available from: http://seer.cancer.gov/statfacts/html/melan.html.
2. Cai, S., et al., *Carrier-based intralymphatic cisplatin chemotherapy for the treatment of metastatic squamous cell carcinoma of the head & neck.* Ther Deliv, 2010. **1**(2): p. 237-45.
3. Feleszko, W., et al., *Potentiated antitumour effects of cisplatin and lovastatin against MmB16 melanoma in mice.* Eur J Cancer, 1998. **34**(3): p. 406-11.
4. Charmaine J. Foltz, M.U.-C., *Guidelines for Assessing the Health and Condition of Mice.* Lab Animal, 1999. **28**(4): p. 28-32.
5. Institute, N.C., *Locally advanced cancer*, in *NCI Dictionary of Cancer Terms*2013.
6. Society, A.C. *Cancer Facts & Figures 2013*. 2013 [cited 2013 June 10th]; Available from: http://www.cancer.org/research/cancerfactsstatistics/cancerfactsfigures2013/index.
7. da Rocha Dias, S., et al., *The European Medicines Agency review of vemurafenib (Zelboraf(R)) for the treatment of adult patients with BRAF V600 mutation-positive unresectable or metastatic melanoma: summary of the scientific assessment of the Committee for Medicinal Products for Human Use.* Eur J Cancer, 2013. **49**(7): p. 1654-61.
8. Hodi, F.S., et al., *Improved survival with ipilimumab in patients with metastatic melanoma.* N Engl J Med, 2010. **363**(8): p. 711-23.

9. Dequen, P., et al., *Systematic review and network meta-analysis of overall survival comparing 3 mg/kg ipilimumab with alternative therapies in the management of pretreated patients with unresectable stage III or IV melanoma.* Oncologist, 2012. **17**(11): p. 1376-85.

10. Tarhini, A., *Immune-Mediated Adverse Events Associated with Ipilimumab CTLA-4 Blockade Therapy: The Underlying Mechanisms and Clinical Management.* Scientifica, 2013. **2013**: p. 19.

11. Thumar, J.R. and H.M. Kluger, *Ipilimumab: a promising immunotherapy for melanoma.* Oncology, 2010. **24**(14): p. 1280-8.

12. Spaeth, E.L., et al., *Mesenchymal CD44 expression contributes to the acquisition of an activated fibroblast phenotype via TWIST activation in the tumor microenvironment.* Cancer Res, 2013. **73**(17): p. 5347-59.

13. Stewart, D.J., et al., *Human tissue distribution of platinum after cis-diamminedichloroplatinum.* Cancer Chemother Pharmacol, 1982. **10**(1): p. 51-4.

14. Seo, K.W., et al., *Anti-tumor effects of canine adipose tissue-derived mesenchymal stromal cell-based interferon-beta gene therapy and cisplatin in a mouse melanoma model.* Cytotherapy, 2011. **13**(8): p. 944-55.

15. Kubo, H., et al., *Sequential chemoimmunotherapy with cisplatin, interferon-beta and interleukin-2 inhibits the growth of B16-F1 melanoma in syngeneic mice.* Melanoma Res, 2000. **10**(3): p. 223-9.

16. Kirchner, H.H., J. Atzpodien, and H. Poliwoda, *[Chemo-/immunotherapy in advanced malignant melanoma: carboplatin and DTIC or cisplatin, dtic, bcnu*

and tamoxifen followed by immunotherapy with interleukin 2 and interferon alpha-2a]. Med Klin, 1996. **91 Suppl 3**: p. 44-9.

17. Zupi, G., et al., *Antitumor efficacy of bcl-2 and c-myc antisense oligonucleotides in combination with cisplatin in human melanoma xenografts: relevance of the administration sequence.* Clin Cancer Res, 2005. **11**(5): p. 1990-8.
18. Citro, G., et al., *c-myc antisense oligodeoxynucleotides enhance the efficacy of cisplatin in melanoma chemotherapy in vitro and in nude mice.* Cancer Res, 1998. **58**(2): p. 283-9.
19. Pandha, H.S., et al., *Synergistic effects of oncolytic reovirus and cisplatin chemotherapy in murine malignant melanoma.* Clin Cancer Res, 2009. **15**(19): p. 6158-66.
20. Thallinger, C., et al., *CCI-779 plus cisplatin is highly effective against human melanoma in a SCID mouse xenotranplantation model.* Pharmacology, 2007. **79**(4): p. 207-13.
21. Liu, X., S.Y. Chan, and P.C. Ho, *Comparison of the in vitro and in vivo effects of retinoids either alone or in combination with cisplatin and 5-fluorouracil on tumor development and metastasis of melanoma.* Cancer Chemother Pharmacol, 2008. **63**(1): p. 167-74.
22. Cai, S., et al., *Intralymphatic chemotherapy using a hyaluronan-cisplatin conjugate.* J Surg Res, 2008. **147**(2): p. 247-52.
23. Cohen, S.M., et al., *Efficacy and toxicity of peritumoral delivery of nanoconjugated cisplatin in an in vivo murine model of head and neck*

squamous cell carcinoma. JAMA Otolaryngol Head Neck Surg, 2013. **139**(4): p. 382-7.

24. Cohen, M.S., et al., *A novel intralymphatic nanocarrier delivery system for cisplatin therapy in breast cancer with improved tumor efficacy and lower systemic toxicity in vivo.* Am J Surg, 2009. **198**(6): p. 781-6.
25. Seiter, S., et al., *Expression of CD44 splice variants in human skin and epidermal tumours.* Virchows Arch, 1996. **428**(3): p. 141-9.
26. Schaider, H., et al., *CD44 and variants in melanocytic skin neoplasms.* J Cutan Pathol, 1998. **25**(4): p. 199-203.
27. Ahrens, T., et al., *CD44 is the principal mediator of hyaluronic-acid-induced melanoma cell proliferation.* J Invest Dermatol, 2001. **116**(1): p. 93-101.
28. Agrawal, S., et al., *The benefits of adjuvant radiation therapy after therapeutic lymphadenectomy for clinically advanced, high-risk, lymph node-metastatic melanoma.* Cancer, 2009. **115**(24): p. 5836-44.
29. Creagan, E.T., et al., *Adjuvant radiation therapy for regional nodal metastases from malignant melanoma: a randomized, prospective study.* Cancer, 1978. **42**(5): p. 2206-10.
30. Barker, C.A. and N.Y. Lee, *Radiation therapy for cutaneous melanoma.* Dermatol Clin, 2012. **30**(3): p. 525-33.
31. Boeckman, H.J., K.S. Trego, and J.J. Turchi, *Cisplatin sensitizes cancer cells to ionizing radiation via inhibition of nonhomologous end joining.* Mol Cancer Res, 2005. **3**(5): p. 277-85.

32. Ahmed, A., et al., *Postoperative Complications following Nodal Dissection and Their Association with Melanoma Recurrence.* ISRN Surg, 2013. **2013**: p. 382138.

Chapter 7

Future Work-Development of Folate-conjugated core/shell magnetic nanoparticles for targeted hyperthermia

1. Introduction

Previous work on core/shell magnetic nanoparticles (MNPs) focused on the enhancement of the aqueous dispersity and biocompatibility of the as-synthesized MNPs, as well as evaluation of therapeutic efficacy of MNPs-mediated hyperthermia treatment against breast tumors. MNPs can also be utilized in the active targeting of tumor cells, via attaching to a targeting moiety to enable preferential accumulation within the tumors. The folate receptor (FR) is an anchored cell surface receptor that is highly expressed on many human cancer cells such as breast, ovarian, cervical, brain and colorectal tumors [1, 2]. Folate, a non-immunogenic vitamin, is a key factor for DNA replication and binds to FR with high affinity [2-4]. Therefore, the Folic acid/FA interaction can be harnessed to facilitate the entrance of theranostic agents into cancer cells via receptor-mediated endocytosis [5, 6], thus enhancing the diagnosis accuracy and therapeutic efficacy. For future multifunctional magnetic nanoparticle (MNPs) delivery, it would be advantageous to develop folate receptor-targeting core/shell MNPs that are specifically internalized by tumor cells. In the present study, we have synthesized folic acid-modified core/shell MNPs, and they exhibited excellent aqueous dispersity and increased intracellular uptake by a FR-positive human breast tumor cell line. Future work will focus on *in vivo* evaluation of body distribution and tumoral uptake of the FA-MNPs, as well as the efficacy in augmenting magnetic resonance imaging (MRI) contrast and mediating hyperthermia against human breast tumors.

2. Preliminary *in vitro* experiments

2.1 Materials

All chemicals were used as received without further purification unless otherwise noted. Carboxylic PEG amine (NH_2–PEG–COOH)(≥99.5%) was purchased from Jenkem Technology (Beijing, China). Methoxyl PEG carboxylic acid (OMe-PEG) was obtained from Nanocs (New York, NY, USA). Folic acid (crystalline) was purchased from Alfa Aesar (Ward Hill, MA, USA). N-(3-Dimethylaminopropyl)-N′-ethylcarbodiimide (EDC), N-Hydroxysuccinimide (NHS)(98%), (3-Aminopropyl) triethoxysilane (silane-amine)(99%), acetone (≥99.5%), triethylamine (TEA)(≥99.5%) and toluene (anhydrous, 99.8%) were purchased from Sigma-Aldrich Co (St. Louis, MO, USA). Methanol (≥99.9%) and N,N-Dimethylformamide (99.8%, Extra Dry) were obtained from Fisher Scientific (Pittsburgh, PA, USA). Ethanol (200 proof) was purchased from Decon Labs, Inc (King of Prussia, PA, USA). Double distilled water (ddH_2O) was used in syntheses, characterization, cell culture, and animal experiments (sterilized by autoclaving). Dimethyl sulfoxide-D_6 (DMSO-D_6) was purchased from Cambridge Isotope (Andover, MA, USA). Cell culture medium, Dulbecco's Modified Eagle Medium (DMEM), and Fetal Bovine Serum (FBS) were purchased from Life Technologies (Grand Island, NY, USA).

2.2 Methods

2.2.1 Preparation of folic acid-PEG conjugate (FA-PEG-COOH)

The folic acid-PEG conjugate was synthesized as reported earlier with a minor modification [7]. In brief, folic acid (102 mg, 0.23 mmol) dissolved in 10 mL of anhydrous N,N-Dimethylformamide (DMF) was activated with EDC (5 eq; 178 mg) and NHS (5 eq; 132 mg) at ambient temperature overnight under an argon atmosphere. The mixture was then reacted with NH_2–PEG–COOH (0.1 equi; 50 mg) dissolved in 5 mL of DMF in the presence of TEA (3 equi; 16 µL). The mixture was stirred at ambient temperature for 4 h, and then was added into 40-mL ice-cold acetone. Unreacted folic acids were removed by centrifugation, and the resultant supernatant was dialyzed against ddH_2O for 24 h (Spectra/Por 6, MWCO: 1000), followed by lyophilization to render the dry powder of FA-PEG-COOH.

2.2.2 Preparation of aminosilane -modified core/shell FePt@Fe_3O_4 MNPs (silane-MNPs)

Core/shell FePt@Fe_3O_4 MNPs were modified with silane-amine through a ligand exchange reaction using a modified method published by Zhang *et. al*.[8]. Briefly, 200 µL of as-synthesized nanoparticles in hexane (30 mg/mL) were washed with 10 mL of ethanol and centrifuged at 10,000×g for 15 min. After the supernatant was discarded, precipitated MNPs were re-suspended in 300 µL of hexane. The washing step was repeated three times and the precipitated nanoparticles were then dried with speedvap overnight to remove residual solvents. The dried nanoparticles were dispersed in 1.5 mL of anhydrous toluene, followed by adding 300 µL of silane-amine and 1 mL of TEA. The mixture was stirred at 50° C

overnight, followed by centrifugation (10,000×g for 15 min) to collect the silane-grafted MNPs (silane-MNPs). The silane-MNP precipitates were washed with ethanol three times and then dried with speedvap at 35° C.

2.2.3 Modification of silane-MNPs with PEG-FA or PEG-MNPs

12 mg of FA-PEG-COOH was dissolved in 4-mL sodium borate buffer (0.01M, pH 8.0) and then activated with 4 equivalent of EDC (3 mg)/NHS (2.5 mg) for 2 h at ambient temperature. The activated mixture was added with 3-mg silane-MNP dispersed in DMSO and then stirred overnight. FA-PEG modified MNPs were collected following the procedures described in the section 2.2.2. To prepare a non-targeted PEGylated MNPs as control, methoxyl PEG carboxylic acid was used instead of FA-PEG-COOH.

2.2.4 ^{1}H Nuclear magnetic resonance (NMR) spectroscopy

The FA, NH_2–PEG–COOH and FA-PEG-COOH were dissolved in DMSO-D_6 and their 1H NMR spectra were collected on a Bruker Avance 400 MHz NMR Spectrometer (Bruker Corporation, MA, USA).

2.2.5 Fourier Transform Infrared Spectroscopy (FTIR)

FTIR spectra of approximately 2 mg of dried polymers or MNPs were recorded using an IRAffinity-1 FTIR (Shimadzu Scientific Instruments, KS, USA). For each spectrum, 45 scans were collected between 400 and 4000 cm^{-1} at a resolution of 1 cm^{-1}.

2.2.6 Hydrodynamic diameter measurements

FA-MNPs or PEG-MNPs were dispersed at 0.5 mg/mL in PBS, and dynamic light scattering (DLS) measurements of the hydrodynamic diameters of MNP dispersions were performed at 25 °C using a ZetaPlus Particle Size Analyzer (Brookshaven Instrument, NY, USA). All measurements were repeated five times.

2.2.7 *In vitro* cytotoxicity

A metastatic murine breast cancer cell line, MDA-MB-231, purchased from ATCC® was cultured in DMEM supplemented with 10% (v/v) FBS and 1% L-glutamine. Cells were trypsinized and seeded into 96-well plates at 3,000 cells/well (n=3 plates, 12 wells/concentration) and incubated overnight. FA-MNPs or PEG-MNPs dispersed in PBS were added to each well with final concentrations of 5 μg/mL to 1 mg/mL. A resazurin-based colorimetric assay was used to measure viability of cell cultures.

2.2.8 Cellular uptake

To investigate the intracellular uptake of MNPs, MDA-MB-231 cells were seeded in 12-well plates at 3×10^5 cells/well and then incubated with FA-MNP or PEG-MNP suspensions in PBS at 0.3 mg/mL for 24 h. The same volume of the PBS without MNPs was added to cell cultures as a control. After three washes with PBS, the cells were detached with trypsin and then re-suspended in DMEM for cell counting using a hemocytometer. To measure the intracellular uptake of MNPs, the cell suspensions were centrifuged at 8,000×g for 10 min, and cell pellets were digested in 30% HCl at 70 °C for 1h. MNPs in cells were quantified on an inductively coupled plasma mass spectrometer (ICP-MS) (7500a, Agilent Technologies, CA, USA) for iron content, and samples collected from untreated cells were used as a negative control. All measurements were repeated three times.

2.3 Statistical analyses

Tumor size ratio for the four experimental groups were analyzed and expressed at mean ± standard deviation. Statistical significance was determined by the two-way ANOVA with $P< 0.05$ using the GraphPad Prism 6 software.

3. Preliminary results

3.1 Synthesis and characterization of core/shell FePt@Fe_3O_4 MNPs

3.1.1 Synthesis of FA-PEG

Folic acid was covalently linked to the amino group of the heterobifunctional PEG, NH_2-PEG-COOH, via an EDC/sulfo-NHS coupling chemistry. The successful conjugation was confirmed by the presence of characteristic peaks of FA and NH_2-PEG-COOH in the ^{1}H-NMR spectrum of the purified FA-PEG (Figure 1C). Moreover, upon amidation, the chemical shift of the α hydrogen proton adjacent to the amino group of NH_2-PEG-COOH moved from 2.97 ppm (Figure 1B) to a higher frequency. The peak of the corresponding methyl group in the FA-PEG-COOH was not observed in the ^{1}H-NMR spectrum (Figure 1C), probably as it overlapped with the water residue peak.

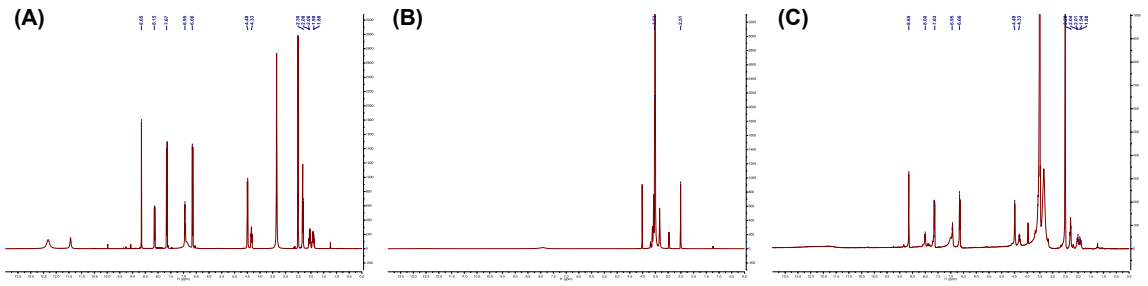

Figure 1. ^{1}H-NMR spectra (DMSO-D_6, 400 MHz) of (A) Folic acid, (B) Amine-PEG-COOH, (C) FA-PEG-COOH. The peak at δ = 2.54 or 3.33 in each spectrum corresponds to the solvent residue of DMSO or water, respectively.

3.1.2 Surface modification of core/shell MNPs with folic acid and PEG

The surface of as-synthesized core/shell MNPs was first grafted with amino groups via a facile silanization reaction, which in turn enabled immobilizing FA-PEG or OMe-PEG through the EDC/NHS-catalyzed reaction between the amino groups on MNPs and the carboxyl terimus of PEG molecules. FTIR spectra of FA, FA-PEG, PEG-MNPs and FA-MNPs are shown in Figure 2. The high-intensity bands at 1605 and 1692 cm^{-1} in Figure 2A were two characteristic peaks of FA, and they were also found in the spectra of FA-PEG (Figure 2B) and FA-MNPs (Figure 2D), indicating a successful FA modification. The FTIR peaks between 840 and 1040 cm^{-1} of the purified MNPs dry power (Figure 2C and D) were assigned to the Si-O-Fe stretching. In addition, the ether group C-O-C stretching band and the vibration band were resolved at 1100 cm^{-1} and 1360 cm^{-1}, respectively, and these two peaks were observed in all three PEG-containing moieties (Figure 2B to D). These results are in great agreement with observations in another study performed by Zhang *et al* [8].

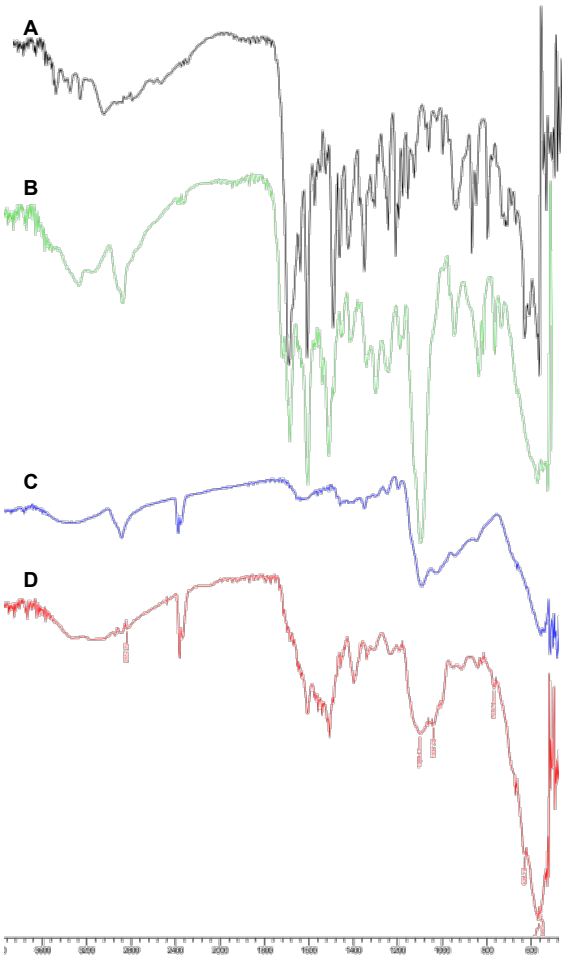

Figure 2. FTIR of (A) Folic acid (FA), (B) FA-PEG-COOH, (C) PEG-MNPs and (D) FA-PEG-MNPs.

3.2 Hydrodynamic size measurements

Both surface-modified MNPs were well dispersed in aqueous solutions due to the PEG-coating on the surface. The hydrodynamic diameters of FA-MNPs and PEG-MNPs are 63.9 ± 3.8 nm and 113.8 ± 10.8 nm, respectively (Figure 3), making them ideal candidates for accumulation into the defective vascular architecture of the breast tumor region via the enhanced permeability and retention effect. The significantly smaller size of the FA-MNPs was probably caused by deprotonation of the carboxylic acid groups of the surface-attached folic acid, thus increasing the aqueous-dispersity of FA-MNPs.

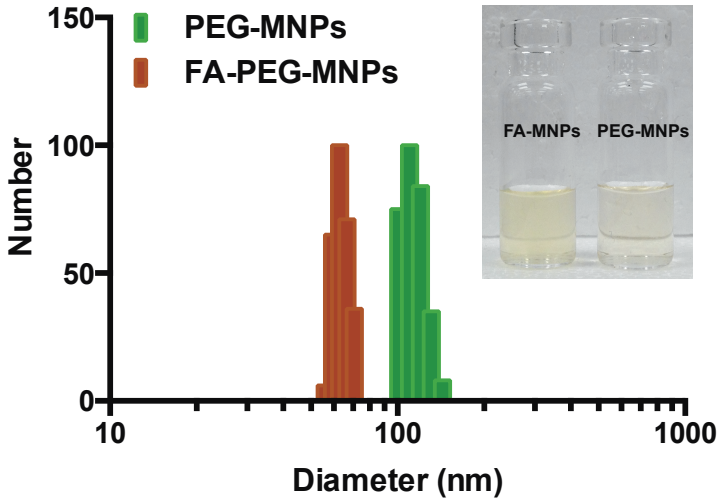

Figure 3. DLS of PEG-MNPs (green) and FA-MNPs (brown) in PBS at 25° C (size distribution in number). Insert: Representative images of FA-MNP (left) and PEG-MNP (right) dispersion (0.5 mg/mL) in PBS.

3.3 *In vitro* cytotoxicity and intracellular uptake and of PEG-MNPs and FA-MNPs

A resazurin cell viability assay was performed in a human breast tumor cell line, MDA-MB-231, to assess the toxicity of the PEG-MNPs and FA-MNPs. Compared with FA-MNPs, the PEG-MNPs exhibited significantly lower cytotoxicity at concentrations ranging from 0.01 to 0.5 mg/mL, as shown in Figure 4. Cells treated with PEG-MNPs were approximately 72 % viable at a high concentration of 0.5 mg/mL after incubation for 72 h, suggesting its non-toxic nature. In comparison, FA-MNPs substantially inhibited cell growth. A cell viability of only 69% was observed even when cells were incubated with 0.01 mg/mL of FA-MNPs for the same duration.

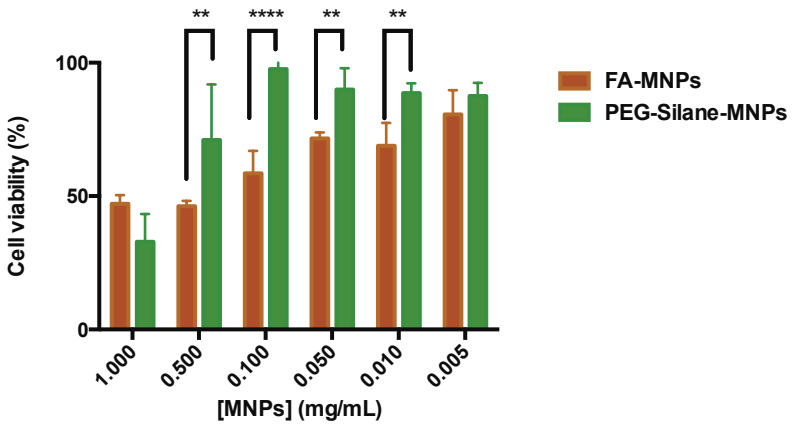

Figure 4. Effects of the PEG-MNPs and FA-MNPs on the proliferation of FR-positive human breast cancer MDA-MB-231 cells. After 72-h incubation, the relative number of viable cells was determined by a resazurin assay.

The capability of the FA-MNPs to target FR-positive tumors was also evaluated in MDA-MB-231 cell line. The ICP-MS iron analysis of digested cell pellets after a 24-h FA-MNPs treatment showed significantly enhanced intracellular accumulation with 122.1 ± 20.9 pg/cell (Figure 5), approximately 2 folds higher than that of the cells treated with PEG-MNPs at an equivalent concentration.

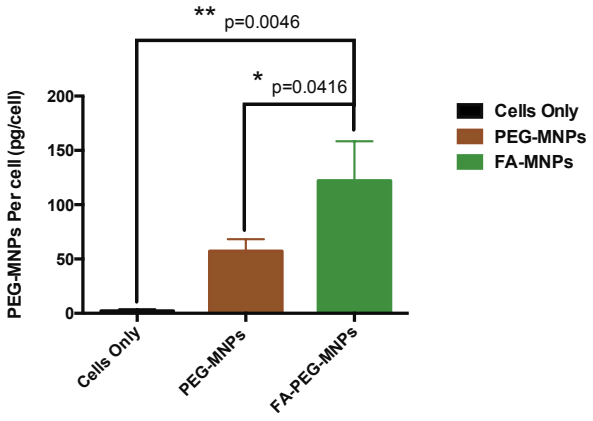

Figure 5. Intracellular uptake of the PEG-MNPs and FA-MNPs by MDA-MB-231 cells after a 24-h incubation at the concentration of 0.3 mg/mL. (Iron analysis by ICP-MS: detection limits=3.79 ppb; R^2=0.9982)

4. Future work

Our *in vitro* results indicate that folic acid-modified core/shell magnetic nanoparticles appear to be a promising targeting delivery system to enhance the MNP accumulation in breast tumors that overexpress the folic acid receptor. This FA-MNPs can be exploited as a potent theranostic agent to enhance the MRI contrast and increase the antitumor efficacy of the MNP-mediated hyperthermia. Therefore, future work will focus on *in vivo* evaluation of its theranostic efficiency in breast cancer xenograft models in mice.

5. References

1. Parker, N., et al., *Folate receptor expression in carcinomas and normal tissues determined by a quantitative radioligand binding assay.* Anal Biochem, 2005. **338**(2): p. 284-93.
2. Garin-Chesa, P., et al., *Trophoblast and ovarian cancer antigen LK26. Sensitivity and specificity in immunopathology and molecular identification as a folate-binding protein.* Am J Pathol, 1993. **142**(2): p. 557-67.
3. Oaks, B.M., et al., *Folate intake, post-folic acid grain fortification, and pancreatic cancer risk in the Prostate, Lung, Colorectal, and Ovarian Cancer Screening Trial.* Am J Clin Nutr, 2010. **91**(2): p. 449-55.
4. Mansoori, G.A., K.S. Brandenburg, and A. Shakeri-Zadeh, *A comparative study of two folate-conjugated gold nanoparticles for cancer nanotechnology applications.* Cancers, 2010. **2**(4): p. 1911-28.

5. Weitman, S.D., et al., *Distribution of the folate receptor GP38 in normal and malignant cell lines and tissues.* Cancer Res, 1992. **52**(12): p. 3396-401.

6. Ross, J.F., P.K. Chaudhuri, and M. Ratnam, *Differential regulation of folate receptor isoforms in normal and malignant tissues in vivo and in established cell lines. Physiologic and clinical implications.* Cancer, 1994. **73**(9): p. 2432-43.

7. Yoo, H.S. and T.G. Park, *Folate-receptor-targeted delivery of doxorubicin nano-aggregates stabilized by doxorubicin-PEG-folate conjugate.* J Control Release, 2004. **100**(2): p. 247-56.

8. Zhang, Y., N. Kohler, and M. Zhang, *Surface modification of superparamagnetic magnetite nanoparticles and their intracellular uptake.* Biomaterials, 2002. **23**(7): p. 1553-1561.